Development of the Mass-47 Clumped Isotope Paleothermometer: Methods, Theory, and Application to Climate and Diagenetic Reconstructions

by

William Frederick Defliese

A dissertation submitted in partial fulfillment
of the requirements for the degree of
Doctor of Philosophy
(Geology)
in the University of Michigan
2014

Doctoral Committee:

Professor Kyger C. Lohmann, Chair
Professor Joel D. Blum
Assistant Professor David C. Lund, University of Connecticut
Associate Professor Nathan A. Niemi
Professor Donald R. Zak

Acknowledgements

I'd like to start by thanking my parents, Phil and Lenore, who have always supported me even if they don't understand what I'm doing half the time. I'd like to thank my advisor, Kacey Lohmann, for providing me with the tools and funding to succeed, and also for giving me a great deal of confidence both in the laboratory and the field that I can complete a project. I'd like to thank Lora Wingate in the stable isotope lab for technical support and also lending an ear when needed. Thanks also go out to the staff in the main office, particularly Anne Hudon, who has always taken great care of the graduate students. I'd like to thank Karthik Anantharaman, Ryan Lesniewski, and Ian Winkelstern for being wonderful officemates, and for many beers shared together. I'm grateful to others who have helped me out along the way: Mike Hren for teaching me everything about clumped isotopes in the lab; Alex Lechler and Nathan Niemi for lending me samples used in Chapter 3; Philip Maxwell, Andrea Dutton, and Jill VanTongeren for providing the samples and some of the data presented in Chapter 5. Lastly, I'd like to thank my committee, Kacey Lohmann, Joel Blum, David Lund, Nathan Niemi, and Don Zak, who have suffered through many committee meetings and other intrusions on their time.

Funding for this thesis came from many sources: The National Science Foundation, The Geological Society of America, The Scott Turner Fund, Rackham School of Graduate Studies, and The University of Michigan. Thanks to all for supporting my studies!

-Will

Table of Contents

List of Figures

Figure

List of Tables

Table

List of Equations

Equation

List of Appendices

Abstract

The mass-47 CO_2 clumped isotope paleothermometer is one of the most exciting developments in the field of paleothermometry of the last 50 years. This technique improves upon previous approaches in that it constrains the formation temperature of carbonate minerals in a single measurement without assumptions about the composition of the precipitating fluid. This allows the clumped isotope thermometer to be applied to situations where traditional techniques cannot discern the relative influences of temperature versus fluid composition, and allows more accurate reconstructions of Earth climate.

Several challenges remain before the thermometer can be accurately applied to Earth materials. Two separate calibrations must be employed to convert measured clumped isotope abundance into temperature estimates: a calibration of the effects of phosphoric acid digestion on CO_2 isotopologues; and a calibration of the corrected mass-47 CO_2 abundance to formation temperatures. Investigation of these calibrations reveals that they are likely mineralogy independent, suggesting that the cation and crystallographic structure plays a negligible role in clumped isotope equilibria.

A second challenge relates to the sample size required for clumped isotope studies: at ~ 20 mg per sample, sample homogeneity cannot be assumed. Full investigation of mixing effects using a computer model and laboratory tests shows that sample heterogeneity can have a measureable effect on clumped isotope temperature estimates, but that these effects can be mitigated by the use of subsampling and mathematical mixing calculations.

Further application of the clumped isotope thermometer requires detailed understanding of different proxy materials and the effects of geologic processes on these materials. Calcite formed by meteoric diagenesis was investigated in Pleistocene rocks and sediments. It was determined that meteoric phreatic cements accurately record mean annual temperature, while carbonate from vadose environments record kinetic departures from isotopic equilibrium.

To demonstrate the utility of clumped isotopes a suite of Cenozoic New Zealand bivalves were examined. The clumped isotope thermometer reveals that New Zealand climate warmed from the Eocene to Miocene, which is the opposite trend inferred using traditional approaches. The ability to constrain temperatures independent of water isotopic composition is a major breakthrough, and will continue to refine our understanding of Earth history.

Chapter 1

Introduction

Paleothermometry is the study of the Earth's temperature through time, which is a critical component of understanding many important questions within fields as diverse as climate change, evolution of life, and economic geology. For reconstructing temperature conditions on or near the Earth's surface, carbonate minerals are most commonly used as they precipitate from liquid water in a variety of environments and exist in large abundances throughout the geologic record. Many different materials and methods have been used to reconstruct temperature histories using carbonates, some of the most notable materials include various biogenic shells and inorganic cements, whereas common methods include oxygen isotope thermometry (Sharp 2007) and elemental ratio geochemistry (Klein et al. 1996). These techniques are all subject to different assumptions underlying their usage, and as such no single technique can be uniformly applied across geologic history.

Oxygen isotope thermometry is probably the most applied paleothermometer, with over 60 years of history and application building its resume. Oxygen isotope thermometry arose in the early 1950's as an extension of work on the Manhattan Project. Harold Urey and associates at the University of Chicago began examining the stable isotope composition of various earth materials after the conclusion of his wartime work separating isotopes for the atomic bomb. It was quickly realized that oxygen isotopes contained in carbonate materials underwent a temperature controlled fractionation during precipitation from water, and that by measuring the

$\delta^{18}O$ of both the water and the carbonate, it was possible to reconstruct the temperature of precipitation (McCrea 1950, Epstein et al. 1951). This fundamental discovery underlies the principle of $\delta^{18}O$ thermometry, but there are several complications that prevent $\delta^{18}O$ from resolving several scenarios and questions in Earth history, particularly in deep geologic time. Critically, to estimate the temperature, it is necessary to know both the $\delta^{18}O$ of the carbonate material (which is easily measured in the laboratory) and the $\delta^{18}O$ of the water from which it formed, a measure that is not available in all but a few scenarios (Sharp 2007). In many cases, a reasonable assumption about the $\delta^{18}O$ of the water can be made, and temperatures calculated based on that assumption. However, there exist many situations where it is difficult to constrain the $\delta^{18}O$ of water, and as such it is very difficult to apply oxygen isotope thermometry. A famous example is the apparent trend towards negative $\delta^{18}O$ values of low latitude brachiopods through time (Prokoph et al. 2008). This trend has been the source of much debate among the scientific community, because if interpreted with modern seawater $\delta^{18}O$ values it indicates that low latitude seawater temperatures in the Paleozoic reach as high as 60 °C. Such estimated temperatures are problematic for both our perception of the evolution of life and geodynamic models, as elevated temperatures of this magnitude would likely lead to runaway greenhouse conditions. If the trend is interpreted with constraining temperatures within modern conditions, then it implies that seawater $\delta^{18}O$ changed considerably in the last 500 million years, a chemical mass balance problem that remains controversial (Muehlenbachs 1998). Elemental proxies are subject to similar limitations and cannot be used reliably where the elemental ratios in precipitating water are unknown (Lear et al. 2000). To solve these ambiguities, a thermometry technique is required that allows direct measurement of formation temperatures without assumptions about the composition of the precipitating medium.

Mass-47 clumped isotope paleothermometry is an emerging isotopic technique developed in the early 2000's that is independent of the isotopic conditions of water, allowing it to be used in situations where traditional $\delta^{18}O$ thermometry cannot provide a resolution (Ghosh et al 2006, Eiler 2011). Like all new and emerging techniques, many questions exist about the mechanics of its application and the conditions necessary for accurate temperature reconstructions. The clumped isotope thermometer measures ^{13}C-^{18}O bonds in CO_2 produced from CO_3 of carbonate minerals, which is liberated by reaction with 105 weight percent phosphoric acid (Ghosh et al. 2006). The abundance of ^{13}C-^{18}O-^{16}O CO_2 molecules (mass 47 CO_2) present in a sample is compared to the number expected from a stochastic (randomized) distribution of isotopes in the sample based on the absolute abundance of ^{13}C and ^{18}O in the sample material. This difference is referred to as Δ_{47} and is controlled by the temperature of formation of the carbonate material. Importantly, this temperature can be calculated for any carbonate mineral independent of the bulk isotopic composition of the precipitating water (Tang et al. 2014). This technique holds great promise for resolving some of the questions currently unsolvable by conventional isotopic and elemental techniques, but challenges remain. The challenge of standardizing measurements in a 2 dimensional reference space was only realized in 2011 (Dennis et al. 2011), and many other issues remain with application. Much remains unknown about the behavior of the mass-47 clumped isotope paleothermometer with respect to fundamental laboratory procedures, interpretation of results, impacts of diagenesis, and integration with other paleo-proxies. This thesis attempts to investigate some of the fundamental behaviors and characteristics of Δ_{47}, which will allow it to be applied to a larger range of problems across a longer span of geologic time.

Chapter 2 is a multipart study that first investigates the behavior of Δ_{47} as CO_3 is reacted with phosphoric acid to produce CO_2. Currently, there is no known way to directly measure CO_3^{2-} ions in the unreacted carbonate for the absolute abundance of ^{13}C-^{18}O bonds, so digestion in H_3PO_4 is necessary to produce CO_2 gas while minimizing the exchange with byproduct H_2O. These digestions take 24 hours or longer depending on the mineralogy of the sample at 25 °C, which is the standard temperature for all chemical reaction equilibria and standardized calibration relations. Raising the temperature reduces the digestion time to 15-60 minutes, but at the cost of introducing a fractionation offset in Δ_{47} that must be accounted for in order to correct measured results to a standardized reference frame. This study calibrates the offset for a variety of carbonate minerals at different reaction temperatures, and allows for reactions performed at higher temperatures to be corrected back to 25 °C, enabling data comparison among laboratories and a uniform framework for accurate temperature reconstructions.

The second part of chapter 2 investigates the absolute relationship between Δ_{47} and precipitation temperature, providing a revised paleothermometer calibration. Calcite and aragonite minerals were precipitated in the laboratory at controlled temperatures, and subsequently analyzed for Δ_{47}. Δ_{47} values were then regressed against known precipitational temperatures to produce a temperature calibration for each mineral. In addition to allowing for accurate calculation of formation temperature, it is also the first study to empirically determine the effect of mineralogy on Δ_{47} in a controlled laboratory setting. These results were combined with prior data from the literature to produce a composite Δ_{47}-temperature calibration. Importantly, these results demonstrate that previously proposed temperature calibrations differ significantly for sample analysis at 25 °C from those preformed at higher temperatures.

Chapter 3 employs a numerical model to investigate the effects of end member mixing on absolute Δ_{47} values and thus, on the estimated temperature of precipitation. Discrepancies in temperature estimates can result in part because of the large sample size requirements for clumped isotope measurements (15-20 mg), which often exceeds the scale of isotopic homogeneity for many proxy materials and results in the physical mixing of materials of differing bulk composition. Mixing in Δ_{47} does not follow linear trends as might be expected in comparison to single isotope systems, and offsets from the mean values can occur. Investigations show that both positive and negative departures from the mean arise, and are solely controlled by the bulk isotopic composition of the end members. The numerical model is used to establish guidelines on when mixing can significantly bias results in clumped isotope studies, and recommends procedures to either avoid mixing problems or calculate the mixing derived offset that may occur.

Chapter 4 investigates the potential for meteoric diagenetic cements to be proxies for clumped isotope thermometry. Meteoric diagenetic cements, in particular meteoric phreatic cement, have the potential to be an excellent proxy material, as they form in isotopic equilibrium at Earth surface mean annual temperature and are immune to further mineral-driven diagenetic alteration. They are also not subjected to biologic factors (vital effects) that may cause departures from equilibrium in biogenic carbonates. Pleistocene and Holocene rocks of varying stages of alteration were collected from Bermuda and Barbados and analyzed for Δ_{47}, $\delta^{18}O$, and $\delta^{13}C$, and classified based on the type and amount of alteration present. This study shows that phreatic digenetic cements have the potential to be an excellent proxy material, whereas alteration in the vadose environment imparts large kinetic effects that significantly bias the Δ_{47}

signal, and may explain some of the documented high temperature estimates from proxy materials such as speleothems and soil carbonates.

Chapter 5 presents a novel combination of traditional $\delta^{18}O$ thermometry and clumped isotope analysis that is used to reconstruct the climate of New Zealand at 41, 27, and 16 Ma. Bivalves of the *Cucullaea* genus were sampled along growth bands to reconstruct seasonal $\delta^{18}O$ and $\delta^{13}C$ trends, while bulk Δ_{47} measurements are used to constrain average growth temperatures. These measurements are combined to reconstruct seasonal temperature changes and changes in seawater $\delta^{18}O$ through time due to ice volume and freshwater runoff. The resulting detailed climatic reconstruction contradicts the history what would be formulated from traditional techniques alone. This study showcases the ability of clumped isotope measurements, in combination with other paleotemperature proxies, to reconstruct paleoclimate where other proxies are lacking, and provides a blueprint for future studies to combine multiple proxies into detailed climatic histories.

Chapter 6 provides a summary of the work presented within, and outlook for future studies involving the clumped isotope paleothermometer.

References

Eiler, J. M. (2011), Paleoclimate reconstruction using carbonate clumped isotope thermometry, *Quaternary Science Reviews*, *30*(25–26), 3575-3588.

Epstein, S., R. Buchsbaum, H. Lowenstam, and H. C. Urey (1951), Carbonate-Water Isotopic Temperature Scale, *Geological Society of America Bulletin*, *62*(4), 417-426.

Ghosh, P., J. Adkins, H. Affek, B. Balta, W. Guo, E. A. Schauble, D. Schrag, and J. M. Eiler (2006), 13C–18O bonds in carbonate minerals: A new kind of paleothermometer, *Geochimica et Cosmochimica Acta*, *70*(6), 1439-1456.

Klein, R. T., K. C. Lohmann, and C. W. Thayer (1996), Bivalve skeletons record sea-surface temperature and δ18O via Mg/Ca and 18O/16O ratios, *Geology*, *24*(5), 415-418.

Lear, C. H., H. Elderfield, and P. Wilson (2000), Cenozoic deep-sea temperatures and global ice volumes from Mg/Ca in benthic foraminiferal calcite, *Science*, *287*(5451), 269-272.

McCrea, J. M. (1950), On the Isotopic Chemistry of Carbonates and a Paleotemperature Scale, *The Journal of Chemical Physics*, *18*(6), 849-857.

Muehlenbachs, K. (1998), The oxygen isotopic composition of the oceans, sediments and the seafloor, *Chemical Geology*, *145*(3), 263-273.

Prokoph, A., G. Shields, and J. Veizer (2008), Compilation and time-series analysis of a marine carbonate δ18O, δ13C, 87Sr/86Sr and δ34S database through Earth history, *Earth-Science Reviews*, *87*(3-4), 113-133.

Sharp, Z. (2007), *Principles of stable isotope geochemistry*, Pearson education Upper Saddle River, NJ.

Tang, J., M. Dietzel, A. Fernandez, A. K. Tripati, and B. E. Rosenheim (2014), Evaluation of kinetic effects on clumped isotope fractionation (Δ47) during inorganic calcite precipitation, *Geochimica et Cosmochimica Acta*, *134*, 120-136.

Chapter 2

Compositional and temperature effects of phosphoric acid fractionation on Δ_{47} analysis and implications for discrepant calibrations

2.1 Abstract

An essential procedure to increase the analytical efficiency of Δ_{47} measurements requires raising the temperature of phosphoric acid digestion for carbonate materials. This temperature change introduces a fractionation offset in Δ_{47} that must be accounted for prior to calculation of temperatures of carbonate formation and to allow interlaboratory comparison of results. We measured the phosphoric acid fractionation factor relative to reaction at 25 °C for calcite, aragonite, and dolomite across a temperature range from 25-90 °C. Significantly, all three minerals behave similarly during phosphoric acid digestion, allowing for a single temperature dependent acid fractionation relationship:

$$1000 \ln \propto_{CO_2(Acid)-\Delta_{47}} = \frac{(0.022434 \pm 0.001490)*10\text{^}6}{T^2} - (0.2524 \pm 0.0168) \qquad (2.1)$$

where α is the phosphoric acid fractionation factor, and T is in degrees Kelvin. Mineralogical or isotopic compositional effects on the fractionation factor were not observed, suggesting that this acid fractionation factor may be valid for all carbonate minerals.

We also present inorganic temperature calibrations for both calcite and aragonite at low temperatures (5-70 °C) and find them to agree with prior published data. Using the new acid fractionation factor, published Δ_{47}-temperature calibrations are recalculated. This analysis confirms a statistically significant Δ_{47}-temperature calibration difference between data analyzed at 25 °C versus higher temperatures. The origin of the discrepancy remains unknown, but it appears that the acid fractionation factor is not the cause.

2.2 Introduction

Mass-47 clumped isotope thermometry of carbonate and carbonate bearing minerals has been increasingly applied since its introduction in 2004 (Eiler and Schauble, 2004, Wang et al. 2004). This technique is desirable over traditional isotopic and elemental thermometry techniques because it eliminates many of the assumptions that must be made for accurate temperature estimates (ie seawater $\delta^{18}O$ values for $\delta^{18}O$ thermometry, seawater Mg/Ca ratios for Mg/Ca thermometry) (Eiler, 2007, 2011). Mass-47 clumped isotope measurements determine the abundance of ^{13}C-^{18}O bonds in CO_2 produced from phosphoric acid digestion of carbonate material (mass-47 CO_2) (Eiler and Shauble, 2004), and compare the absolute abundance of mass-47 CO_2 molecules produced to the number expected from a randomized, stochastic distribution of isotopes in the sample, as expressed by the formula

$$\Delta_{47} = \left[\left(\frac{R^{47}}{R^{47*}} - 1\right) - \left(\frac{R^{46}}{R^{46*}} - 1\right) - \left(\frac{R^{45}}{R^{45*}} - 1\right)\right] \times 1000‰ \qquad (2.2)$$

Δ_{47} in turn is temperature dependant such that when compared to empirical temperature calibrations (Ghosh et al. 2006, Tripati et al. 2010, Dennis et al. 2010, Eagle et al. 2013, Henkes et al. 2013) the equilibrium formation temperature of the source material can be calculated. The benefit of this technique is that it is fully independent of the isotopic composition of the

precipitating liquid, which allows an independent temperature measurement unlike traditional $\delta^{18}O$ techniques. For a review of Δ_{47} and its applications, see Eiler (2007, 2011).

Laboratory methods associated with this technique have eveolved since its introduction, with various innovations to increase sample reproducibility and sample throughput. One of the key limiting factors affecting sample throughput is the reaction rate of liberation of CO_2 from sample CO_3 during phosphoric acid digestion. Since measurement of Δ_{47} requires preservation of ^{13}C-^{18}O bonds through the liberation process, conservative approaches are necessary utilizing 105 wt. % phosphoric acid (Ghosh et al. 2006). 105 wt. % phosphoric acid has many useful properties, such as that it adsorbs water produced by the reaction of CO_3 at room temperature, which is important because H_2O can exchange with CO_2 produced by the reaction and scramble ^{13}C-^{18}O bonds in the measured sample (Wacker et al. 2013). For this reason, initial studies using Δ_{47} analysis reacted carbonate samples with H_3PO_4 at 25 °C in closed reaction vessels before transferring the product CO_2 to a purification line and mass spectrometer analysis (Ghosh et al. 2006, 2007). Sample reaction at this temperature is extremely slow, requiring 18-36 hours for the common carbonate minerals calcite and aragonite (Ghosh et al. 2006, Wacker et al. 2013), and significantly longer (weeks to months) for minerals such as dolomite and siderite. Reaction times can be reduced to 15-60 minutes by raising the temperature of phosphoric acid digestion. Unfortunately, this also results in an increase in the partial pressure of H_2O vapor which can lead to exchange with the evolved CO_2 and change the ^{13}C-^{18}O bond abundance. Samples reacted at temperatures above 25 °C must be corrected to the 25 °C reference reaction temperature (Passey et al. 2010) by use of a temperature dependant fractionation factor to allow the data to be placed on the Absolute Reference Frame (ABS, Dennis et al. 2011). Only in this fashion can

meaningful comparisons between laboratories using different reaction temperatures be undertaken.

Wacker et al. (2013) remains the only study that has examined in detail the issue of phosphoric acid digestion for clumped isotope analysis. In their analysis, Wacker et al. (2013) examined the use of two different reaction mechanisms, the common acid bath at 90 °C and the sealed reaction vessel at 25 ° C, and found better reproducibility for the common acid bath technique, possibly due to interaction with H_2O with the longer reaction times associated with 25 °C reactions. They also investigated the effects of mineralogy (calcite and aragonite) and sample size on phosphoric acid digestion, and found that both minerals behave identically, while increasing sample size led to better reproducibility.

Critically, several issues remain unresolved. No study has developed an empirical fractionation factor valid across multiple temperatures, but rather simply measured the offsets between 25 and 90 °C reactions (Passey et al. 2010, Wacker et al 2013, Henkes et al. 2013). In addition, it is unclear whether all carbonate minerals should behave identically during phosphoric acid digestion. Quantum mechanical models (Guo et al. 2009) suggest that the phosphoric acid fractionation factor is mineralogy independent, yet the absolute Δ_{47} – temperature relationships should be mineralogy dependent. To date, the only experimental results for calcite and aragonite (two polymorphs of $CaCO_3$) show that they behave differently during acid fractionation (Wacker et al. 2013). Whether this extends to other carbonate minerals with different dominate cations and crystal structures (eg dolomite, $CaMg(CO_3)_2$) remains to be investigated and is addressed by this study.

A third and more significant issue revolves around the many different published Δ_{47} – temperature relationships. Calibrations based on analyses performed at 25 °C reaction temperatures are seemingly offset from those based on higher reaction temperatures (Tang et al. 2014, Fernandez et al. 2014, Zaarur et al. 2013). The phosphoric acid fractionation factor could possibly account for some of the variation among these different calibrations. In this study we empirically determine the temperature dependence of the acid fractionation factor and clarify its role in explaining difference between these calibrations by recalculating previously published data using a common acid fractionation factor. We also present new data from inorganic precipitation experiments, including the first reported inorganic aragonite Δ_{47} – temperature calibration.

2.3 Materials and Methods

2.3.1 Phosphoric Acid Fractionation Samples

We used four different sample materials to assess the effects of mineralogy and isotopic composition on Δ_{47} fractionation caused by phosphoric acid digestion of carbonates.

- Carrara Marble, a commonly used isotope standard distributed by the IAEA.
- Joulters Cay Ooids are Holocene aragonitic ooids that were collected from Joulters Cay, Bahamas, and formed in waters with a mean annual temperature of ~22 °C.
- *Adamussium Colbecki* (Adamussium in text) is a calcitic Antarctic scallop, and was live collected at ~ 30 meters depth from Granite Harbor, McMurdo Sound in 1986 (Barrera et al. 1990), and grew at an average temperature of ~-1.8 °C.

- SRM 88b Limestone is a dolomite standard available from the National Institute of Standards and Technology (NIST) that is used as a standard for trace metal analysis. It was chosen since there are no commonly used dolomite stable isotope standards.

All samples except SRM 88b were prepared by crushing and powdering using a mortar and pestle. SRM 88b comes in powder form from NIST, and was used without any special treatment.

2.3.2 Inorganic Precipitation Experiments

Calcite and aragonite samples were synthesized in the laboratory using three different precipitation techniques: 1) The forced degassing technique (Ghosh et al. 2006, Kim and O'Neil, 1997); 2) Natural degassing technique (Dennis and Schrag, 2010, Kim et al. 2007); and 3) A daily addition/degassing technique.

The forced degassing technique has been well established in studies investigating the $\delta^{18}O$ fractionation in carbonates (Kim and O'Neil, 1997). Solutions were prepared by dissolving $NaHCO_3$ and $CaCl_2$ in deionized H_2O, and supersaturated by bubbling CO_2 gas through the solution for a period of at least one hour. The solutions were then sealed and placed in a heating/chilling water bath at the desired temperature, and N_2 bubbled through to remove dissolved CO_2 and promote precipitation. The solution was isolated from the atmosphere and dehydration by bubbling the N_2 through additional deionized H_2O both upstream and downstream of the precipitating solution. It proved to be very difficult to control the rate of degassing with the regulators and materials on hand, which resulted in disequilibrium precipitation and multiple carbonate phases within a single sample. As such, this method was abandoned and the resulting precipitates were not included in this study.

Natural degassing techniques involve supersaturating a solution with respect to calcium carbonate, and then allowing CO_2 to freely degas to the atmosphere which promotes precipitation (Dennis and Schrag, 2010). Two solutions were prepared with one solution consisting of $NaHCO_3$ dissolved in 3600 mL of deionized water, and the other consisting of $CaCl_2$ dissolved in 400 mL of deionized water. $MgCl_2$ was added to the $CaCl_2$ solution in a 4:1 ratio of Mg:Ca for aragonite precipitations at temperatures of 50 °C and below, as high Mg in solution promotes the formation of aragonite over calcite (Morse et al., 1997). Both solutions were placed in a water bath at controlled temperatures, and allowed to equilibrate for 48-72 hours before starting the reaction by adding the $CaCl_2$ solution into the $NaHCO_3$ solution. All solution and temperature data is presented in Table 1. The final mixture was allowed to naturally degas and precipitate for a period of up to several weeks after which the solution was filtered to recover all of the precipitates. These precipitates consisted of both floating crystalline mats as well as crystals growing directly on the glass surface of the precipitation vessel which were removed from the vessel by a metal spatula. Subsequently, the recovered precipitate was crushed via mortar and pestle to an even fineness and examined with XRD to determine mineralogy. Only samples of pure calcite or aragonite were used for additional analysis, any mineralogical mixtures were discarded and the precipitation repeated.

The final method utilized was a combination of a natural degassing and constant addition method. This method was only used once to produce a large quantity of calcite at 5 °C, as we had difficulty producing enough material for clumped isotope analysis at this temperature despite repeated attempts. $NaHCO_3$ was dissolved in 3600 mL of deionized water, and placed in a water bath at 5 °C. $CaCl_2$ was dissolved in 400 mL of deionized water, and also equilibrated at 5 °C. After both solutions had equilibrated for 10 days, 1 mL of the $CaCl_2$ solution was added daily to

the $NaHCO_3$ solution. The $NaHCO_3$ solution was open to the atmosphere during this precipitation to allow natural degassing as the solution precipitated. This precipitation experiment lasted from January 11th 2012 until December 20th 2012, with removal of precipitate taking place on February 20th, March 28th, and December 20th. Only the precipitate removed on February 20th was used for this study. Water samples taken at the same time as the removal of precipitate confirmed equilibrium with respect to $\delta^{18}O$.

2.3.3 Acid Digestion

105 wt. % Phosphoric acid was used in all experiments, and was prepared by hydrating $H_6P_4O_{13}$. $H_6P_4O_{13}$ was heated on a hot plate with stir bar while H_2O was added until the mixture reached a density of 1.92 g/ml. The density was checked by removing an aliquot of acid and allowing it to cool to room temperature before measuring to ensure accuracy.

Carbonate digestions at 25 °C were performed in offline sealed reaction vessels. Carbonate samples ranging from 4-6 mg in size were loaded into one arm of the reaction vessel, and 2-4 ml of 105% phosphoric acid was loaded into the other arm (Ghosh et al. 2006). The vessels were evacuated to high vacuum for at least two hours after loading by use of an oil diffusion pump, and then allowed to equilibrate overnight in a water bath with shaker held at 25 °C. The phosphoric acid was added to the sample powder to start the reaction, and the vessels were returned to the water bath. $CaCO_3$ samples were reacted at least 24 hours until completion. $CaMg(CO_3)_2$ samples were reacted for one week before CO_2 was cryogenically extracted and cleaned using the same extraction/purification line used for all other reaction temperatures.

Carbonate digestions at all other temperatures (50, 60, 75, and 90 °C) were performed using a common acid bath attached to an extraction/purification line customized exclusively for

clumped isotope analysis (Figure 2.1). All precipitate samples were digested at 75 °C. 4-6 mg of powdered sample were loaded into a carousel and individually dropped into the common acid bath reaction chamber. The reaction chamber is kept at a constant temperature by an enclosing glass envelope filled with circulating water from a heated water bath, which allowed precise temperature control. Extracted CO_2 and byproduct H_2O were simultaneously frozen in a U-trap connected to the reaction chamber by liquid N_2 (LN_2 hereafter) to minimize isotopic exchange with evolved H_2O, this U-trap was open to the reaction chamber throughout the digestion process. Acid digestion times varied depending on mineralogy and reaction temperature, generally $CaCO_3$ samples took 10-20 minutes to react to completion, while $CaMg(CO_3)_2$ samples took 1-4 hours. Reaction progress was judged based on observation of the reaction chamber and determination that no more CO_2 bubbles were forming.

2.3.4 CO_2 cleaning

CO_2 was extracted and purified using the customized vacuum line (Figure 2.1). Samples reacted at 25 °C were introduced into the line using an external port. Sample CO_2 was trapped in the first of two U-traps using LN_2, along with any H_2O present from the digestion. CO_2 was subjected to two stages of cryogenic separation (Isopropol alcohol/LN_2 traps at -95 °C, 4 minute transfer time) to remove H_2O. Dehydrated CO_2 was then cleaned using either a GC column (Supelco Supel-Q PLOT, 30m x 0.53mm) (prior to July 2011) or a 6 mm diameter glass U-trap filled with PoraPak Q material (Waters Corp., 50-80 mesh) (July 2011 and later dates). Samples cleaned using the GC column were entrained in a helium carrier gas flowing at 7 mL/minute at a temperature of -20 °C, and were collected downstream of the GC column by LN_2 in a multi-loop trap. Samples cleaned using the PoraPak were frozen into a coldfinger upstream of the PoraPak U trap, warmed to room temperature, and then allowed to equilibrate for 5 minutes with the

Figure 2.1: Extraction Line Design

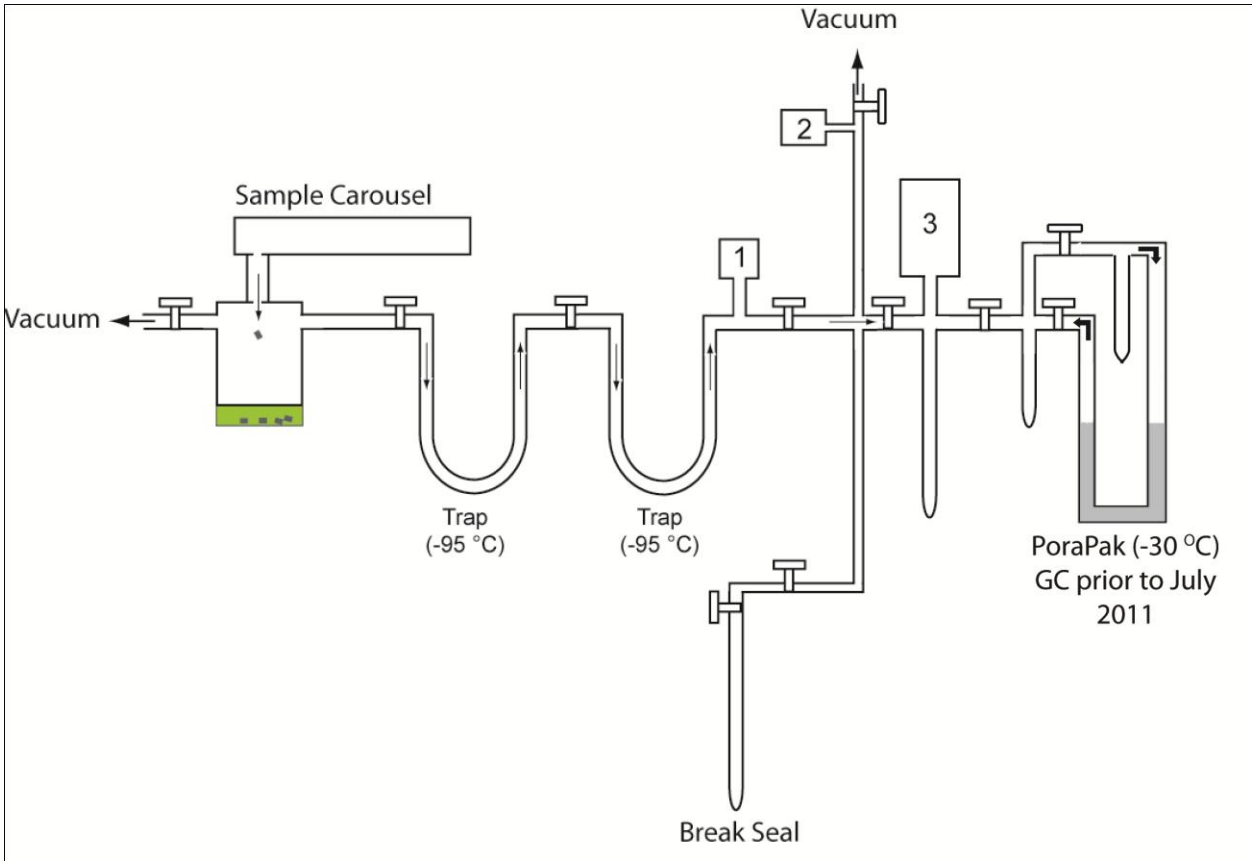

Figure 2.1 Notes: Extraction Line Diagram. 1, 2, and 3 are locations of Pirani gauges.

PoraPak held at -30 °C. LN_2 was then placed on a coldfinger downstream of the PoraPak trap, and the sample CO_2 was cryogenically drawn through the trap for 15 minutes without the use of a carrier gas. Yields were checked before and after this step using an electric manometer to ensure complete transfer of the sample to minimize fractionation during the cleaning process. Samples with incomplete transfer yields were discarded. Cleaned CO_2 was then transferred to a glass 6mm break seal for storage until analysis on the mass spectrometer, and samples were analyzed within 24 hours of extraction. CO_2 equilibrated with H_2O at 25 and 50 °C (see section 2.3.6 Data Processing) was cleaned using the same procedures as sample CO_2 outlined here.

2.3.5 Measurements

Sample and equilibrated gas CO_2 (see Data Processing) were analyzed at the University of Michigan Stable Isotope Laboratory using a Thermo-Finnigan MAT 253 dual inlet mass spectrometer that has been specially configured to collect masses 44-49 (Huntington et al. 2009). Analyses were performed in dual inlet mode with the pressure balanced to achieve 16 volts on the mass 44 cup. Measurements for $\delta^{18}O$, $\delta^{13}C$, and Δ_{47} were taken simultaneously as described by Huntington et al. (2009). Each measurement consisted of 80 cycles of sample-standard comparison, with an 8 second integration time and 16 second changeover delay, for a total of 640 seconds of integration time per sample replicate. The pressure was rebalanced every 10 cycles during an analysis. Both $\delta^{18}O$ and $\delta^{13}C$ are measured on the VPDB scale as determined using a pre-calibrated CO_2 tank (Matheson Corp.) as the reference gas ($\delta^{13}C$ = -3.70 VPDB, $\delta^{18}O$ = 34.99 VSMOW), whose composition has been determined through comparison with NBS standard gases and CO_2 evolved by acid digestion from NBS-19 and NBS-18. The total measurement time for each analysis was approximately 3 hours per sample, with a minimum of three replicate analyses for each sample.

2.3.6 Data Processing

Δ_{47} data is reported using the Absolute Reference Frame (ARF) of Dennis et al. (2011). Raw Δ_{47} data are treated to correct for non-linearities in the mass spectrometer and to scale absolutely to the ARF to allow for interlaboratory comparison. This requires the construction of an Empirical Transfer Function (ETF, Dennis et al. 2011), which allows data to be placed in the ARF. Standardization was performed by preparing a suite of CO_2 gasses of different bulk compositions that were equilibrated at fixed temperatures and used to correct for source non-linearity and scale compression (Dennis et. al., 2011). Heated gas CO_2 was baked in quartz tubes at 1000 °C for 2 hours and immediately quenched at room temperature to create a stochastic standard baseline. CO_2 gas was equilibrated with H_2O of varying isotopic composition at 25 °C and 50 °C for a minimum of 3 days before extraction. All of these prepared standard gases were subjected to the same cleaning procedures as samples unknowns to ensure that H_2O and other contaminants were removed. This also has the benefit of incorporating any potential fractionations caused by the preparation procedure into the ETF, which subsequently accounts for any systematic effects (see Discussion). The standard gases were used to construct the ETF, with slope and intercept values determined using the statistical package R (R Development Core Team, 2011). A unique ETF was calculated for discrete time intervals during which measurements were being made and standard values were consistent. Two standard gases were run daily during clumped isotope acquisitions, intersperced with sample unknowns.

2.3.7 Recalculation of Δ_{47}-Temperature Calibrations

Data from previously published Δ_{47}-temperature calibrations (Ghosh et al. 2006, Ghosh et al. 2007, Came et al. 2007, Tripati et al. 2010, Zaarur et al. 2013, Eagle et al. 2010, Dennis and

Schrag 2010, Henkes et al. 2013, Eagle et al. 2013, Tang et al. 2014, Fernandez et al. 2014, Dennis et al. 2013, Saenger et al. 2012, Zaarur et al. 2011, this study) were compiled in a single database, and all points were weighted based on the number of replicate analyses performed. Only data that could be placed on the absolute reference frame (Dennis et al. 2011) were included; this resulted in 746 data points when counting each replicate analysis individually. The unique phosphoric acid fractionation factor that was used in each study was mathematically removed. This was replaced with the phosphoric acid fractionation factor calculated in this study, based upon the reaction temperature employed for each dataset. Using this consistently corrected dataset, regression analyses were performed using the R statistical package. Statistical analysis of the regression parameters was performed to determine if applying a single acid fractionation factor resolved the observed differences among the published calibrations. This approach has the advantage in that all results are statistically treated in the same way, which eliminates a degree of uncertainty when comparing different datasets.

2.4 Results

2.4.1 Phosphoric Acid Digestion Results

$\delta^{18}O$, $\delta^{13}C$, raw and corrected Δ_{47} results, as well as the ETF used for each sample are reported in Appendix 1. Errors are reported as plus/minus one standard error, which is based on external error between replicates. No difference is seen between samples purified using the GC versus PoraPak. For all four sample materials, lower corrected Δ_{47} values are associated with higher phosphoric acid digestion temperatures. The average difference between reactions at 90 °C and 25 °C was 0.088‰ for Adamussium, 0.074‰ for Carrara Marble, 0.089‰ for Joulter's Cay Ooids, and 0.079‰ for SRM 88b.

We constructed linear regressions for each sample material to evaluate the relationship between Δ_{47} values at the different reaction temperatures. These regressions are plotted in figure 2.2, it is apparent from visual inspection that all four sample materials have similar slopes. To evaluate the degree of similarity among the regression relationships, an ANCOVA was performed. The results reveal that there is no measurable difference in the slopes ($p = 0.701$, reject multiple slope hypothesis unless $p \leq 0.05$) of the four sample materials, which indicates that calcite, aragonite and dolomite all behave similarly during phosphoric acid digestion. We grouped all of the data from all sample types to calculate the phosphoric acid fractionation factor for Δ_{47}, and the resulting equation is:

$$1000 \ln \propto_{[Reaction\ T-25C]} = \frac{(0.022434 \pm 0.001490) * 10\text{^}6}{T^2} - (0.2524 \pm 0.0168) \quad (2.3)$$

Where T is acid digestion temperature in degrees Kelvin, and the errors are one standard error.

2.4.2 Inorganic Precipitation Results

$\delta^{18}O$, $\delta^{13}C$, and Δ_{47} results for our precipitation experiments are presented in Table 2.1 and Figure 2.3. Δ_{47} values for calcite samples ranged from 0.593 to 0.745‰ for individual replicate analyses, while aragonite samples ranged between 0.580 and 0.806‰. We calculated linear regressions for the calcite data, aragonite data, and data from both mineralogies combined:

Calcite: $\Delta_{47} = \frac{(0.03155 \pm 0.00293) \times 10^6}{T^2} + (0.3331 \pm 0.0313)$ R^2=0.8847 (2.4)

Aragonite: $\Delta_{47} = \frac{(0.03817 \pm 0.00334) \times 10^6}{T^2} + (0.2727 \pm 0.0355)$ R^2=0.8899 (2.5)

All Data: $\Delta_{47} = \frac{(0.03484 \pm 0.00229) \times 10^6}{T^2} + (0.3031 \pm 0.0244)$ R^2=0.8778 (2.6)

Table 2.1: Precipitation Data

Date	Mineralogy	T °C	Ω (Calcite)	$CaCl_2$ mol/L	$NaHCO_3$ mol/L	$MgCO_3$ mol/L	$\delta^{18}O$	$\delta^{13}C$	Δ_{47}
1/11/2012[a]	Calcite	5	N/A	0.27	0.027	0	-6.79±0.21	-5.68±0.06	0.7400±0.0030
1/12/2011	Calcite	25	14.79	0.0035	0.0035	0	-10.84±0.14	-4.93±0.11	0.6953±0.0131
3/24/2014	Calcite	50	7.94	0.02	0.002	0	-15.75±0.07	-3.72±0.05	0.6195±0.0082
9/27/2013	Calcite	70	7.4	0.014	0.0014	0	-14.79±0.06	-4.62±0.05	0.6100±0.0089
11/19/2013	Aragonite	5	8.13	0.07	0.007	0.3	-4.62±0.08	1.09±0.08	0.7653±0.0174
10/17/2013	Aragonite	25	11.75	0.06	0.006	0.24	-8.18±0.09	-0.55±0.06	0.7090±0.0078
3/14/2014	Aragonite	50	10.71	0.04	0.004	0.16	-14.40±0.14	-2.81±0.07	0.6265±0.0056
3/20/2011	Aragonite	70	14.12	0.018	0.0018	0	-16.97±0.15	-2.77±0.08	0.6053±0.0114

Table 2.1 Notes: Precipitation experimental conditions and stable isotope results. a: Constant addition method, material collected 2/20/2012.

Figure 2.2: Comparison of Acid Effects on Δ_{47}

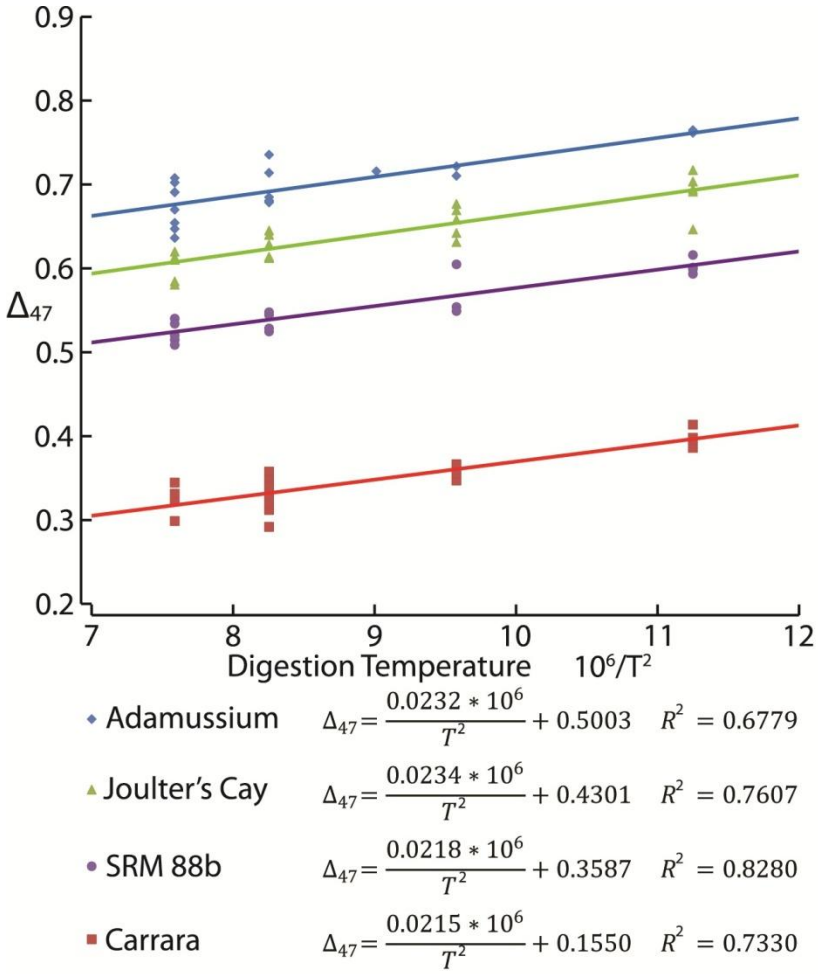

Figure 2.2 Notes: Δ_{47} results at different phosphoric acid digestion temperatures, plotted with least-squares regression lines for each sample type. Each point on the graph represents one replicate analysis, each replicate was weighted equally for regressions and statistics. Note that some points overlap.

Figure 2.3: Comparison of Δ_{47}-Temperature Calibrations

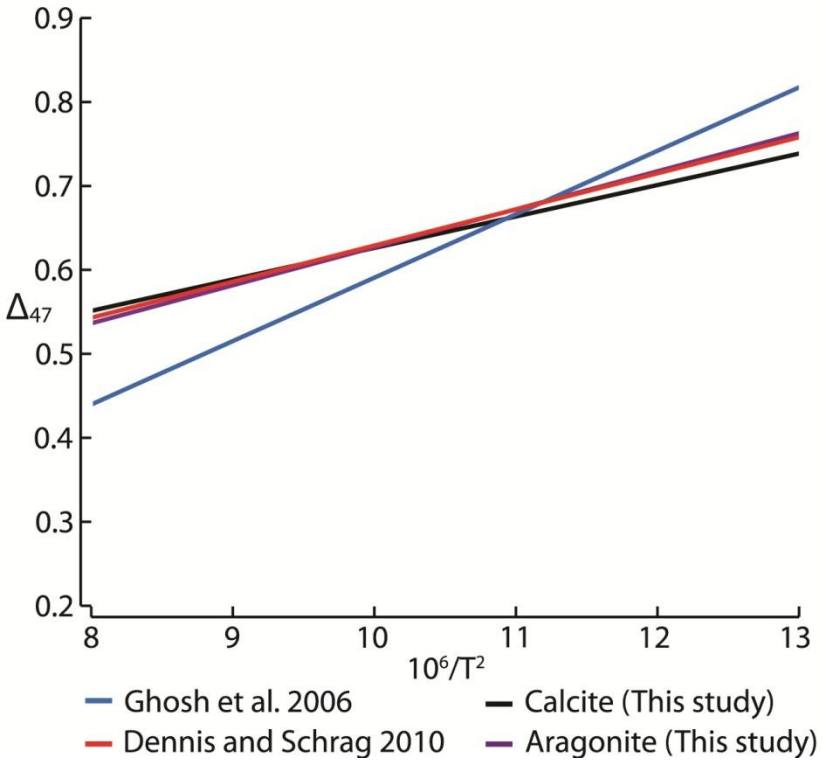

Figure 2.3 Notes: Δ_{47}-temperature calibrations produced from precipitation experiments compared to previously published calibrations.

2.4.3 Recalculated Temperature Relationships

Δ_{47}-temperature calibrations recalculated using our common acid fractionation factor (data in Appendix 2) are reported in Table 2.2 and shown in Figure 2.4. There is a clear difference between data from 25 °C reaction temperatures and data from higher temperatures; however there is no statistical difference between the 75 °C data and 90 °C data. 100 °C data falls on a similar slope as the 75 and 90 °C data, however the intercept is significantly different (0.2782±0.0115 for 75 and 90 °C versus 0.1561±0.0108 for 100 °C, errors are one S.E.). This may be a influence of mineralogy, as the only reported data analyzed at 100 °C is siderite ($FeCO_3$, Fernandez et al. 2014), and all other data consists of the various $CaCO_3$ polymorphs.

2.5 Discussion

2.5.1 Acid Fractionation Effects on Δ_{47}

The most significant finding in our study is that calcite, aragonite, and dolomite respond similarly during phosphoric acid digestion. Guo et al. (2009) suggested that the critical step in phosphoric acid fractionation for ^{13}C-^{18}O bond behavior occurs after the dissociation of the cation and the carbonate ion, our results support this model and suggest that the cation composition and crystal lattice configuration has no measurable effect on Δ_{47} during digestion. While we did not analyze every carbonate mineral potentially used for clumped isotope analysis, such as siderite (Fernandez et al. 2014), it is expected based on our results that they would likely behave similarly to the minerals analyzed here.

The earlier study of Wacker et al. (2013) reported slight differences between calcite and aragonite; however our data do not support such a conclusion. Our statistical analysis using an ANCOVA considered two models: 1) slope of raw Δ_{47} versus reaction temperature depended on

Table 2.2: Recalculated Calibration Regressions

Name	Slope * $10^6/T^2$	standard error	Intercept	standard error	R^2	n
Defliese All Data	0.03484	0.00229	0.3031	0.0244	0.8778	33
Defliese Calcite Only	0.03155	0.00293	0.3331	0.0313	0.8847	16
Defliese Aragonite Only	0.03817	0.00334	0.2727	0.0355	0.8899	17
All Data	0.04317	0.00109	0.2022	0.0129	0.6779	746
25C Data	0.06110	0.00274	-0.0049	0.0315	0.7203	195
75C Data	0.03484	0.00229	0.3031	0.0244	0.8778	33
90C Data	0.03749	0.00109	0.2727	0.0131	0.7007	506
100C Data	0.03568	0.00105	0.1561	0.0108	0.5370	12
All Data no 25C	0.04013	0.00117	0.2387	0.0139	0.6825	551
All Data 75C + 90C	0.03703	0.00097	0.2782	0.0115	0.7316	539
Biogenic	0.04431	0.00148	0.1907	0.0178	0.6156	561
Biogenic no 25C	0.03704	0.00156	0.2811	0.0190	0.5912	394
Synthetic	0.03951	0.00201	0.2364	0.0224	0.6776	185
Synthetic no 25C	0.03701	0.00218	0.2607	0.0243	0.6482	157
Calcite	0.04038	0.00141	0.2460	0.0169	0.7496	276
Calcite no 25C	0.03707	0.00167	0.2829	0.0202	0.7206	191
Aragonite	0.04305	0.00172	0.1932	0.0205	0.6522	336
Aragonite no 25C	0.03806	0.00161	0.2526	0.0196	0.7038	236
Siderite	0.03568	0.00105	0.1561	0.0108	0.5370	12
Biogenic Calcite	0.03919	0.00167	0.2688	0.0203	0.7629	174
Biogenic Calcite no 25C	0.02959	0.00212	0.3886	0.0262	0.6503	107
Synthetic Calcite	0.03664	0.00211	0.2752	0.0246	0.7487	102
Synthetic Calcite no 25C	0.03383	0.00194	0.3035	0.0227	0.7849	84
Biogenic Aragonite	0.04683	0.00194	0.1465	0.0233	0.6468	319
Biogenic Aragonite no 25C	0.04106	0.00198	0.2185	0.0243	0.6638	219
Synthetic Aragonite	0.03817	0.00334	0.2727	0.0355	0.8899	17

Table 2.2 Notes: Results of reanalysis of all published data, as well as data reported in this study. n = number of replicates used to create each regression.

Figure 2.4: Recalculated Δ_{47}-Temperature Calibrations

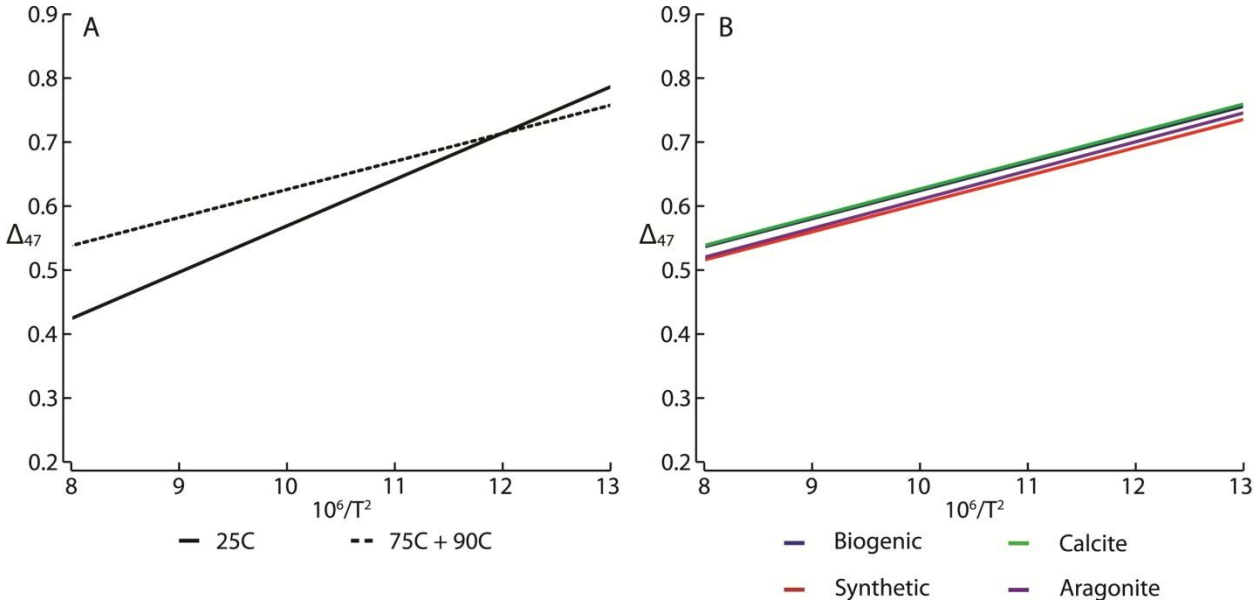

Figure 2.4 Notes: Recalculated Δ_{47}-temperature calibrations from literature data. A: 25C data and data produced at higher temperatures follow different calibrations. B: Subsets of the combined 75C and 90C data, which do not show significant differences between them.

sample type, and 2) slope was independent of sample type. We find no significant correlation between slope of raw Δ_{47} versus reaction temperature and sample type, suggesting that mineralogy does not play a significant role in phosphoric acid digestion. This may be due to current limitations on mass spectrometer sensitivity and counting statistics, and the possibility exists that further technological innovation will reveal small differences between minerals.

Prior work (Guo et al. 2009, Passey et al. 2010, Wacker et al. 2013, Henkes et al. 2013) has reported phosphoric acid fractionation as a fixed offset from the raw Δ_{47} value at a given temperature. Our result, while presented in α form, can be effectively used the same way as the range of reported Δ_{47} values in the literature is very narrow (approximately 0.3-0.8‰), and compositional effects are well below measurement errors and counting statistics (Huntington et al. 2009). We calculate a phosphoric acid correction compared to digestion at 25 °C of 0.038‰ at 50 °C, 0.067‰ at 75 °C, and 0.082‰ at 90 °C reactions, respectively. Prior work has only measured for a 90 °C reaction temperature, our value falls in the middle of reported values, which range from 0.066‰ to 0.096‰ as summarized in Wacker et al. (2013).

Wacker et al. (2013) reported a sample size effect on reactions at 25 °C, suggesting that analyses performed with less than 7 mg of sample exhibited increased variation compared to sample sizes of 7 mg or larger, or when compared to reactions at 90 °C. Our analyses were performed in 2010 and 2011, before the publication of Wacker et al. (2013); as such all of our samples are in the range of 4-6 mg, and none were over 7 mg as recommended. We do not see increased variation among analyses at 25 °C compared to reactions run at other temperatures; in fact three out of our four sample materials exhibit the smallest external standard error at 25 °C when compared to other reaction temperatures. The reasons for this difference are unclear, but our results do not show any loss of precision related to sample size at 25 °C.

We also investigated possible Δ_{47} size effects on phosphoric acid digestion, i.e. samples with larger Δ_{47} values fractionate more than samples with smaller Δ_{47} values. For this test we used two calcite samples, Cararra Marble and *Adamussium*. Our statistical approach utilized an ANCOVA which indicates no significant effect of different bulk Δ_{47} values on phosphoric acid digestion, consistent with quantum mechanical models (Guo et al. 2009). Similar to our results comparing mineralogy, further developments in mass spectrometer resolution and precision may eventually reveal slight dependencies on absolute Δ_{47} values, however we find no evidence that such effects are significant at present.

2.5.2 Empirical Calcite and Aragonite Δ_{47}-Temperature Calibration

We have produced both a calcite and aragonite Δ_{47}-temperature calibration based on synthetic carbonate produced in the laboratory. The slope of our calcite calibration is very similar to the slope reported in Dennis and Schrag (2010), and our aragonite calibration is very similar to previously published data. There is no reason to suspect that our precipitates are out of equilibrium with respect to Δ_{47}, as our data closely matches previous results and prior work has indicated that Δ_{47} should be relatively insensitive to precipitation rate and method (Tang et al. 2014). We do not see a significant difference between the calcite and aragonite produced by natural degassing in the lab, and combine all of our data into a single temperature calibration, which is statistically indistinguishable from other calibration studies produced at higher acid digestion temperatures.

2.5.3 Reconciling Δ_{47}-Temperature Calibrations

Similar to past results (Tang et al. 2014, Fernandez et al. 2014, Eagle et al. 2013, Henkes et al. 2013), applying a common acid fractionation factor does not resolve the discrepancy

between digestions at 25 °C versus higher temperatures (Table 2.2). We find that there is no statistical difference between data produced at 75 versus 90 °C after appropriate acid fractionation factors are applied, which indicates that the problem is likely not related to the temperature of reaction but rather reflects some other laboratory procedural differences. Restricting data to values reported solely on the absolute reference frame (Dennis et al. 2011) does not resolve the issue either, but reinforces the idea that the problem lies not in standardization or the phosphoric acid fractionation factor, but there is an procedural difference responsible for the discrepancy. As currently recognized, the phosphoric acid fractionation factor (Guo et al. 2009, this study) cannot be responsible for different slopes of temperature calibrations as it should only affect the intercept. There is a difference in intercept between the 75 and 90 °C data and the 100 °C data, however since the data from 100 °C is purely siderite and the data from cooler temperature $CaCO_3$ polymorphs, it is impossible to determine if that offset is caused by mineralogy or as a result of higher digestion temperatures.

Combining all of the data (746 total replicate analyses), we have generated a composite calibration (figure 2.4A, table 2.2) for 25 °C (195 replicate analyses) and a combination of 75 and 90 °C (539 replicate analyses, 100 °C data was excluded for reasons outlined above). Further restricting the higher temperature data by mineralogy and material type, and synthetic (inorganic, laboratory based) versus biogenic precipitation types, we do find some small differences in the dataset. The synthetic (n=157) and biogenic (n=394) data have very similar slopes, however the intercept for the biogenic data is slightly larger than the synthetic slope (0.2811 versus 0.2607, figure 2.4B). This may arise from less exact temperature control on many of the biogenic data points, as well as the influence of minor vital effects or possible mixing of seasonal growth bands (Defliese and Lohmann, in review (this work, Chapter 3)).

Nevertheless, the two material types are very similar statistically. Calcite (n=191) and aragonite (n=236) have similar but slightly steeper slopes compared to the biogenic and synthetic calibrations, with calcite having a slightly larger intercept (0.2829 versus 0.2565, figure 2.4B). There is no evidence of any systematic bias caused by any particular group of the data, so we believe that at present it is valid to group 75 and 90 °C data together to form a composite calibration:

$$\Delta_{47} = \frac{(0.03703 \pm 0.00097) \times 10^6}{T^2} + (0.2782 \pm 0.0115) \quad R^2=0.7316, n=539 \qquad (2.7)$$

The composite calibration at 25 °C would be:

$$\Delta_{47} = \frac{(0.06110 \pm 0.002741) \times 10^6}{T^2} - (0.0049 \pm 0.0315) \quad R^2=0.7203, n=195 \qquad (2.8)$$

The data used to produce these composites comes from multiple labs and study intervals, thus minimizing the likelihood that analytical artifacts have a large effect on the calibration, as can occur with small sample sizes. At present the discrepancy between data produced at 25 °C versus higher temperatures appears to be systematic and real, necessitating the use of two distinct calibrations. We find no evidence that 'most biogenic data' fall near the original Ghosh et al. (2006) slope (Zaarur et al. 2013), but rather convincing evidence that acid digestion temperature and technique determines the appropriate Δ_{47}-temperature calibration to be used, and that the Dennis and Schrag (2010) calibration is comparable to other calibrations produced using similar techniques.

2.5.4 Vapor Pressure of Water in Phosphoric Acid

One of the critical factors affecting Δ_{47} analysis is water. H_2O can react with sample CO_2 to form carbonic acid, and in the process scramble ^{13}C-^{18}O bonds. This will result in a resetting

of temperatures, so for reproducible, reliable results, water interaction must be kept to a minimum. 105 wt. % Phosphoric acid is naturally hydroscopic at 25 °C, and will adsorb ambient H_2O produced by a reaction. However, there still exists a danger of small amounts of H_2O being present in the headspace of a reaction chamber, which could create significant offsets over the duration of a digestion (24 hours). This risk is magnified for reactions taking place at elevated temperatures, as the vapor pressure of H_2O over phosphoric acid increases with increasing temperature. We measured the vapor pressure of H_2O over 105 wt. % H_3PO_4 in a vacuum to quantify the effect of enhanced temperature on water production, and provide recommendations on how to best balance the need of high sample throughput (rapid sample reaction) versus potential exchange of CO_2 and H_2O during the digestion process.

We measured the vapor pressure of H_2O over 105 wt. % H_3PO_4 by use of our extraction line and common acid bath. The acid bath temperature was set to the desired temperature, and the line opened to vacuum to establish a baseline. Prior to our measurements, the line and acid bath were leak tested with no acid present and isolated from the vacuum; no rise in pressure was recorded above the background, which was approximately 1-2 mmHg measured using a Pirani-type gauge. The chamber was then isolated from the vacuum source, and the pressure monitored until it came to equilibrium and recorded as the vapor pressure of H_2O over 105 wt. % H_3PO_4 in a vacuum.

Vapor pressure of H_2O over 105 wt. % H_3PO_4 in a vacuum are presented in Figure 2.5. Our results show an exponential increase in the vapor pressure with increasing temperature. Most workers have favored reactions at 90 °C, however this produces approximately three times the water produced at 75 °C, and seven times what is produced at 50 °C. Proper care must be made to trap and freeze all gasses produced from phosphoric acid digestion of carbonates at

Figure 2.5: Vapor Pressure of H_2O over Phosphoric Acid in a Vacuum

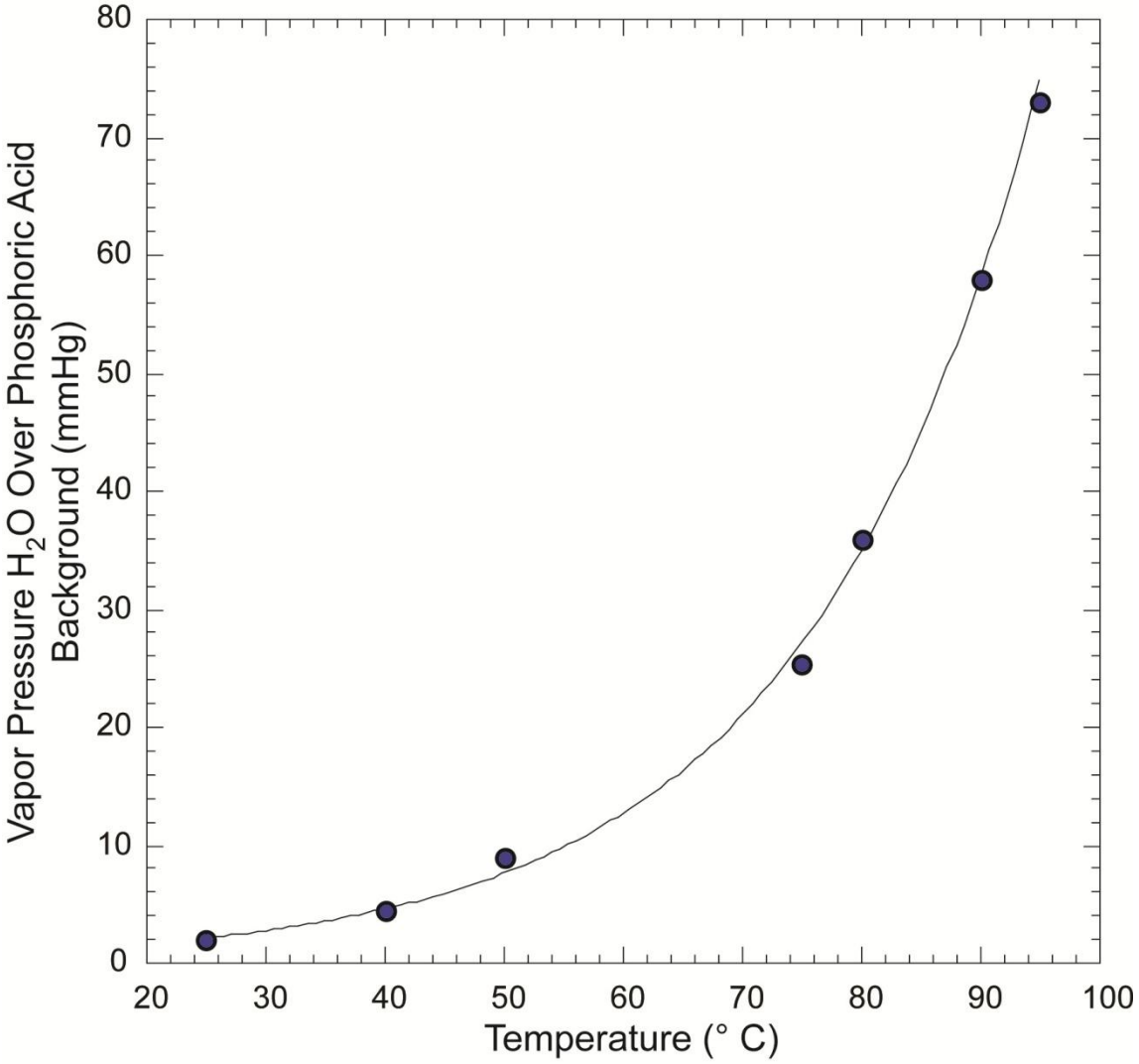

these elevated temperatures, as even the smallest amount of free H_2O can exchange with sample CO_2 and bias a Δ_{47} analysis. We recommend that all gases be frozen with LN_2 as they are produced during the reaction. Multiple steps of cryogenic separation at temperatures of -95 °C or below are necessary to remove all water from the sample, as ice begins to measurably sublimate in a vacuum above -80 to -90 °C (Murphy and Koop, 2005). We also recommend 75 °C as a reaction temperature for calcite and aragonite samples as there is not a significant increase in reaction time, but the amount of water produced is approximately three times less. Other mineralogies such as dolomite or siderite may warrant higher reaction temperatures to increase throughput due to their lower reaction speeds, but at the risk of increased water contamination.

2.6 Conclusion

The phosphoric acid digestion fractionation factor for mass-47 CO_2 produced from carbonate minerals has been empirically measured over a range of reaction temperatures. Our results suggest that calcite, aragonite, and dolomite behave identically during phosphoric acid digestion, and no difference is seen in the magnitude of the Δ_{47} offset between them between and given reaction temperature and 25 °C reaction. This suggests that the critical step during phosphoric acid digestion occurs after dissociation from the cation, and that other carbonate minerals likely fall on the same fractionation line as the three investigated here.

Placing all of the reported calibration data in a common phosphoric acid fractionation framework does not solve the issue of discrepant calibrations produced at 25 °C versus higher temperatures. We produce composite calibrations for both temperature regimes, and find that there are statistically significant correlations for 25 °C digestions as well as higher temperature digestions. Our results suggest that mineralogical and acid fractionation factor differences are

not likely the cause of discrepant calibrations, and some other methodology issue must be the cause.

We also measured the vapor pressure of H_2O above 105 wt. % H_3PO_4 in a vacuum at different temperatures, and show that the vapor pressure increases significantly at higher temperatures (eg 90 °C reactions favored by much of the community). We recommend that consideration be taken to minimize the amount of H_2O produced by phosphoric acid digestion of carbonates for Δ_{47} analysis, and that reaction temperatures above 75 °C not be used unless necessary due to mineralogy (i.e. siderite samples).

2.7 References

Barrera, E., M. J. S. Tevesz, and J. G. Carter (1990), Variations in Oxygen and Carbon Isotopic Compositions and Microstructure of the Shell of Adamussium colbecki (Bivalvia), *Palaios*, *5*(2), 149-159.

Came, R. E., J. M. Eiler, J. Veizer, K. Azmy, U. Brand, and C. R. Weidman (2007), Coupling of surface temperatures and atmospheric CO2 concentrations during the Palaeozoic era, *Nature*, *449*(7159), 198-201.

Dennis, K. J., and D. P. Schrag (2010), Clumped isotope thermometry of carbonatites as an indicator of diagenetic alteration, *Geochim. Cosmochim. Acta*, *74*(14), 4110-4122.

Dennis, K. J., H. P. Affek, B. H. Passey, D. P. Schrag, and J. M. Eiler (2011), Defining an absolute reference frame for 'clumped' isotope studies of CO2, *Geochim. Cosmochim. Acta*, *75*(22), 7117-7131.

Dennis, K. J., J. K. Cochran, N. H. Landman, and D. P. Schrag (2013), The climate of the Late Cretaceous: New insights from the application of the carbonate clumped isotope thermometer to Western Interior Seaway macrofossil, *Earth and Planetary Science Letters*, *362*(0), 51-65.

Eagle, R. A., E. A. Schauble, A. K. Tripati, T. Tütken, R. C. Hulbert, and J. M. Eiler (2010), Body temperatures of modern and extinct vertebrates from 13C-18O bond abundances in bioapatite, *Proceedings of the National Academy of Sciences*.

Eagle, R. A., et al. (2013), The influence of temperature and seawater carbonate saturation state on 13C–18O bond ordering in bivalve mollusks, *Biogeosciences*, *10*(7), 4591-4606.

Eiler, J. M. (2007), "Clumped-isotope" geochemistry - The study of naturally-occurring, multiply-substituted isotopologues, *Earth Planet. Sci. Lett.*, *262*(3-4), 309-327.

Eiler, J. M. (2011), Paleoclimate reconstruction using carbonate clumped isotope thermometry, *Quat. Sci. Rev.*, *30*(25–26), 3575-3588.

Eiler, J. M., and E. Schauble (2004), (OCO)-O-18-C-13-O-16 in Earth's atmosphere, *Geochim. Cosmochim. Acta*, *68*(23), 4767-4777.

Fernandez, A., J. Tang, and B. E. Rosenheim (2014), Siderite 'clumped' isotope thermometry: A new paleoclimate proxy for humid continental environments, *Geochim. Cosmochim. Acta*, *126*(0), 411-421.

Ghosh, P., J. Adkins, H. Affek, B. Balta, W. F. Guo, E. A. Schauble, D. Schrag, and J. M. Eiler (2006), C-13-O-18 bonds in carbonate minerals: A new kind of paleothermometer, *Geochim. Cosmochim. Acta*, *70*(6), 1439-1456.

Ghosh, P., J. Eiler, S. E. Campana, and R. F. Feeney (2007), Calibration of the carbonate 'clumped isotope' paleothermometer for otoliths, *Geochim. Cosmochim. Acta*, *71*(11), 2736-2744.

Guo, W. F., J. L. Mosenfelder, W. A. Goddard, and J. M. Eiler (2009), Isotopic fractionations associated with phosphoric acid digestion of carbonate minerals: Insights from first-principles theoretical modeling and clumped isotope measurements, *Geochim. Cosmochim. Acta*, *73*(24), 7203-7225.

Henkes, G. A., B. H. Passey, A. D. Wanamaker, E. L. Grossman, W. G. Ambrose, and M. L. Carroll (2013), Carbonate clumped isotope compositions of modern marine mollusk and brachiopod shells, *Geochim. Cosmochim. Acta*, *106*, 307-325.

Huntington, K. W., et al. (2009), Methods and limitations of 'clumped' CO2 isotope (Delta(47)) analysis by gas-source isotope ratio mass spectrometry, *J. Mass Spectrom.*, *44*(9), 1318-1329.

Kim, S.-T., and J. R. O'Neil (1997), Equilibrium and nonequilibrium oxygen isotope effects in synthetic carbonates, *Geochimica et Cosmochimica Acta*, *61*(16), 3461-3475.

Kim, S.-T., J. R. O'Neil, C. Hillaire-Marcel, and A. Mucci (2007), Oxygen isotope fractionation between synthetic aragonite and water: Influence of temperature and Mg2+ concentration, *Geochimica et Cosmochimica Acta*, *71*(19), 4704-4715.

Morse, J. W., Q. Wang, and M. Y. Tsio (1997), Influences of temperature and Mg:Ca ratio on CaCO3 precipitates from seawater, *Geology*, *25*(1), 85-87.

Murphy, D. M., and T. Koop (2005), Review of the vapour pressures of ice and supercooled water for atmospheric applications, *Quarterly Journal of the Royal Meteorological Society*, *131*(608), 1539-1565.

Passey, B. H., N. E. Levin, T. E. Cerling, F. H. Brown, and J. M. Eiler (2010), High-temperature environments of human evolution in East Africa based on bond ordering in paleosol carbonates, *Proceedings of the National Academy of Sciences*, *107*(25), 11245-11249.

Saenger, C., H. P. Affek, T. Felis, N. Thiagarajan, J. M. Lough, and M. Holcomb (2012), Carbonate clumped isotope variability in shallow water corals: Temperature dependence and growth-related vital effects, *Geochimica et Cosmochimica Acta*, *99*(0), 224-242.

Tang, J., M. Dietzel, A. Fernandez, A. K. Tripati, and B. E. Rosenheim (2014), Evaluation of kinetic effects on clumped isotope fractionation (Δ47) during inorganic calcite precipitation, *Geochimica et Cosmochimica Acta*, *134*, 120-136.

Tripati, A. K., R. A. Eagle, N. Thiagarajan, A. C. Gagnon, H. Bauch, P. R. Halloran, and J. M. Eiler (2010), C-13-O-18 isotope signatures and 'clumped isotope' thermometry in foraminifera and coccoliths, *Geochim. Cosmochim. Acta*, *74*(20), 5697-5717.

Wacker, U., J. Fiebig, and B. R. Schoene (2013), Clumped isotope analysis of carbonates: comparison of two different acid digestion techniques, *Rapid Communications in Mass Spectrometry*, *27*(14), 1631-1642.

Wang, Z. G., E. A. Schauble, and J. M. Eiler (2004), Equilibrium thermodynamics of multiply substituted isotopologues of molecular gases, *Geochim. Cosmochim. Acta*, *68*(23), 4779-4797.

Zaarur, S., G. Olack, and H. P. Affek (2011), Paleo-environmental implication of clumped isotopes in land snail shells, *Geochimica et Cosmochimica Acta*, *75*(22), 6859-6869.

Zaarur, S., H. P. Affek, and M. T. Brandon (2013), A revised calibration of the clumped isotope thermometer, *Earth and Planetary Science Letters*, *382*(0), 47-57.

Chapter 3

Patterns and Implications of Non-Linear Mixing on Mass-47 Clumped Isotope Thermometry

3.1 Abstract

The mass-47 clumped isotope paleothermometer is being increasingly applied to a diverse and growing set of proxy materials since its introduction in 2004. Because of the measurement limits of current mass spectrometers, large samples on the order of 5-10 mg are required for an individual analysis, with most measurements being replicated multiple times for statistical purposes, effectively requiring sample sizes of 20-40 mg. Heterogeneities within proxy materials on this sampling scale may result in the mixing of end members with differing bulk $\delta^{13}C$ and $\delta^{18}O$, which can create offsets in Δ_{47} that are not reflecting differences in temperature. A numerical model was developed to simulate the effects of such mixing on Δ_{47} and found that mixing is not linear with respect to end member Δ_{47}, but rather depends primarily on end member bulk isotopic compositions. Both positive and negative offsets from true Δ_{47} are possible depending the relationship between end members, with the result that mixing can lead to both temperature underestimates and overestimates. This mixing effect only becomes significant compared to shot noise and inherent measurement uncertainty when end member isotopic

composition differs by 2‰ or more for both $\delta^{13}C$ and $\delta^{18}O$, or when either is offset by approximately 15‰ or more. To quantify effects of mixing for future studies, it is essential that high resolution subsampling be performed on all samples likely to exhibit heterogeneities, which includes many biogenic carbonates, diagenetically altered carbonates, and pedogenic carbonates.

3.2 Introduction

Use of the mass-47 clumped isotope paleothermometer has expanded greatly in the last few years, being applied to a diverse set of proxy materials. These materials include mollusks (Zaarur et al. 2011, Henkes et al. 2013, Eagle et al. 2013), brachiopods (Came et al. 2007), corals (Ghosh et al. 2006, Thiagarajan et al. 2011), speleothems (Affek et al. 2008, Kluge and Affek 2012), foraminifera (Tripati et al. 2010), soil carbonates (Quade et al. 2007, Passey et al. 2010, Quade et al. 2013), phosphate associated carbonate (Eagle et al. 2010), and various diagenetic phases including phreatic and burial cements (Bergman et al. 2013, Budd et al. 2013) and dolomite (Bristow et al. 2011, Ferry et al. 2011). To achieve high quality measurements, counting statistics requires large sample sizes, with typical replicates of 5-15 mg being analyzed multiple times for total sample sizes of up to 50 mg (eg, Huntington et al 2009). Most of these phases show isotopic heterogeneity on a small scale, such as the seasonal growth bands in many biogenic carbonates, and multiple stages of cementation in diagenetic carbonates, soil carbonates, and speleothems. Most sampling procedures use either a drill or mortar and pestle to extract large quantities of sample powder, and combine multiple growth bands or cement layers to reach the required amount. This leads to homogenization of an isotopically heterogeneous sample, each with potentially distinct values for $\delta^{13}C$, $\delta^{18}O$, and Δ_{47}. Given that Δ_{47} is calculated relative to the sample's bulk $\delta^{13}C$ and $\delta^{18}O$, mixing phases with different compositions can have a dramatic effect on the calculated Δ_{47} values, and thus on calculated paleotemperatures.

Mixing relationships in multiply substituted isotopologues have been investigated by a number of authors, particularly focusing on the isotopologues of CO_2 (Zyakun, 2003, Eiler and Schauble, 2004, Affek and Eiler, 2006) and N_2O (Kaiser, Rockmann, Brenninkmeijer, 2003), with only a few studies briefly considering $CaCO_3$ (Bristow et al., 2011, Henkes et al., 2013). These studies have shown that mixing of two different populations of CO_2 (or N_2O) causes deviations in measured isotope ratios from what would be expected from a linear mixing model. For example, Affek and Eiler (2006) demonstrated that mixing of CO_2 from car exhaust and ambient atmosphere produced Δ_{47} offsets of up to 0.042‰ compared to a linear mixing model, while Henkes et al. (2013) suggested a maximum offset of 0.0014‰ in a hypothetical bivalve. In each of these examples, mixing would create an underestimate of the average equilibrium temperature, and is comparable or larger than typical errors for Δ_{47} measurement, such as the 0.0017‰ standard deviation reported for interlaboratory comparison of NBS-19 by Dennis et al. (2011). While it has been well documented that certain proxy materials, such as speleothems and corals, show Δ_{47} based temperatures that deviate from known average growth temperatures, the reasons for this are unclear. Several possibilities have been invoked to account for these discrepancies, such as disequilibrium precipitation, diagenetic overprinting, or biologic vital effects, but it is possible that non-linear mixing can account for some of these observed deviations.

This paper builds on the prior work with isotopologues of CO_2, and attempts to quantify the magnitude of temperature estimate bias that occurs when carbonates of different bulk isotopic composition are mixed. Specifically, we establish the scale on which mixing becomes significant compared to measurement error, and investigate whether this biasing can account for some of the discrepancies reported thus far in the literature. We establish the scale and

implications of mixing on Δ_{47} values by simulating the effects of mixing utilizing a numerical model and test it with laboratory measurements of mixtures of carbonates with divergent end member compositions.

3.3 Theory of Mixing

Prior work (Eiler and Schauble, 2004, Affek and Eiler, 2006, Bristow et al., 2011) has demonstrated that a mixture of CO_2 of different compositions mixes linearly with respect to $\delta^{13}C$, $\delta^{18}O$, δ^{45}, δ^{46}, and δ^{47}, but that Δ_{47} mixes non-linearly. Our model calculates the Δ_{47} value of a mixture by calculating the Δ_{47}, $\delta^{13}C$, $\delta^{18}O$, δ^{45}, δ^{46}, and δ^{47} of each end member relative to a working gas and instrument, assuming linear mixing of $\delta^{13}C$, $\delta^{18}O$, δ^{45}, δ^{46}, and δ^{47}; and calculate the Δ_{47} value of the mixture using these derived values. For each end member, we begin by assigning a value for Δ_{47}, $\delta^{13}C$, and $\delta^{18}O$, which is used to calculate δ^{45}, δ^{46}, and δ^{47} of the CO_2 gas produced by phosphoric acid digestion relative to a working gas. $\delta^{18}O$ values for CO_2 gas are calculated by using the phosphoric acid digestion calibration of Swart et al. (1991). $\delta^{13}C$ is assumed to not fractionate during acid digestion. The gas values of $\delta^{13}C$ and $\delta^{18}O$ were used to calculate R^{13} and R^{18} for each end member, using the absolute abundance ratios of Gonfiantini et al (1993):

$$R^{13} = \left(\frac{\delta^{13}C_{VPDB}}{1000} + 1\right) \times 0.0112372 \quad (3.1)$$

$$R^{18} = \left(\frac{\delta^{18}O_{VSMOW}}{1000} + 1\right) \times 0.0020052 \quad (3.2)$$

R^{17} was calculated based on R^{18}, using

$$R^{17} = \left(\frac{R^{18}}{0.0020052}\right)^{0.5164} \times 0.0003799 \quad (3.3)$$

The absolute abundance of each isotope was then calculated for each end member:

$$\left[^{12}C\right] = \frac{1}{1+R^{13}} \tag{3.4}$$

$$\left[^{13}C\right] = \frac{R^{13}}{1+R^{13}} \tag{3.5}$$

$$\left[^{16}O\right] = \frac{1}{1+R^{17}+R^{18}} \tag{3.6}$$

$$\left[^{17}O\right] = \frac{R^{17}}{1+R^{17}+R^{18}} \tag{3.7}$$

$$\left[^{18}O\right] = \frac{R^{18}}{1+R^{17}+R^{18}} \tag{3.8}$$

These abundances are used to calculate the stochastic distribution of isotopes, R*, which is the ratio of each isotopologue mass abundance relative to mass 44 abundance:

$$R^{45*} = \frac{\left[^{13}C\right]\left[^{16}O\right]\left[^{16}O\right]+2\left[^{12}C\right]\left[^{16}O\right]\left[^{17}O\right]}{\left[^{12}C\right]\left[^{16}O\right]\left[^{16}O\right]} \tag{3.9}$$

$$R^{46*} = \frac{2\left[^{12}C\right]\left[^{16}O\right]\left[^{18}O\right]+\left[^{12}C\right]\left[^{17}O\right]\left[^{17}O\right]+2\left[^{13}C\right]\left[^{16}O\right]\left[^{17}O\right]}{\left[^{12}C\right]\left[^{16}O\right]\left[^{16}O\right]} \tag{3.10}$$

$$R^{47*} = \frac{2\left[^{13}C\right]\left[^{16}O\right]\left[^{18}O\right]+\left[^{13}C\right]\left[^{17}O\right]\left[^{17}O\right]+2\left[^{12}C\right]\left[^{17}O\right]\left[^{18}O\right]}{\left[^{12}C\right]\left[^{16}O\right]\left[^{16}O\right]} \tag{3.11}$$

The same steps are taken for the working gas to calculate the stochastic distribution of isotopes, R^*_{WG}. δ^{45} and δ^{46} are then calculated for both end members as following:

$$\delta^{45} = \left(\frac{R^{45*}}{R^{45*}_{WG}} - 1\right) \times 1000 \tag{3.12}$$

$$\delta^{46} = \left(\frac{R^{46*}}{R^{46*}_{WG}} - 1\right) \times 1000 \tag{3.13}$$

Finally, δ^{47} was calculated for each end member by taking the Δ_{47} value for each, removing the acid fractionation offset and empirical transfer function (ETF), and making the assumption that only δ^{47} contributes to Δ_{47} measurements, as abundances of ^{17}O are very low compared to ^{18}O (Wang et al., 2004). This assumption introduces a small error in the calculations, however when mixtures of known compositions were analyzed on the mass spectrometer, the difference between the measured and calculated δ^{47} was ≤0.02‰. For each end member, using the nomenclature of Dennis et al. (2011), and with the end member values chosen for Δ_{47}, the steps were:

$$\Delta_{47[RF]} = \Delta_{47[\text{End Member Value}]} - \text{acid correction} \tag{3.14}$$

$$\Delta_{47[SGvsWG]0} = \frac{\Delta_{47[RF]} - \text{ETF}_{Int}}{\text{ETF}_{Slope}} \tag{3.15}$$

Where ETF_{Int} and ETF_{Slope} represent the intercept and slope of the empirical transfer function, $\Delta_{47[RF]}$ is the Δ_{47} value in the universal reference frame, and $\Delta_{47[SGvsWG]0}$ is the equilibrated gas corrected Δ_{47} value. δ^{47} was calculated using the following equation, whose derivation is outlined in Appendix 3:

$$\delta^{47} = \frac{(\Delta_{47[SGvsWG]0} + 1000) \times R^{47*} - 1000 \times R^{47*}_{WG}}{R^{47*}_{WG} - \text{EGL}_{Slope} \times R^{47*}} \tag{3.16}$$

Where EGL_{Slope} is the slope of the equilibrated gas lines.

For each mixture, linear mixing was assumed for $\delta^{13}C$, $\delta^{18}O$, δ^{45}, δ^{46}, and δ^{47}. Values for each mixture were calculated by

$$\delta i_{mix} = x_1 \delta i_1 + x_2 \delta i_2 \ldots + x_n \delta i_n \tag{3.17}$$

Where δ*i* represents a given component, *n* represents the end member compositions, and *x* is the fractional contribution of each end member, with $\Sigma_x=1$. From here, the normal process of calculating $R^{45}*_{mix}$, $R^{46}*_{mix}$, and $R^{47}*_{mix}$ is performed with the stochastic distribution of isotopes in the mixture based on $\delta^{13}C_{mix}$ and $\delta^{18}O_{mix}$ using equations 3.1-3.11. $\delta^{45}{}_{mix}$, $\delta^{46}{}_{mix}$, and $\delta^{47}{}_{mix}$ are used to calculate $R^{45}{}_{mix}$, $R^{46}{}_{mix}$, and $R^{47}{}_{mix}$ by the following equation:

$$R^i = \left(\frac{\delta i}{1000} + 1\right) \times R_{WG}^{i*} \tag{3.18}$$

Where *i* represents masses 45, 46 and 47. Finally, Δ_{47mix} is calculated as

$$\Delta_{47[SGvsWG]mix} = \left[\left(\frac{R^{47}}{R^{47*}} - 1\right) - \left(\frac{R^{46}}{R^{46*}} - 1\right) - \left(\frac{R^{45}}{R^{45*}} - 1\right)\right] \times 1000 \tag{3.19}$$

$$\Delta_{47[SGvsWG]0mix} = \Delta_{47[SGvsWG]mix} - \delta 47_{mix} \times EGL_{Slope} \tag{3.20}$$

$$\Delta_{47mix} = \Delta_{47[SGvsWG]0mix} \times ETF_{Slope} + ETF_{Int} \tag{3.21}$$

The choice of working gas, acid reaction temperature, and machine artifacts (taken into account with the Empirical Reference Frame) affect the calculated values for δ^{45}, δ^{46}, and δ^{47}, but do not affect the final calculated $\delta^{13}C$, $\delta^{18}O$, and Δ_{47}.

3.4 Methods

Using the technique and equations described above, a numerical model was constructed to calculate the effect of mixing of end member carbonates with differing compositions. To investigate general patterns and trends caused by mixing solid carbonates, simulations were performed representing a wide spectrum of end member compositions and equilibrium

temperatures.. For these simulations, we assumed an 'ideal' machine and working gas, with working gas composition of $\delta^{13}C$ = 0‰ VPDB and $\delta^{18}O$ = 0‰ VSMOW, ETF_{Slope} = 1, ETF_{Int} = 0, EGL_{Slope} = 0, and acid reaction at 25° C. (In practice, users should use the appropriate values for their system and operating conditions.) Under these conditions, the chosen end member value for Δ_{47} is equivalent to $\Delta_{47[SGvsWG]}$ and equations 3.14 and 3.15 are unnecessary. In addition, equation 3.16 simplifies to have the form

$$\delta^{47} = \left(\left(\frac{\Delta_{47[SGvsWG]0}}{1000} + 1\right) \times \left(\frac{R^{47*}}{R^{47*}_{WG}}\right) - 1\right) \times 1000 \qquad (3.22)$$

To test the model and these general simulations, we also analyzed two mixtures of known composition and compared them to model results (Section 3.7). Using the mass spectrometer operating conditions (working gas values, ETF, etc) and known end member values for mixtures, the model predictions were within one standard error of the measured Δ_{47} values.

3.5 Results and Discussion

3.5.1 General Patterns and Trends of Mixing

We analyzed numerous scenarios involving mixing of end members of differing bulk isotopic compositions, mixing proportions, and equilibrium temperatures. For simplicity, we chose to use three values of Δ_{47} for end members: .55198, .71324, and .77718 (corresponding to 100, 20 and 0 °C on the Dennis and Schrag (2010) temperature calibration, as corrected in Dennis et al. (2011)). We used values for $\delta^{13}C$ and $\delta^{18}O$ that ranged from +15‰ to -15‰ VPDB, and investigated the effects of each. Eight different scenarios for mixing were considered: 1) Constant Δ_{47}, with variation in $\delta^{13}C$ and $\delta^{18}O$ bulk composition with both offset in the same positive or negative direction; 2) Constant Δ_{47} and $\delta^{13}C$, but with variation in $\delta^{18}O$;

3) Constant Δ_{47} and $\delta^{18}O$, with variation in $\delta^{13}C$; 4) Constant Δ_{47}, but where $\delta^{13}C$ and $\delta^{18}O$ varied in antithetical directions; 5) Different Δ_{47} with constant $\delta^{13}C$ and $\delta^{18}O$; 6) Different Δ_{47} with variation in $\delta^{13}C$ and $\delta^{18}O$ moving in the same direction; 7) Different Δ_{47} with either $\delta^{13}C$ or $\delta^{18}O$ constant; and 8) Different Δ_{47} with variation in $\delta^{13}C$ and $\delta^{18}O$ moving in antithetical directions. Simulations were run for mixing proportions of $x = 0$ to 1 in .1 intervals, with all analyses presented in the data repository.

We introduce a new term to describe the discrepancy between Δ_{47} calculated by the model and Δ_{47} calculated from conservative linear mixing of end member values. Since Δ is already in use, we use the greek letter Γ to describe this term, with $\Gamma_{47} = \Delta_{47Model} - \Delta_{47Linear}$ (Figure 3.1). This will produce a positive value when conservative linear mixing underestimates Δ_{47}, and a negative value when linear mixing overestimates Δ_{47}. The units of Γ_{47} are equal to that of Δ_{47} and are ‰.

Several general trends are immediately clear upon reviewing the data. First, the sign of Γ_{47} is controlled by the end member values of $\delta^{13}C$ and $\delta^{18}O$, and is independent of each end member's Δ_{47} (Figure 3.2). When $\delta^{13}C$ and $\delta^{18}O$ have a positive correlation, i.e. both values for one end member are more negative than the other, Γ_{47} is positive (Figure 3.2A). Likewise, when one of either $\delta^{13}C$ or $\delta^{18}O$ is constant, and the other changes, Γ_{47} is positive (Figure 3.2B). Γ_{47} is negative when $\delta^{13}C$ and $\delta^{18}O$ show a negative correlation, i.e. when one end member has positive $\delta^{13}C$ and negative $\delta^{18}O$, and other end member has negative $\delta^{13}C$ and positive $\delta^{18}O$ (Figure 3.2C). Γ_{47} is zero and follows a linear mixing model when the end members have identical bulk isotopic compositions, regardless of Δ_{47} values (Figure 3.2D). The implications are that apparent Δ_{47} values from mixtures can be an overestimate or underestimate of true temperature conditions,

Figure 3.1: Changes in Γ_{47} as a Function of Percent Mixing

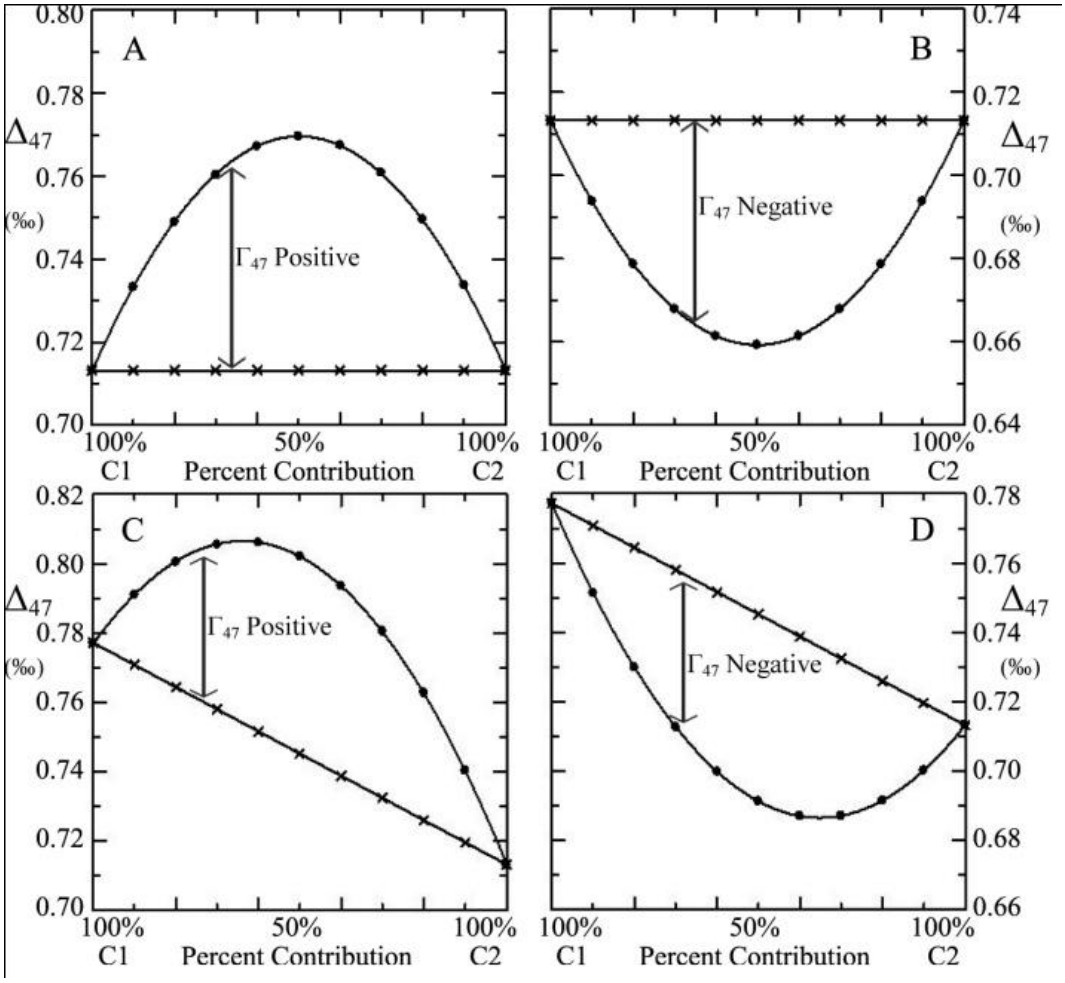

Figure 3.1 Notes: Diagram illustrating changes in Γ_{47} as a function of percent mixing. Δ_{47}-model results are given by circles, Δ_{47}-linear mixing by crosses. C1 and C2 represent different end members, in each case C1 has an isotopic composition of 0‰ for both $\delta^{13}C$ and $\delta^{18}O$, and C2 has a composition of -15‰ for both $\delta^{13}C$ and $\delta^{18}O$. A: A positive Γ_{47} offset, caused by a positive correlation between $\delta^{13}C$ and $\delta^{18}O$, causes a temperature underestimate. C1 and C2 have the same Δ_{47} value. B: A negative Γ_{47} offset, caused by a negative correlation between $\delta^{13}C$ and $\delta^{18}O$, results in a temperature overestimate. C1 and C2 have the same Δ_{47} value. C: A positive Γ_{47} offset is manifest when C1 and C2 have differing Δ_{47} values. D: A negative Γ_{47} offset occurs when C1 and C2 have differing Δ_{47} values.

Figure 3.2: Demonstration of Different Patterns of Mixing

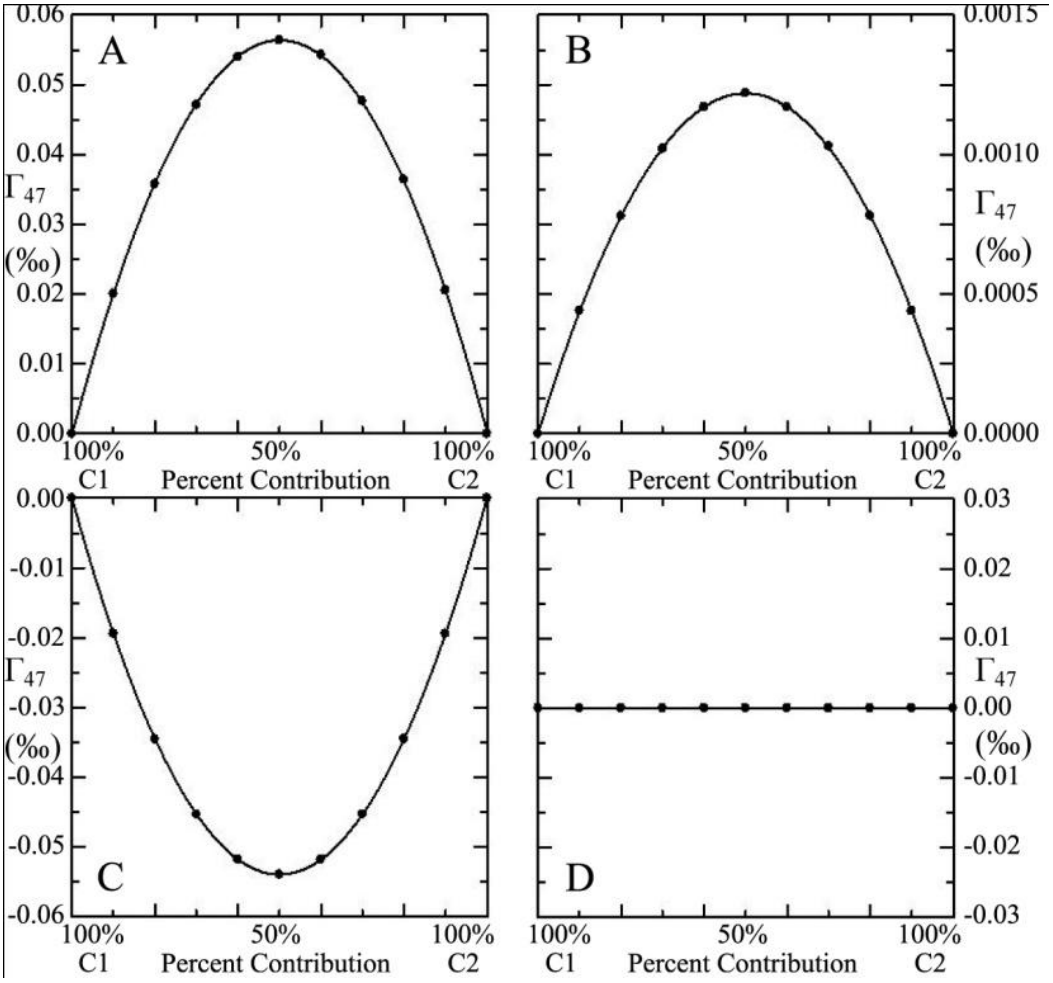

Figure 3.2 Notes: Demonstration of the different patterns of mixing, where C1 and C2 are carbonate end members with differing isotopic compositions. A: A positive Γ_{47} occurs when there is a positive correlation between $\delta^{13}C$ and $\delta^{18}O$ of the end members. In this figure, Δ_{47} is constant, and the end members differ by 15‰ in both carbon and oxygen, with a positive correlation. B: A positive Γ_{47} occurs when either $\delta^{13}C$ or $\delta^{18}O$ is constant between the end members and the other varies, the effect is much smaller in magnitude than as shown in A. C: A negative Γ_{47} occurs when there is a negative correlation between $\delta^{13}C$ and $\delta^{18}O$ of the end members. In this figure, Δ_{47} is constant, and the end members differ by 15‰ in both carbon and oxygen, with a negative correlation. D: When the two end members have the same bulk isotopic composition, Γ_{47} is zero (no mixing offset).

and deciphering which is true requires detailed knowledge of the correlation between $\delta^{13}C$ and $\delta^{18}O$ within the sample.

The magnitude of Γ_{47} is controlled by the size of the offset in $\delta^{13}C$ and $\delta^{18}O$ between end members in the mixture, as well as the percent contribution of each. In two component mixing, the maximum size of Γ_{47} is reached when each end member contributes 50% to the final mixture, regardless of the sign of Γ_{47}. A plot of Γ_{47} versus *x* has a parabolic shape, which means that even small contributions of one end member have a significant contribution. For instance, a 1% contribution of one end member with 99% of the other gives a Γ_{47} value that is approximately 3.96% of the maximum, where a 5% contribution gives a Γ_{47} that is 19% of the maximum. The maximum value of Γ_{47} depends primarily on the offset between the $\delta^{13}C$ and $\delta^{18}O$ values of each end member, with a smaller dependence on the actual value for each end member. Larger offsets between the end members leads to a larger Γ_{47} (Figure 3.3), with an offset of 15‰ for $\delta^{13}C$ and $\delta^{18}O$ having almost 9 times the Γ_{47} compared to an offset of 5‰ for both. An offset of 2‰ for both carbon and oxygen leads to a Γ_{47} of about 0.0010‰, which is comparable to the error for most measurements.

The actual carbon and oxygen value of each end member makes a much smaller but detectable difference in Γ_{47} as well. For example, a 15‰ offset with both end members having positive $\delta^{13}C$ and $\delta^{18}O$ makes for a smaller Γ_{47} than a 15‰ offset with both end members having negative $\delta^{13}C$ and $\delta^{18}O$ (Figure 3.4), and has an effect of 0.0017‰ for the case in Figure 3.4. This is due to there being many more stochastic ^{13}C-^{18}O bonds when both isotopes are abundant, which lessens the overexpression of ^{13}C-^{18}O bonds. The Δ_{47} value of each end member has an extremely small effect on the magnitude of Γ_{47}, and over the Δ_{47} values we chose had a maximum effect of about 0.0001‰, when comparing end members with Δ_{47} = 0.77718 and

Figure 3.3: Size Effects of Γ_{47}

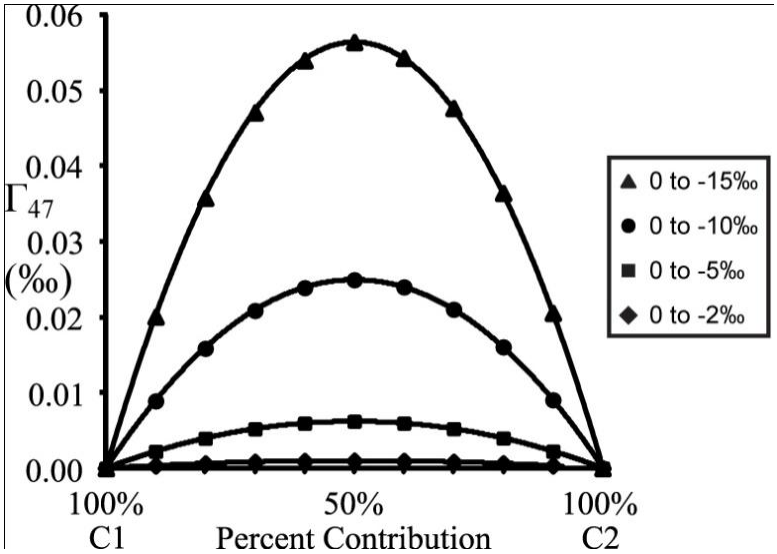

Figure 3.3 Notes: Illustration of the increasing size of Γ_{47} when the difference between end member compositions increases. In all cases, there is a positive correlation between $\delta^{13}C$ and $\delta^{18}O$. In each case, end member C1 has a composition of 0‰ for both $\delta^{13}C$ and $\delta^{18}O$, and end member C2 has a composition for both $\delta^{13}C$ and $\delta^{18}O$ of -2‰, -5‰, -10‰, and -15‰.

Figure 3.4: Effects of Isotope Abundance on Γ_{47}

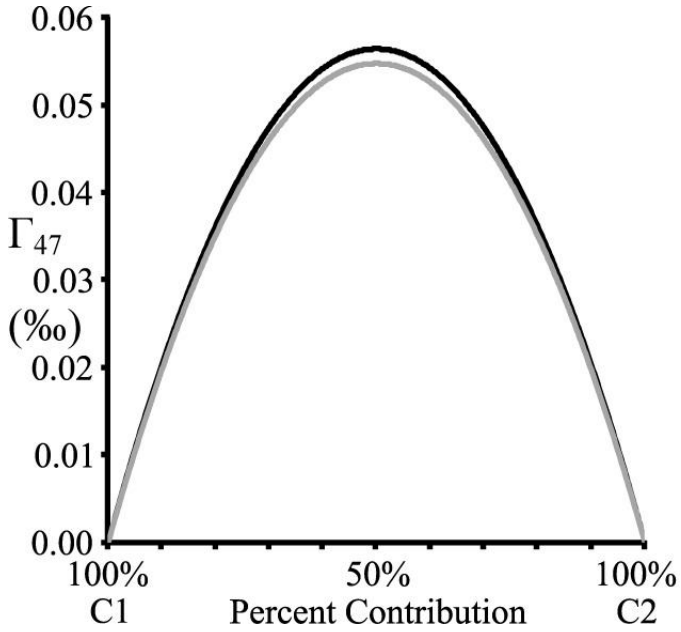

Figure 3.4 Notes: Illustration of the effect of differing absolute isotopic abundance on Γ_{47}. As there are less ^{13}C-^{18}O bonds overall, mixing creates a larger offset when they are less abundant (i.e., when both $\delta^{13}C$ and $\delta^{18}O$ are very negative, giving less ^{13}C and ^{18}O in the whole system). The black line represents mixing between end members have compositions for both $\delta^{13}C$ and $\delta^{18}O$ of 0‰ and -15‰, the light grey line represents mixing between end members having compositions of 15‰ and 0‰ for both $\delta^{13}C$ and $\delta^{18}O$.

0.55198. This value is very small, and is within the shot noise limit for Δ_{47} measurement, so it can be effectively ignored.

3.5.2 Implications for Paleotemperature Reconstructions

Our model results indicate that mixing can become a significant contribution to Δ_{47} when the sample exhibits isotopic heterogeneities on the order of ~2‰ when both carbon and oxygen vary, or ~15‰ when only one isotope is involved. Since the sign of Γ_{47} cannot be determined without knowing the correlation between $\delta^{13}C$ and $\delta^{18}O$, microsampling is necessary to determine the magnitude and sign of any effect of mixing. A review of previous studies suggests heterogeneities on the order of 2‰ or greater are likely to occur in several of the proxies commonly utilized for clumped isotope studies, including many biogenic carbonates (occurring as growth bands) (Adkins et al., 2003, Rollion-Bard et al., 2008, Yan et al., 2009, Hren et al., 2013), diagenetic carbonates (Budd et al., 2013), and pedogenic carbonates (Duetz et al., 2002). Growth bands and diagenetic carbonates are well known to have isotopic variation, which can be especially large in the case of diagenetic carbonates (eg, James and Choquette, 1990, Choquette and James, 1990). Isotopic variation in pedogenic carbonates has been much less studied in the literature, with only a few examples of studies utilizing high resolution measurements from individual soil nodules (eg, Duetz et al., 2013). Since pedogenic carbonates form over periods ranging from tens to millions of years, there is the potential for significant changes in precipitational environment recorded in a single nodule (Sheldon and Tabor, 2009). Caliche profiles are often associated with internodule variation, with reported ranges as large as 3‰ in $\delta^{18}O$ and 11.3‰ in $\delta^{13}C$ between incipient nodules formed in the same unit (Zhou and Chafetz, 2010). This amount of variability is quite large, and as such caliche is not commonly utilized by paleopedogenic studies. Intranodule variation in non-caliche profiles have been studied by only

a few authors, with variability depending on the type of soil nodule. Zhou and Chafetz (2010) found intranodule variability of up to 1.4‰ in $\delta^{13}C$ and 0.3‰ $\delta^{18}O$ in non-altered soil nodules from a caliche profile, which is too small of a variation to cause a mixing offset in clumped isotope measurements. In contrast, Bennett et al. (2012) took transects across several soil nodules from Olduvai Gorge, Tanzania, and found that all had a positive correlation between $\delta^{13}C$ and $\delta^{18}O$, with a maximum intranodule variability of up to 3.5‰ in $\delta^{18}O$ and 7.5‰ in $\delta^{13}C$. Yang et al. (2012) found a smaller variation in a single large nodule of 1.6‰ in $\delta^{18}O$ and 2.6‰ in $\delta^{13}C$, but found a nearly 1:1 negative correlation between $\delta^{18}O$ and $\delta^{13}C$. Variation exceeding 2‰ within individual nodules have also been reported by Duetz et al. (2002). These contrasting results show that intranodule variability in soil carbonates can follow either positive or negative correlations, and may be large enough to cause statistically significant offsets in measured Δ_{47} values. Further study on the issue of intranodule variation would be beneficial to both the clumped isotope community as well the broader paleopedology community, and may resolve some of the significant offsets observed between recorded temperatures and Δ_{47}-derived temperatures (eg, Quade et al., 2013).

3.5.3 Potential Effects on Clumped Isotope Temperature Calibrations

The discrepancy between the several published empirical temperature calibrations (Ghosh et al., 2006, 2007, Came et al., 2007, Tripati et al., 2010, Dennis and Schrag, 2010, Thiagarajan et al., 2011, Henkes et al., 2013, Eagle et al., 2013) and theoretical predictions (Schauble et al., 2006, Guo et al., 2009) remains a significant challenge for the clumped isotope community. This divergence has been attributed to a number of factors, such as different taxa used for the calibration or different methods of precipitating inorganic calcite, differences in reaction and measurement technique, or non-uniform standardization prior to the development of

the empirical reference frame (Dennis et al., 2011). Mixing has the potential to further complicate the results by potentially biasing calibrations that depend on organisms from different temperature and environmental conditions that experience different growth patterns, even within the same species. For example, a calibration that is based on bivalves spanning multiple localities to encompass a range in temperatures could be affected if the bivalves in one location have a negative Γ_{47} while those in a second location have a positive Γ_{47}, or different samples could have varying magnitudes of Γ_{47}. This effect, when applied over multiple locations, could potentially bias the calibration away from a 'true' calibration and account for some of the variability between studies. While such effects cannot be proven from published data, they have the potential to be a contributing factor to the calibration discrepancies.

3.6 Application of Mixing to Clumped Isotope Results

To solve for Γ_{47}, it is necessary to know both the isotopic compositions of the end members, as well as the percent contribution of each end member to the mixture. As discussed in section 4, the Δ_{47} values of the end members do not contribute significantly to Γ_{47}, so it is not necessary to know them to calculate the true temperature of the mixture (i.e., the linear Δ_{47} value of the mixture). However, if one or more end member Δ_{47} values can be constrained, estimation of remaining end member Δ_{47} value can be calculated by mixing equations, enabling the system to be solved.

3.6.1 Two Component Systems

Two component systems are easily solvable with a combination of Δ_{47} analysis, high resolution $\delta^{18}O$ and $\delta^{13}C$ measurements, and/or knowledge of percent contribution to a mixture. Calculating Γ_{47} of the mixture is straightforward, and can be accomplished in two ways: 1)

knowledge of only the $\delta^{18}O$ and $\delta^{13}C$ values of either both end members and the mixture, using eq. 17 to solve for the percent contribution of each end member; or 2) knowledge of the isotopic values of one end member and of the mixture, and the percent contribution of each end member to the mixture, then using eq. 17 to solve for the isotopic composition of the unknown end member. In practice, approach 1 is likely to be more accurate, but approach 2 can be used when phases are too small to be sampled directly, with point counting or other techniques being used to estimate percent contribution to the mixture.

Δ_{47} values for an end member can be extrapolated in a two component system with knowledge of Γ_{47} for the mixture and constraints on the other end member's Δ_{47} value. In this case, the linear Δ_{47} value of the mixture ($\Delta_{47linear}$) is known by subtracting Γ_{47} from measured Δ_{47}. $\Delta_{47linear}$ can then be used in eq. 17 along with the known end member Δ_{47} value to estimate the other end member Δ_{47} value, since the percent contribution of each end member is already known from the Γ_{47} calculation. There are numerous scenarios where this calculation might be useful, particularly in diagenetic environments where the formation temperature of one phase can be constrained by other methods (for example, fluid inclusion thermometry), and the temperature of the other phase calculated using this approach.

3.6.2 Multiple Component Systems

In the case of systems consisting of three or more components, solving for Γ_{47} requires knowledge of the end member isotopic compositions as well as an independent quantification of percent contributions to the mixture. It is possible through an algebraic approach to solve for the isotopic composition of a single unknown end member using eq. 17, however the compositions of all other end members and the percent contributions of each must be known. Solving for Δ_{47}

for the end members is impossible except in the case of a single unknown end member, in which case eq. 17 may be applied.

3.7 Empirical Test of Mixing

To validate the simulations of our mixing model, an empirical test of mixing was performed. Two mixtures were made to demonstrate a positive Γ_{47} and a negative Γ_{47}, respectively. Mixture A was chosen to create a positive Γ_{47} and consisted of a 1:1 mixture of laboratory standards Merck and Carrara Marble, while mixture B consisted of a 1:1 mixture of two field collected samples, 10SP06A (Member B, Sheep Pass Formation, Nevada, USA, Late Cretaceous – Eocene) and *Otala lactea* (Bierman's Quarry, Bermuda, the shell carbonate of a recent land snail), and was designed to create a negative Γ_{47}. Both mixtures were designed to create large Γ_{47} offsets to allow easy comparison with model results. Mixtures were prepared by weighing 50mg powder of each end member, placing both powders into a sample vial, and shaking vigorously for several minutes. Both mixtures and all end members were analyzed for $\delta^{13}C$, $\delta^{18}O$, and Δ_{47} at the University of Michigan Stable Isotope Lab. Samples were digested with 104% phosphoric acid at 75° C in a common acid bath attached to a custom built extraction line. Sample CO_2 was purified by two stages of cryogenic separation at -90° C to remove water, and remaining contaminants were removed by passing the CO_2 through a column of PoraPak Q resin held at -30° C. Purified sample CO_2 was analyzed using a Thermo-Finnigan MAT 253 mass spectrometer operated in dual inlet mode as described in Huntington et al. (2009). Samples were corrected for non-linearity and scale compression by use of an empirical transfer function as described in Dennis et al. (2011), which was constructed from standard CO_2 gases equilibrated at 25° and 1000° C.

Measured end member values for both mixtures A and B were used as inputs for the mixing model, as well as the operating conditions for the instrument during the time the samples were analyzed (October 23rd – November 5th, 2013). We used a working gas with values $\delta^{13}C$ = -3.70 VPDB, $\delta^{18}O$ = 34.99 VSMOW, the equilibrated gas slope was 0.0274 with a 1000° C intercept of -0.8885, and the empirical transfer function slope was 1.0391 with an intercept of 0.9499. We used an empirically measured phosphoric acid fractionation offset of 0.066581‰ for Δ_{47} and an α of 1.008051 for $\delta^{18}O$ to correct for digestion at 75° C. Measured and model results for both mixtures are listed in Table 3.1.

Measured Δ_{47} results for both mixtures fall within one standard error of the predicted mean model result, and errors are contained within the range of model runs (Figure 3.5). $\delta^{18}O$ and $\delta^{13}C$ results for mixture A fall slightly off of the prediction for a 50:50 mixture of end members, indicating a slight sampling bias or that the mixture was not completely homogenized. This does not significantly affect the results however, as the model accurately predicted the final Δ_{47} of each mixture. While these mixtures were specifically chosen from existing materials to create the largest possible positive and negative Γ_{47}, they illustrate the ability of end member mixing to significantly alter any interpretation that does not account for such offsets. For example, using the Δ_{47} – temperature scale of Ghosh et al. (2006), mixture B results in a 7.5° C overestimate of temperature compared to the true temperature of formation (the average of the temperatures recorded by the end members). This demonstration shows that not only does mixing in Δ_{47} not follow linear trends, but that it can significantly affect temperature reconstructions and potentially lead to temperature over- or under-estimates, particularly when proxies of highly variable isotopic composition are used.

Table 3.1: Mixing Test Results

	n[a]	Δ_{47}	$\delta^{18}O$	$\delta^{13}C$
Carrara Marble	6	0.3882±0.0094	-2.26±0.12	1.73±0.10
Merck	4	0.6090±0.0166	-15.93±0.07	-34.86±0.17
Mixture A	6	0.6414±0.0089	-9.64±0.15	-17.89±0.24
Model (Mixture A)[b]	N/A	0.6434	-9.09	-16.56
Otala lactea	4	0.6998±0.0133	-0.32±0.12	-9.79±0.01
10SP06A	4	0.6864±0.0118	-11.11±0.17	3.60±0.12
Mixture B	6	0.6531±0.0090	-5.86±0.30	-2.99±0.32
Model (Mixture B)[b]	N/A	0.6573	-5.72	-3.09

Table 3.1 Notes: Clumped isotope results and model results. All errors are 1 standard error. a: Number of replicate analyses. b: Errors and replicates are not computed for model outputs.

Figure 3.5: Mixing Test Results

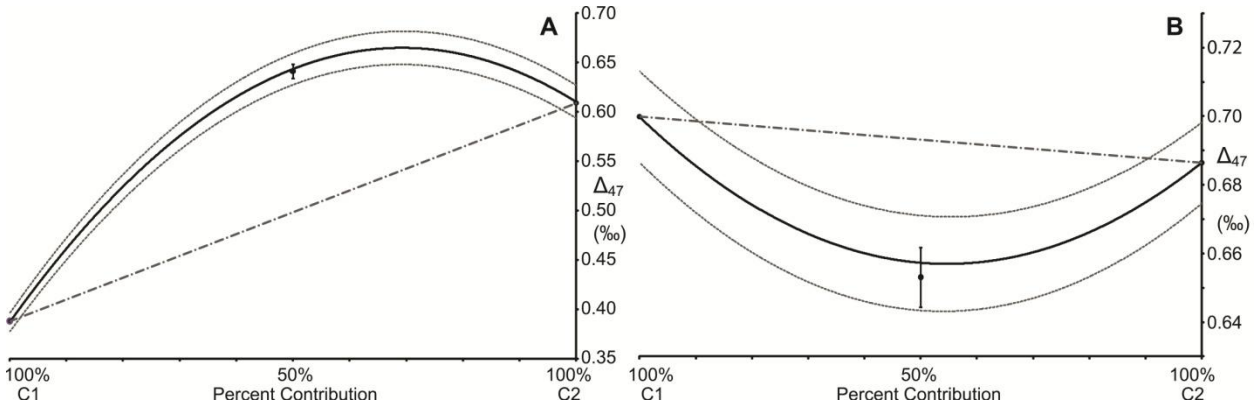

Figure 3.5 Notes: Modeled mixing results versus measured mixtures. Solid black line represents mean model results, with stippled grey lines showing the range of model output based on errors in end member values. Dashed grey line shows the pattern expected from linear mixing of Δ_{47}. Error bars are one standard error. A: Mixture A, representing a positive Γ_{47}. B: Mixture B, representing a negative Γ_{47}.

3.8 Conclusions

Model results on the effects of linear mixing of end members in mass-47 clumped isotope analysis indicate that mixing offsets are usually not significant unless variability in $\delta^{18}O$ and $\delta^{13}C$ exceeds 2‰ for both isotopes or 15‰ for a single isotope. The covariation between $\delta^{18}O$ and $\delta^{13}C$ controls the sign of the Γ_{47} anomaly, as a positive correlation leads to an underestimate of true precipitation temperatures, and a negative correlation leads to an overestimate. End member Δ_{47} values have very little effect on the magnitude of Γ_{47}, suggesting that end member differences in $\delta^{18}O$ and $\delta^{13}C$ are the primary influences on Γ_{47}. To quantify the effects of mixing on Δ_{47} measurements, it is suggested that high resolution $\delta^{18}O$ and $\delta^{13}C$ analysis be performed on samples selected for clumped isotope thermometry. Proxy materials that record seasonal environmental records or integrate large amounts of time in areas sampled for analysis are most likely to be affected by mixing.

Our results suggest that mixing alone is not responsible for many of the offsets between Δ_{47} values and estimated growth temperatures. However, proxies such as shells, corals, speleothems, soil carbonates, and diagenetic phases can all be subject to large variations in $\delta^{18}O$ and $\delta^{13}C$ that can cause measureable Γ_{47} offsets. More research is needed to determine the natural variability within several of these materials. Further development of clumped isotope measurement techniques will likely lead to smaller sample sizes, lowering the risk of mixing multiple components into a single measurement.

3.9 Acknowledgements

WFD would like to thank Cedric John, who inspired this investigation via a conversation at the 2012 AGU Fall Meeting. The authors also thank Alex Lechler and Nathan Niemi for use

of sample 10SP06A. This work was supported by NSF Geobiology and Low Temperature Geochemistry grant EAR 1123733 (KCL).

3.10 References

Adkins J. F., Boyle E. A., Curry W. B., and Lutringer A. (2003) Stable isotopes in deep-sea corals and a new mechanism for "vital effects". *Geochim. Cosmochim. Acta* **67**, 1129-1143.

Affek H. P., and Eiler J. M. (2006) Abundance of mass 47 CO2 in urban air, car exhaust, and human breath. *Geochim. Cosmochim. Acta* **70**, 1-12.

Affek H.P., Bar-Matthews M., Ayalon A., Matthews A., and Eiler J.M. (2008) Glacial/interglacial temperature variations in Soreq cave speleothems as recorded by 'clumped isotope' thermometry. *Geochim. Cosmochim. Acta* **72**, 5351-5360.

Bennett C. E., Marshall J. D., and Stanistreet I. G. (2012) Carbonate horizons, paleosols, and lake flooding cycles: Beds I and II of Olduvai Gorge, Tanzania. *J. Hum. Evol.* **63**, 328-341.

Bergman S.C., Huntington K.W., and Crider J.G. (2013) Tracing paleofluid sources using clumped isotope thermometry of diagenetic cements along the Moab Fault, Utah. *American Journal of Science* **313**, 490-515.

Bristow T., Bonifacie M., Derkowski A., Eiler J., and Grotzinger J. (2011) A hydrothermal origin for isotopically anomalous cap dolostone cements from south China. *Nature* **474**, 68-71.

Budd D. A., Frost E. L., Huntington K. W., and Allwardt P. F. (2013) Syndepositional Deformation Features In High-Relief Carbonate Platforms: Long-Lived Conduits for Diagenetic Fluids. *J. Sediment. Res.* **83**, 12-36.

Came R. E., Eiler J. M., Veizer J., Azmy K., Brand U., and Weidman C. R. (2007) Coupling of surface temperatures and atmospheric CO2 concentrations during the Palaeozoic era. *Nature* **449**, 198-U193.

Choquette P. W., and James N. P. (1990) Limestones – The Burial Diagenetic Environment. In *Diagenesis* (Eds. I. A. McIlreath, and D. W. Morrow). Geological Association of Canada, St. John's, Newfoundland, Canada.

Dennis K. J., Affek H. P., Passey B. H., Schrag D. P., and Eiler J. M. (2011) Defining an absolute reference frame for 'clumped' isotope studies of CO2. *Geochim. Cosmochim. Acta* **75**, 7117-7131.

Dennis K. J., and Schrag D. P. (2010) Clumped isotope thermometry of carbonatites as an indicator of diagenetic alteration. *Geochim. Cosmochim. Acta*, **74**, 4110-4122.

Dettman D. L., Reische A. K., and Lohmann K. C. (1999) Controls on the stable isotope composition of seasonal growth bands in aragonitic fresh-water bivalves (unionidae). *Geochim. Cosmochim. Acta* **63**, 1049-1057.

Deutz P., Montañez I. P., and Monger H. C. (2002) Morphology and Stable and Radiogenic Isotope Composition of Pedogenic Carbonates in Late Quaternary Relict Soils, New Mexico, U.S.A.: An Integrated Record of Pedogenic Overprinting. *J. Sediment. Res.* **72**, 809-822.

Eagle R.A., Schauble E.A., Tripati A.K., Tütken T., Hulbert R.C., and Eiler J.M. (2010) Body temperatures of modern and extinct vertebrates from 13C-18O bond abundances in bioapatite. *Proceedings of the National Academy of Sciences* **107**, 10377-10382.

Eagle, R.A., Eiler, J.M., Tripati, A.K., Ries, J.B., Freitas, P.S., Hiebenthal, C., Wanamaker Jr, A.D., Taviani, M., Elliot, M., Marenssi, S., Nakamura, K., Ramirez, P., and Roy, K., 2013, The influence of temperature and seawater carbonate saturation state on 13C–18O bond ordering in bivalve mollusks: Biogeosciences, v. 10, p. 4591-4606.

Eiler J. M., and Schauble E. (2004) (OCO)-O-18-C-13-O-16 in Earth's atmosphere. *Geochim. Cosmochim. Acta* **68**, 4767-4777.

Ferry J., Passey B., Vasconcelos C., and Eiler J. (2011) Formation of dolomite at 40-80 degree C in the Latemar carbonate buildup, Dolomites, Italy, from clumped isotope thermometry. *Geology* **39**, 571-574.

Ghosh P., Adkins J., Affek H., Balta B., Guo W. F., Schauble E. A., Schrag D., and Eiler J. M. (2006) C-13-O-18 bonds in carbonate minerals: A new kind of paleothermometer. *Geochim. Cosmochim. Acta* **70**, 1439-1456.

Ghosh P., Eiler J., Campana S. E., and Feeney R. F. (2007) Calibration of the carbonate 'clumped isotope' paleothermometer for otoliths. *Geochim. Cosmochim. Acta* **71**, 2736-2744.

Gonfiantini R., Stichler W., and Rozanski K. (1993) Standards and Intercomparison Materials Distributed by the International Atomic Energy Agency for Stable Isotope Measurements. In *Reference and intercomparison materials for stable isotopes of light elements*. International Atomic Energy Agency, Vienna, Austria.

Guo W. F., Mosenfelder J. L., Goddard W. A., and Eiler J. M. (2009) Isotopic fractionations associated with phosphoric acid digestion of carbonate minerals: Insights from first-principles theoretical modeling and clumped isotope measurements. *Geochim. Cosmochim. Acta* **73**, 7203-7225.

Henkes G. A., Passey B. H., Wanamaker A. D., Grossman E. L., Ambrose W. G., and Carroll M. L. (2013) Carbonate clumped isotope compositions of modern marine mollusk and brachiopod shells. *Geochim. Cosmochim. Acta* **106**, 307-325.

Hren M. T., Sheldon N. D., Grimes S. T., Collinson M. E., Hooker J. J., Bugler M., and Lohmann K. C. (2013) Terrestrial cooling in Northern Europe during the Eocene–Oligocene transition. *Proceedings of the National Academy of Sciences* **110**, 7562-7567.

Huntington K. W., Eiler J. M., Affek H. P., Guo W., Bonifacie M., Yeung L. Y., Thiagarajan N., Passey B., Tripati A., Daëron M., and Came R. (2009) Methods and limitations of 'clumped' CO2 isotope (Delta(47)) analysis by gas-source isotope ratio mass spectrometry. *J. Mass Spectrom.* **44**, 1318-1329.

James N. P., and Choquette P. W. Limestones – The Meteoric Diagenetic Environment. In *Diagenesis* (Eds. I. A. McIlreath, and D. W. Morrow). Geological Association of Canada, St. John's, Newfoundland, Canada.

Kaiser J., Rockmann T., and Brenninkmeijer C. A. M. (2003) Assessment of (NNO)-N-15-N-15-O-16 as a tracer of stratospheric processes. *Geophys. Res. Lett.* **30**.

Kluge T., and Affek H.P. (2012) Quantifying kinetic fractionation in Bunker Cave speleothems using Δ47. *Quat. Sci. Revs.* **49**, 82-94.

Passey B.H., Levin N.E., Cerling T.E., Brown F.H., and Eiler J.M. (2010) High-temperature environments of human evolution in East Africa based on bond ordering in paleosol carbonates. *Proceedings of the National Academy of Sciences* **107**, 11245-11249.

Quade J., Garzione C., and Eiler J. (2007) Paleoelevation reconstruction using pedogenic carbonates, Paleoaltimetry: Geochemical and Thermodynamic Approaches, Volume 66: Reviews in Mineralogy & Geochemistry: Chantilly, Mineralogical Soc Amer, p. 53-87.

Quade J., Eiler J., Daëron M., and Achyuthan H. (2013) The clumped isotope geothermometer in soil and paleosol carbonate. *Geochim. Cosmochim. Acta* **105**, 92-107.

Rollion-Bard C., Erez J., and Zilberman T. (2008) Intra-shell oxygen isotope ratios in the benthic foraminifera genus Amphistegina and the influence of seawater carbonate chemistry and temperature on this ratio. *Geochim. Cosmochim. Acta* **72**, 6006-6014.

Schauble E. A., Ghosh P., and Eiler J. M. (2006) Preferential formation of C-13-O-18 bonds in carbonate minerals, estimated using first-principles lattice dynamics. *Geochim. Cosmochim. Acta* **70**, 2510-2529.

Sheldon N. D., and Tabor N. J. (2009) Quantitative paleoenvironmental and paleoclimatic reconstruction using paleosols. *Earth-Sci. Rev.*, **95**, 1-52.

Swart P. K., Burns S. J., and Leder J. J. (1991) Fractionation of the stable isotopes of oxygen and carbon in carbon dioxide during the reaction of calcite with phosphoric acid as a function of temperature and technique. *Chemical Geology; Isotope Geoscience Section* **86**, 89-96.

Thiagarajan N., Adkins J., and Eiler J. (2011) Carbonate clumped isotope thermometry of deep-sea corals and implications for vital effects. *Geochim. Cosmochim. Acta* **75**, 4416-4425.

Tripati A. K., Eagle R. A., Thiagarajan N., Gagnon A. C., Bauch H., Halloran P. R., and Eiler J. M. (2010) C-13-O-18 isotope signatures and 'clumped isotope' thermometry in foraminifera and coccoliths. *Geochim. Cosmochim. Acta* **74**, 5697-5717.

Wang Z. G., Schauble E. A., and Eiler J. M. (2004) Equilibrium thermodynamics of multiply substituted isotopologues of molecular gases. *Geochim. Cosmochim. Acta* **68**, 4779-4797.

Yan H. U. I., Lee X., Zhou H. U. I., Cheng H., Peng Y. A. N., and Zhou Z. (2009) Stable isotope composition of the modern freshwater bivalve *Corbicula fluminea*. *Geochemical Journal* **43**, 379-387.

Yang S., Ding Z., Wang X., Tang Z., and Gu Z. (2012) Negative δ18O–δ13C relationship of pedogenic carbonate from northern China indicates a strong response of C3/C4 biomass to the seasonality of Asian monsoon precipitation. *Palaeogeography, Palaeoclimatology, Palaeoecology* **317–318**, 32-40.

Zaarur S., Olack G., and Affek H. (2011) Paleo-environmental implication of clumped isotopes in land snail shells. *Geochim. Cosmochim. Acta* **75**, 6859-6869.

Zhou J., and Chafetz H. S. (2010) Pedogenic carbonates in Texas: Stable-isotope distributions and their implications for reconstructing region-wide paleoenvironments. *J. Sediment. Res.* **80**, 137-150.

Zyakun A. M. (2003) What factors can limit the precision of isotope ratio measurements in the isotopomer pool? *International Journal of Mass Spectrometry* **229**, 217-224.

Chapter 4

Evaluation of Meteoric Calcite Cements as a Proxy for Mass-47 Clumped Isotope Paleothermometry

4.1 Abstract

Meteoric diagenetic cements are ubiquitous throughout geologic history, affecting most carbonate exposures worldwide. They can often be difficult to interpret, as it is usually difficult to separate the influences of water $\delta^{18}O$ and temperature on isotopic signals contained within the carbonate rock body. Despite this difficulty in interpretation, meteoric phreatic cements can potentially be a useful proxy material, as they form slowly in equilibrium at mean annual temperature and are not affected by any biogenic effects that can bias other proxy materials.

We applied the mass-47 clumped isotope paleothermometer to Pleistocene and Holocene carbonates from Bermuda and Barbados in order to investigate the effects of meteoric diagenesis on Δ_{47} signals, and to determine their suitability as a paleotemperature proxy. Phreatic calcite cements are found to record the same temperatures as unaltered carbonate sediments, while any sample exhibiting vadose characteristics is biased towards unreasonably hot apparent formation temperatures. Burial heating and requilibration are not geologically viable explanations for the anomalously hot temperatures recorded in vadose cements, as neither Bermuda or Barbados has

any burial history. Instead, it is likely that precipitation in the vadose zone occurs on timescales quicker than isotopic equilibrium can be achieved, driven by a combination of CO_2 degassing and evaporation, which have been previously shown to cause problems in speleothems and pedogenic carbonates.

We conclude that meteoric phreatic calcites may be an ideal phase for paleotemperature reconstruction, as they accurately record mean annual temperatures and form under equilibrium conditions, while also being immune to further mineral driven diagenesis. Vadose cements, and any sample likely affected by processes similar to vadose diagenesis, should be avoided for climate reconstructions using the mass-47 clumped isotope thermometer.

4.2 Introduction

The mass-47 clumped isotope carbonate paleothermometer (denoted as Δ_{47}) is a recent innovation that allows independent measurement of the formation temperature of carbonate materials. It has been increasing applied to a variety of problems where independent confirmation of the $\delta^{18}O$ of the precipitating fluid is difficult or unavailable, which precludes accurate reconstructions of paleotemperature and resolution of the depositional environment and history. In contrast, with a single measurement, clumped isotope analysis of carbonates offers the ability to reconstruct the temperature of precipitations, $\delta^{18}O$ and $\delta^{13}C$ of the carbonate, and the $\delta^{18}O$ of formation waters (Ghosh et al. 2006, Eiler 2007, Eiler 2011). A natural application of this technique is the study of meteoric and burial diagenesis, in which the relative influence of temperature and changing $\delta^{18}O$ caused by diagenetic fluids moving through the system are difficult to separate (Bergman et al. 2013, Budd et al. 2013, Loyd et al. 2013). Only with the use of additional constraints such as fluid inclusions, which are not always present or available for

analysis, can carbonate materials be effectively used for reconstructing environmental conditions of earth materials in deep geologic time. Clumped isotopes can potentially resolve these issues, which would greatly advance the study of diagenetic systems, and allow scientists to reconstruct temperatures and water compositions in the absence of other information.

In this study, carbonates forming within the meteoric diagenetic environment are examined to evaluate the degree to which they record and preserve information about the environment in which they formed. Meteoric carbonates are of particular interest because they form at or very near to the Earth's surface, and thus have the potential of providing a unique record of past climate conditions. Meteoric diagenesis takes place primarily in two formation zones: the vadose zone, which occurs above the water table and is a zone of periodic wetting and water transport; and the phreatic zone, which is located below the water table and is constantly saturated with water (James and Choquette, 1990). These two zones have disparate modes of dissolution and cementation. The vadose zone is characterized by water-controlled dissolution, where the saturation state of formation waters moving through the rock body controls carbonate dissolution and precipitation of low-Mg calcite cements (James and Choquette, 1990). Mineral precipitation is driven by CO_2 degassing and surface evaporation. The phreatic zone is characterized by mineral-controlled dissolution and precipitation, where metastable mineralogies such as aragonite and high-Mg calcite are dissolved and replaced by more stable minerals such as low-Mg calcite (James and Choquette, 1990). These differing processes produce distinctive crystal morphologies and characteristics observable in petrographic analyses of the carbonate rock body (Figure 4.1), which allows for determination of the type and degree of diagenetic alteration that has impacted individual samples.

Figure 4.1: Meteoric Diagenesis Zones and Processes

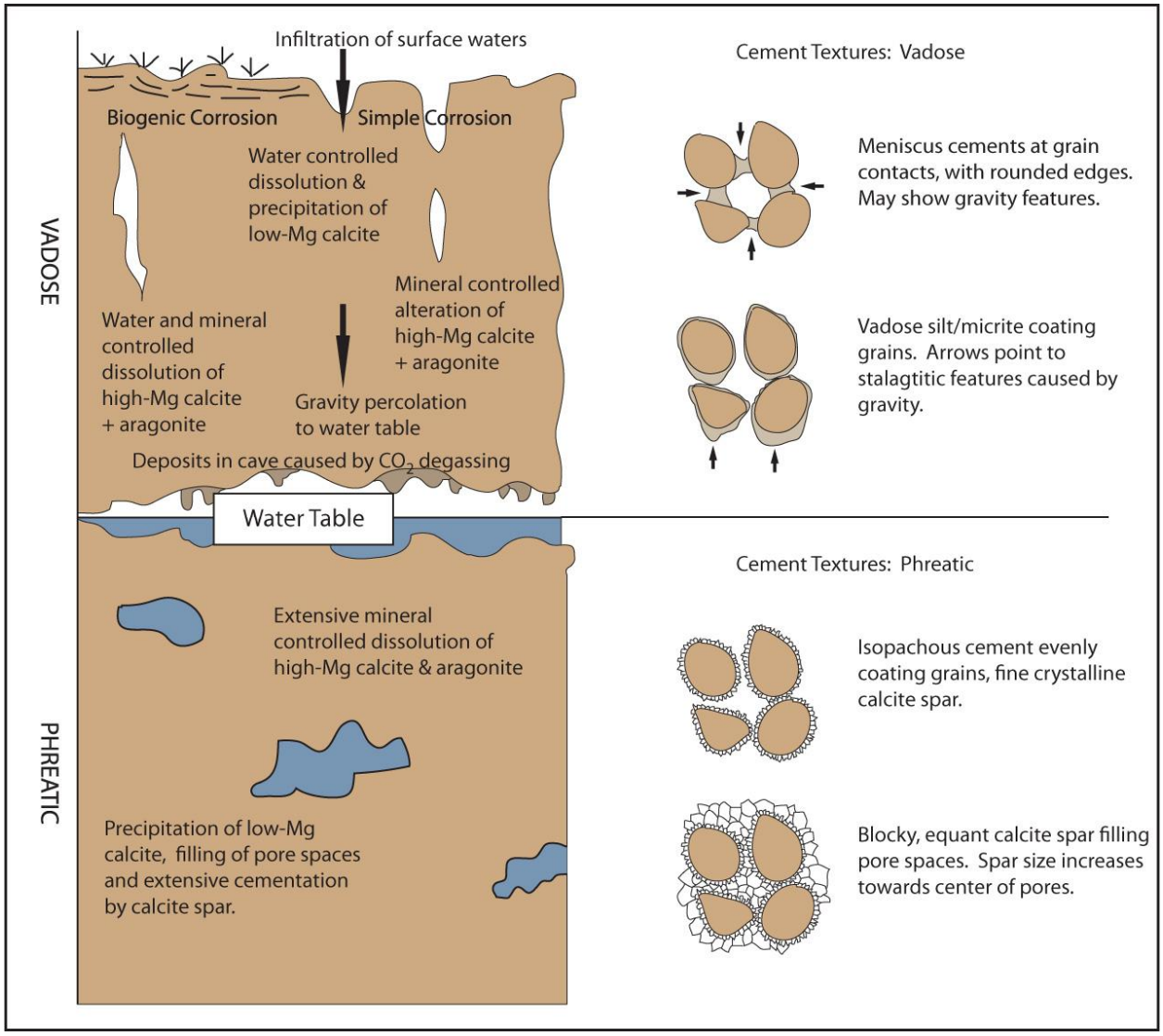

Several characteristics of meteoric phreatic cements (MPC) make them particularly promising as a proxy of mean annual temperature via clumped isotope analysis. These cements form in the water table and are buffered from temperature excursions by the large heat capacity of the host water-saturated rock. MPC precipitates slowly in its environment and is not subjected to excursions in precipitation rate caused by temperature changes, evaporation, or CO_2 degassing, all of which may cause departures from isotopic equilibrium during precipitation. Additionally MPC is formed of stable low-Mg calcite, which is immune to further mineralogical-controlled dissolution-precipitation diagenesis, unlike many primary proxies such as aragonitic bivalves or high-Mg calcite. As such, it may be an ideal phase for reconstructing mean annual temperatures, and clumped isotope analysis of meteoric diagenetic phases may additionally shed light on several of the existing well documented departures from equilibrium documented in Δ_{47} studies of pedogenic carbonates and speleothems, both of which form in environments analogous to the vadose zone. Here we use coexisting unaltered host rock and rocks altered by both phreatic and vadose diagenesis from Pleistocene to Holocene deposits in Bermuda and Barbados to evaluate the effects of meteoric diagenesis on Δ_{47} signals, and to examine their potential as a paleotemperature proxy.

4.3 Geologic Setting

Bermuda and Barbados are two seamounts capped by extensive carbonate forming reefs which comprise most of the exposures above sea level in both island complexes. Both of these locations have extensive well-documented Pleistocene to recent meteoric diagenetic cements occurring in host rocks throughout the islands. These islands also allow us to eliminate burial reheating and the possibility of requilibration of Δ_{47} signals as a variable in our analysis (Passey et al. 2012, Henkes et al. 2014), as neither one has experienced any burial since their formation.

Burial requilibration in response to increased temperature has been suggested as possible mechanism for some of the elevated temperatures reported from prior Δ_{47} studies; our choice of field locations allows us to solely focus on formation temperatures and equilibrium relations without additional complicating factors.

Barbados (15°10' N, 59°30' W) has been continually tectonically uplifted throughout the Pleistocene, producing a series of reef terraces corresponding to successive highstands (Schellmann and Radtke 2004). Sampling on Barbados focused on host rocks of marine isotopic stages (MIS) 9 and 11 in age. The corresponding cements are of an age equal to or younger than the host rocks. All Barbados samples are completely recrystallized, and no original grains are visible. These samples likely reflect 100% phreatic diagenesis (Allan and Matthews, 1982).

Bermuda (32°18' N, 64°45' W) has an unusual geologic history for a carbonate island that has required multiple revisions to the depositional model and ages of the various units (Figure 4.2, see Vacher et al. 1995 and sources within for a full description). Most exposed rocks in Bermuda consist of eolianite, a wind deposited carbonate sandstone made of algal and other carbonate allochems that is intercalculated with paleosols formed during sea level lowstands. Locally, beach deposits are present in some locations. The current depositional model for Bermuda suggests that carbonate primary production reaches a maximum during interglacial highstands, and that large carbonate sand dunes form to create the interior regions of Bermuda (Vacher et al. 1995, Vacher and Rowe 1997). Subsequent diagenesis and calcite cementation lithifies the dunes in place, forming spectacular outcrops of eolianite. The depositional pattern does not produce the 'layer cake' structure that might be expected in subaqueously deposited sediments, but rather a combination of laterally prograding onlapping dune and beach structures that are separated by red soil zones (paleosols) corresponding to

glacial intervals and relative sea level lowstands. Many stratigraphic units are missing from individual outcrops, complicating initial efforts to construct a coherent stratigraphy and to assign depositional ages (Land et al. 1967, Vacher et al. 1995, Vacher and Rowe 1997). This depositional model also implies that all grains contained within a formation predate that formation, which means that the temperature they record does not represent the time of deposition but an amalgamation of time periods preceeding it. Given this, and the fact that current mean annual temperature in Bermuda is the highest it has been since at least MIS 5e (Sachs and Lehman 1999, Lehman et al. 2002), temperatures recorded in host rock in Bermuda are expected to be colder than present.

Diagenetic cements can be used to constrain relative sea level in Bermuda by noting their formation above or below the water table (Meischner et al. 1995). Bermuda has a very simple hydrological system, with all precipitation immediately infiltrating into host rock down to sea level (Rowe 1984). Currently there are no streams or elevated water tables in Bermuda, and it is unlikely that such features were significant in the past. The only way to raise the water table and the associated freshwater lens is to raise the relative sea level, so the existence of phreatic cements at elevations above current sea level has been used by previous authors to constrain minimum sea level rises at times in the past (Meischner et al. 1995, Vollbrecht and Meischner 1996). All of our samples come from sections that are at or above current sea level, so they are not subjected to current phreatic diagenesis which might complicate our temperature reconstructions.

Bermuda samples span host rocks of MIS 13 (or older) to modern beach sands. Host rocks of all interglacial episodes except MIS 3 are present in our sampling. Lowstand sequences

Figure 4.2: Bermuda Stratigraphy and Sampling Locations

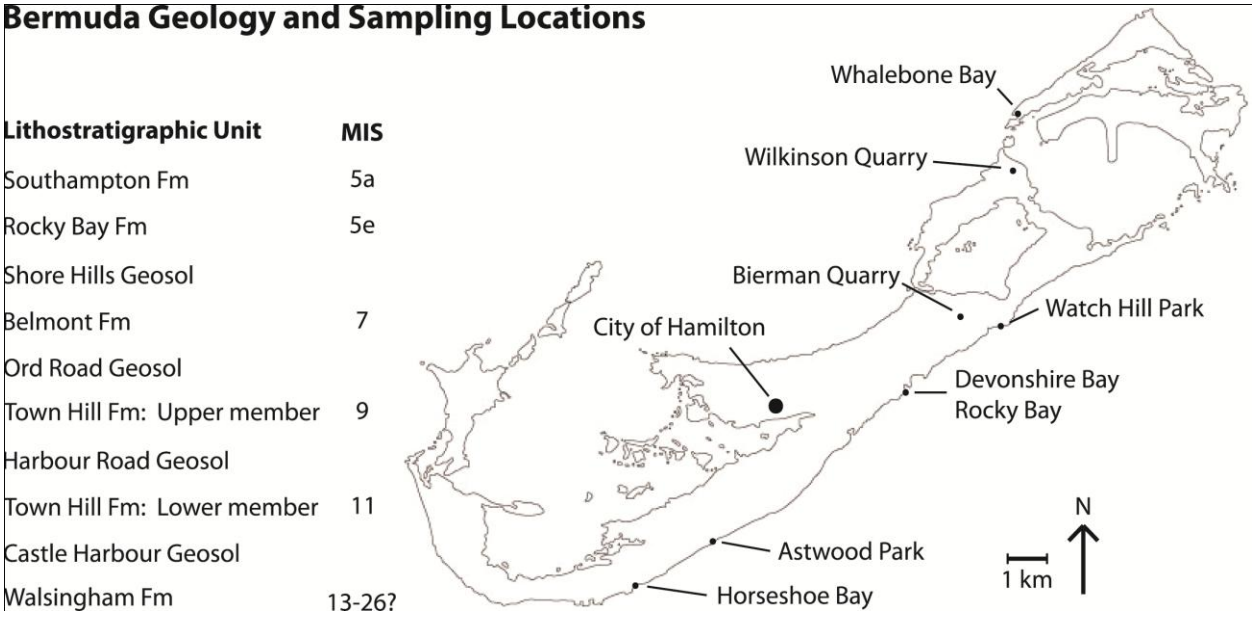

Figure 4.2 Notes: Units present at each sampling location: Astwood Park (Southampton Fm., modern beach), Bierman Quarry (Lower Town Hill Fm., Harbour Road Geosol, Upper Town Hill Fm.), Devonshire Bay/Rocky Bay (Belmont Fm., Shore Hills Geosol (Patchy), Rocky Bay Fm., Southampton Fm.), Horseshoe Bay (Southampton Fm., modern beach), Watch Hill Park (Upper Town Hill Fm., patchy outcrops of Belmont Fm. and Rocky Bay Fm.), Whalebone Bay (Upper Town Hill Fm., Rocky Bay Fm.), Wilkinson Quarry (Walsingham Fm., Castle Harbour Geosol, Lower Town Hill Fm.)

are present below current sea level, and were not sampled. Bermuda samples are not as well cemented as Barbados samples, and all rocks contain a significant amount of original material. Both vadose and phreatic cements are present in Bermuda sequences, with some samples contain only one mode of diagenesis while others contain both phreatic and vadose phases.

4.4 Methods

Samples were collected by use of rock hammer and chisels for all well-cemented rocks. Samples were cleaned with deionized H_2O, the exterior surface removed, and cut into slabs to allow access to unweathered interior surfaces. One surface of the slab was bulk sampled by a 0.5 mm dental bur for Δ_{47} analysis, the other surface was used to make thin sections for petrographic and high resolution stable isotope analysis. Barbados samples were not analyzed by thin section, as they were completely crystalline and showed no traces of original grains.

Modern beach sediments were collected and allowed to air dry in the field before being shipped to the laboratory. Once in the lab, they were rinsed with deionized H_2O, and allowed to air dry. Foreign (non-carbonate) objects were removed with tweezers before powdering with a mortar and pestle for Δ_{47} analysis.

Δ_{47} analysis was performed using a custom built reaction line at the University of Michigan Stable Isotope Laboratory. Four to six mg of sample powder was digested in a common acid bath using 104 wt. % H_3PO_4 at a temperature of 75 °C. Extracted CO_2 was dried by two stages of cryogenic separation at -95 °C (N-propanol/Liquid N_2 mixture, followed by a 5 minute transfer time) to remove H_2O. Dehydrated CO_2 was then further purified of other possible contaminants using a U trap filled with PoraPak Q material (Waters Corp., 50-80 mesh). Samples were frozen into a coldfinger upstream of the PoraPak U trap, and allowed to equilibrate

for 5 minutes with the PoraPak trap held at -30 °C (Defliese et al. in review (this work, Chapter 2)). Liquid N_2 was then placed on a coldfinger downstream of the PoraPak trap, and sample CO_2 was cryogenically drawn through the trap for 15 minutes without the use of a carrier gas. Yields were checked before and after this step using an electric manometer to ensure total sample recovery during the cleaning process, any samples without complete yields were discarded. Purified CO_2 was then transferred to a vial for storage until analysis on the mass spectrometer, and samples were analyzed within 24 hours of extraction.

Samples were analyzed at the University of Michigan Stable Isotope Laboratory using a Thermo-Finnigan MAT 253 dual inlet mass spectrometer that has been specially configured to collect masses 44-49 (Huntington et al. 2009). Analyses were performed in dual inlet mode with the pressure balanced to achieve 16 volts on the mass 44 cup, and measurements for $\delta^{18}O$, $\delta^{13}C$, and Δ_{47} were taken simultaneously. Δ_{47} results are normalized to the Universal Reference Frame by use of CO_2-H_2O equilibration at 25 °C and heated CO_2 at 1000 °C as described in Dennis et al. (2011). All standard CO_2 gases were subject to the same cleaning procedures as sample CO_2 gasses to ensure uniformity. Δ_{47} values were converted into temperatures using the composite calibration of Defliese et al. (in review (this work, Chapter 2)).

Point counting analysis on thin sections was conducted by scanning images from the thin sections using a digital camera attached to a petrographic microscope in the Electron Beam Microanalysis Laboratory at the University of Michigan. An estimate of the relative abundance of the different carbonate allochems and cement types was tabulated from the images using the program *ImageJ*. The percent original grains, vadose cements, phreatic cements, and pore spaces for Bermuda samples were calculated from these image scan data, with areas assigned based on visual characteristics such as cement texture. Thin sections were also examined under

cathodoluminscence, however none of the samples exhibited any fluorescence or luminescent zonation, which is not surprising as there is no weathering source for luminescing ions in Bermuda.

Individual grains and cements were analyzed for $\delta^{18}O$ and $\delta^{13}C$ by microdrilling thin sections by a Merchantek MicroMill computer controlled stage. Approximately 50 μg of powder was used for each analysis, and was analyzed using a Kiel III automated carbonate device attached to a Thermo-Finnegan MAT 253 dual inlet mass spectrometer. Data were standardized by comparison to NBS 18 and 19 standards, and is reported in ‰ relative to the VPDB standard.

Mixing calculations were carried out on Bermuda samples to calculate the influence of different cement types on bulk Δ_{47} values (Defliese and Lohmann, in review (this work, Chapter 3)). Δ_{47} measurements from modern beach sediments as well as samples containing >98% unaltered grains were used to constrain original grain Δ_{47} values, and combined with end-member $\delta^{18}O$ and $\delta^{13}C$ values to estimate phreatic and vadose Δ_{47} values using the approach of Defliese and Lohmann (in review (this work, Chapter 3)). This was achieved by first estimating a common Δ_{47} value for phreatic cements using samples that consisted only of replaced original grains (neomorphic replacement) and phreatic components (>2% vadose component), and then applying the estimated value to samples that had multiple phases present.

4.5 Results

Δ_{47} results and point count data are reported in Tables 4.1 and 4.2. Δ_{47} values are reported as temperatures using the composite calibration of Defliese et al. (in prep (this work, Chapter 2). Barbados samples record temperatures from 15.9 to 21.8 °C, which fall below the current mean annual temperature of 26.2 °C (Table 4.2). Bermuda samples show greater

Table 4.1: Bermuda Point Counting and Stable Isotope Data

SAMPLE	Formation	Fraction Original	Fraction Vadose	Fraction Phreatic	Pore Volume	Bulk $\delta^{13}C$ (VPDB)	Bulk $\delta^{18}O$ (VPDB)	Bulk Δ_{47}	Temp. (° C)
B2011HB1[a]	Modern	N/A	N/A	N/A	N/A	1.55±0.29	-0.30±0.32	0.7164±0.0140	17.5±4.7
B2011AP3[a]	Modern	N/A	N/A	N/A	N/A	0.72±0.21	-0.35±0.18	0.7141±0.0142	18.3±4.8
B2011AP4	Late Southampton	99%	1%	0%	33%	0.22±0.25	-0.68±0.62	0.7213±0.0162	15.9±5.3
B2011AP2[a]	Early Southampton	N/A	N/A	N/A	N/A	0.68±0.13	-0.48±0.24	0.7282±0.0131	13.7±4.2
B2011WB8	Rocky Bay	97%	1%	1%	28%	0.27±0.36	-0.49±0.35	0.7203±0.0144	16.3±4.7
B2011RB9	Belmont	82%	16%	2%	11%	0.68±0.08	-1.03±0.08	0.6952±0.0108	24.8±3.9
B2011DB1	Belmont	43%	13%	43%	8%	-5.84±0.50	-3.31±0.41	0.6755±0.0062	32.1±2.4
B2011DB5	Belmont	22%	2%	77%	17%	-5.11±0.24	-3.17±0.31	0.7298±0.0075	13.2±2.4
B2011DB6	Early Belmont	43%	2%	55%	21%	-5.18±3.78	-3.52±0.94	0.7282±0.0156	13.7±5.0
B2011DB7	Early Belmont	43%	3%	54%	20%	-4.15±0.15	-3.41±0.33	0.6952±0.0165	24.8±6.0
B2011DB8	Early Belmont	43%	2%	55%	14%	-4.49±0.29	-3.38±0.35	0.7091±0.0073	20.0±2.5
B2011DB9	Early Belmont	45%	4%	51%	20%	-4.27±0.38	-3.33±0.24	0.7077±0.0088	20.5±3.0
B2011BQ3	Upper Town Hill	76%	24%	0%	24%	-3.12±0.14	-2.63±0.26	0.6753±0.0139	32.2±5.4
B2011WHP1	Upper Town Hill	54%	43%	3%	11%	-4.77±0.20	-2.36±0.16	0.6396±0.0145	47.0±6.5
B2011WB1	Upper Town Hill	44%	49%	6%	15%	-6.14±0.66	-2.98±0.49	0.6468±0.0047	43.8±2.0
B2011WB2	Upper Town Hill	19%	2%	79%	24%	-5.82±0.89	-3.17±0.57	0.7211±0.0100	16.0±3.3
B2011WB3	Upper Town Hill	33%	1%	65%	9%	-2.89±0.20	-2.48±0.96	0.7154±0.0071	17.9±2.4
B2011BQ1	Lower Town Hill	53%	29%	18%	6%	-6.28±0.26	-3.27±0.32	0.6273±0.0096	52.5±4.5
B2011WQ11	Lower Town Hill	36%	1%	63%	13%	-6.78±0.11	-2.99±0.45	0.7072±0.0033	20.7±1.1
B2011WQ1	Walsingham	50%	13%	37%	22%	-5.18±0.14	-3.58±0.55	0.6244±0.0054	53.9±2.6
B2011WQ12	Walsingham	36%	2%	63%	11%	-5.76±0.20	-3.65±0.50	0.7259±0.0080	14.5±2.6

Table 4.1 Notes: a: Sample was not point counted, as it was either pure sediment or too friable to make thin sections.

Table 4.2: Barbados Stable Isotope Data

Sample	Bulk $\delta^{13}C$ (VPDB)	Bulk $\delta^{18}O$ (VPDB)	Bulk Δ_{47}	Temperature (° C)
WP-19	-7.96±0.04	-4.35±0.08	0.7054±0.0078	21.3±2.7
WP-9-29MAR2010 Replaced Coral	-3.13±0.15	-4.20±0.10	0.7214±0.0107	15.9±3.5
WP-9-29MAR2010 SPAR	-4.50±0.65	-4.35±0.02	0.7177±0.0053	17.1±1.8
St David's Float	-1.17±0.33	-4.23±0.06	0.7040±0.0122	21.8±4.3
WP-07-07	-4.94±0.36	-3.29±0.18	0.7104±0.0120	19.6±4.1
WP-07-29MAR	-5.08±0.37	-3.45±0.07	0.7144±0.0076	18.2±2.5
WP-07-26MAR	-5.72±0.21	-3.54±0.13	0.7153±0.0054	17.9±1.8
Barbados 46	-6.73±0.09	-3.71±0.14	0.7118±0.0097	19.1±3.3
Barbados 9	-5.00±0.47	-3.64±0.13	0.7192±0.0082	16.6±2.7
Barbados 7	-4.21±0.13	-4.21±0.10	0.7117±0.0074	19.1±2.5
WP-21	-9.85±0.54	-4.47±0.34	0.7142±0.0101	18.3±3.4

variation, with a minimum temperature of 13.2 °C and a maximum temperature of 53.9 °C, which significantly exceeds the modern mean annual temperature of 21.6 °C (Table 4.1). When combined with point counting data, a clear trend in temperature is revealed. Samples that consist of either original grains or phreatic cements, or some combination thereof, fall below current mean annual temperature for both islands. In contrast, any sample exhibiting significant vadose cements (>2% vadose component) displays elevated temperatures that in many cases fall well above current mean annual temperatures or even peak summer temperatures (Figure 4.3).

High resolution subsampling results for Bermuda samples are shown in Table 4.3, as well as calculated Δ_{47} values for different cement types. We calculate an average Δ_{47} value of 0.7195‰ for phreatic cements from samples exhibiting only original and phreatic textures, corresponding to an equilibrium temperature of 16.5 °C. Calculated Δ_{47} values for vadose components range from 0.5655‰ to 0.000‰, with an average value of 0.3692‰, which corresponds to an apparent formation temperature of 365 °C. When we only consider samples that have more than 10% vadose component, the average Δ_{47} value rises to 0.4224 ‰, which corresponds to an apparent formation temperature of 234 °C. Calculated mixing offsets in Δ_{47} suggest that end member mixing does not play a significant role in most Bermuda samples, with only a few samples containing significant vadose components having offsets exceeding 0.0010‰, and none larger than 0.0036‰. Our calculations for vadose Δ_{47} values incorporate these offsets for the samples affected.

Figure 4.3: Bermuda Δ_{47} Temperatures Relative to the Stratigraphic Age of Host Rock

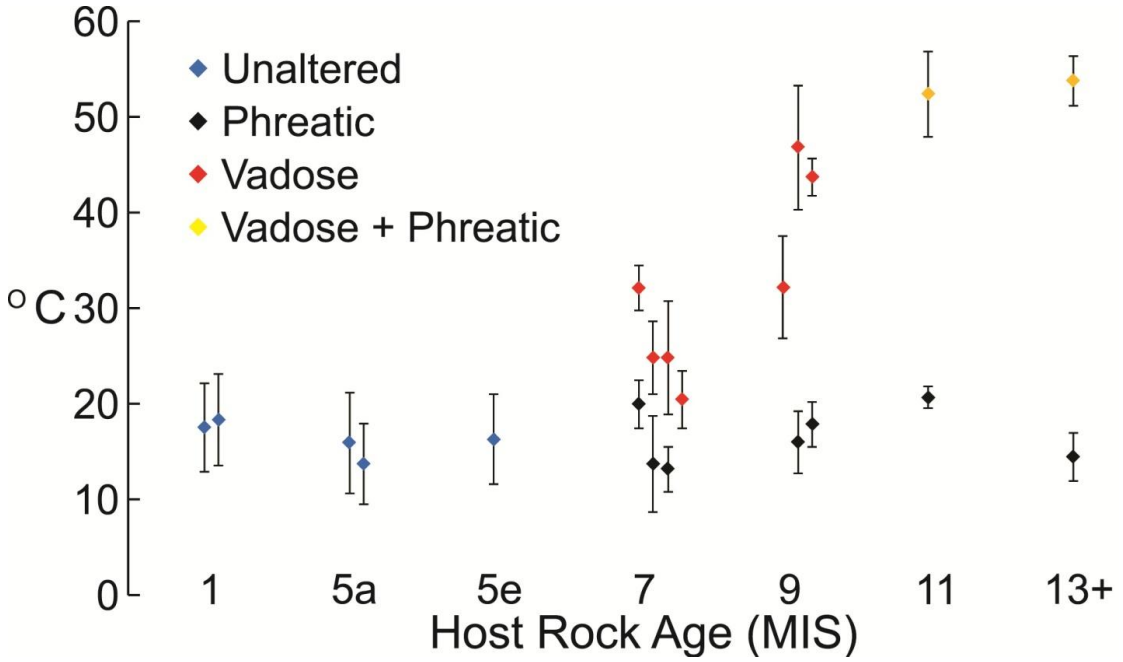

Table 4.3: Bermuda Subsampling and Mixing Calculation Results

SAMPLE	Formation	Original	Phreatic	Vadose	Original $\delta^{18}O$	Original $\delta^{13}C$	Phreatic $\delta^{18}O$	Phreatic $\delta^{13}C$	Vadose $\delta^{18}O$	Vadose $\delta^{13}C$	Δ_{47} (Vadose)
B2011HB1	Modern	100.0%	0.0%	0.0%	N/A						
B2011AP3	Modern	100.0%	0.0%	0.0%	N/A						
B2011AP4	Late Southampton	99.0%	0.0%	1.0%	-1.51	0.51					
B2011AP2	Early Southampton	N/A									
B2011WB8	Rocky Bay	97.0%	1.0%	1.0%	-0.57	-0.28					
B2011RB9	Belmont	82.0%	2.0%	16.0%	-0.78	-0.04			-1.95	-1.73	*0.5655*
B2011DB1	Belmont	43.0%	43.0%	13.0%	-2.27	-6.27	-2.72	-6.12	-6.21	-8.92	*0.3907*
B2011DB5	Belmont	22.0%	77.0%	2.0%	-3.77	-6.04	-3.32	-6.28			
B2011DB6	Early Belmont	42.6%	55.4%	2.0%	-2.80	-4.08	-3.19	-3.23			
B2011DB7	Early Belmont	43.3%	53.8%	2.9%	-2.78	-5.92	-3.39	-4.58	-5.15	-4.84	*0*
B2011DB8	Early Belmont	42.8%	55.1%	2.0%	-3.88	-5.16	-4.85	-5.31			
B2011DB9	Early Belmont	44.6%	51.4%	4.0%	-2.90	-3.99	-3.51	-3.26	*-5.9*	*-20*	*0.3654*
B2011BQ3	Upper Town Hill	75.8%	0.0%	24.2%	-1.78	-2.98			*-5.3*	*-3.5*	*0.5342*
B2011WHP1	Upper Town Hill	53.7%	3.3%	43.0%	-1.75	-3.86	*-22.50*	*-9*	-1.57	-5.60	*0.5244*
B2011WB1	Upper Town Hill	44.2%	6.5%	49.3%	-2.53	-7.04	*-18.00*	*-16*	-1.43	-4.02	*0.5454*
B2011WB2	Upper Town Hill	19.0%	79.4%	1.5%	-2.69	-4.16	-2.57	-6.34			
B2011WB3	Upper Town Hill	33.4%	65.2%	1.4%	-2.13	-4.08	-1.19	-2.52			
B2011BQ1	Lower Town Hill	52.6%	18.3%	29.2%	-2.16	-5.89	-2.54	-5.56	*-5.7*	*-7.4*	*0.3968*
B2011WQ11	Lower Town Hill	36.0%	63.3%	0.8%	-2.33	-7.33	-2.38	-7.57			
B2011WQ1	Walsingham	50.1%	37.4%	12.5%	-3.28	-5.33	-3.37	-6.43	*-5.4*	*-0.8*	*0*
B2011WQ12	Walsingham	35.8%	62.6%	1.6%	-3.34	-5.47	*-3.82*	*-5.92*			

Table 4.3 Notes: Subsampling and mixing calculation results for Bermuda samples. Values in italics were derived from isotope mass balance and the mixing equations of Defliese and Lohmann (in review), and were not measured directly. See text for details.

4.6 Carbonate Petrology and Diagenesis

4.6.1 Barbados

All Barbados samples are fully crystalline and replaced with sparry calcite, and original textures and components have been completely obliterated. In most cases, there are no relicts of original material, though a few samples show neomorphic replacement of coral skeletal structures which have been subsequently overgrown by calcite spar. Remaining porosity for most samples is negligible. Thin sections were not made for these rocks, as the objective of this study is to identify the behavior of Δ_{47} in different types of diagenetic cement, and the Barbados samples comprise meteoric phreatic calcites exclusively.

4.6.2 Bermuda

Bermuda samples were taken at multiple locations on the island (Figure 4.2), focusing on sections and exposures where diagenetic alteration has been reported by previous authors. We will discuss the petrology by field location and Formation.

4.6.2.1 Astwood Park

The Southampton Formation (MIS 5a) forms large eolianite dunes with foresets up to 5 meters in this section, separated by weakly developed protosols rich in land snails. Petrographic analysis of the Southampton Fm. shows that it is very weakly cemented, with ~33% porosity and small quantities (less than 1% of rock) of vadose meniscus cements at grain contacts. Grains do not visually appear to be altered or replaced.

Bulk rock Δ_{47} measurements from the Southampton Fm. at Astwood Bay yield an average of 0.725‰, or 14.8 °C. Simultaneous measurements of bulk rock $\delta^{18}O$ and $\delta^{13}C$ (Figure

4.4A) show that some components of the rock have been altered from primary marine values, as $\delta^{18}O$ averages -0.58‰ VPDB, while $\delta^{13}C$ is 0.45‰ (unaltered values should have $\delta^{18}O > 0$ ‰, $\delta^{13}C \sim 2$ ‰). Subsampling of two red algae grains reveals that some of the grains have been replaced and others retain original isotopic values in equilibrium with seawater. Given the lack of dissolution features and cements precipitated within the pore space of the Southampton Fm. samples, some of the grains that appear altered may be recycled from pre-existing eroded rock allochems that were altered before being incorporated into the Southampton Fm.

In addition to the Southampton Fm. section, a sediment sample was taken from the modern beach at Astwood Park. Bulk measurements of the beach sand give a Δ_{47} value of 0.7141‰, which is equivalent to a formation temperature of 18.3 °C. Bulk $\delta^{18}O$ and $\delta^{13}C$ values are consistent with a mixture of calcite and aragonite in equilibrium with modern seawater.

4.6.2.2 Bierman's Quarry

The Town Hill Fm. at Bierman's Quarry exposes a Lower unit (MIS 11) and Upper unit (MIS 9) separated by a 10-20 cm thick red soil layer. All exposures are well above current sea level and above the influence of all prior sea level maxima. Thin sections of the Lower unit of the Town Hill Fm. show significant amounts of phreatic spar (18% of rock) as well as vadose meniscus cements and thin, irregular crystalline rinds (29%). Porosity (6%) has been reduced by cement growth in inter-granular and dissolution porosity. The Upper Town Hill Fm. is significantly more porous at 24% porosity, and shows no sign of phreatic cementation in thin section. Extensive vadose alteration is present with dissolution apparent on many grains and vadose cements representing 24% of the remaining rock.

Whole rock Δ_{47} values for the Lower and Upper Town Hill Fm. at Bierman's Quarry are 0.627‰ and 0.675‰, which corresponds to 52.5 and 32.2 °C, respectively. Microsampling of algal grains and phreatic cements in the lower unit and algal grains in the upper unit of the Town Hill Fm. shows that they have been altered by fresh water with $\delta^{18}O$ values less than -2‰ based on the combined measures of Δ_{47} and $\delta^{18}O$ (Figure 4.4B).

4.6.2.3 Devonshire Bay/Rocky Bay

The Belmont Formation (MIS 7) in Devonshire and Rocky Bays forms a beach hardground approximately 2 meters above current sea level, which transitions upsection into eolianite dunes. An older set of Belmont Fm. eolianite dunes outcrops below the beachrock and are very heavily altered, with phreatic cement and neomorphic replacement accounting for over 50% of the rock by volume. This is in contrast to the beachrock which is much more varied with 18-79% replacement (Table 4.3). The overlying Belmont Fm. eolianite is very weakly cemented above the 2 meter mark, with negligible phreatic cement and up to 18% vadose cements and silts. In Rocky Bay, the Rocky Bay Formation (MIS 5e) cuts down into the Belmont Fm., consisting of a cliff-cut rubble section, a gastropod rich protosol, which is in turn overlain by the Rocky Bay Fm. eolianite approximately 3 meters above current sea level. The Rocky Bay Formation is significantly less well cemented than the Belmont Fm. beachrock in this locality and is easily friable, unlike the Belmont Formation.

Bulk Δ_{47} values for the older Belmont Fm. eolianite range from 0.695‰ to 0.728‰, which corresponds to 13.7 to 24.8 °C. Two of the samples, which have trace amounts (~4%) of vadose silt features, display elevated temperatures. Microsampling of allochems reveals that all of the grains that appear to be unaltered in thin section have $\delta^{18}O$ values that are not

representative of original material, and have been extensively altered by interaction with fresh water (Figure 4.4C). A few cements have $\delta^{18}O$ values more negative than -5‰, which is more negative than calcite equilibrated with current rainfall (-4‰ VPDB for calclite in equilibrium with rainfall, IAEA/WMO Global Network for Isotopes in Precipitation 2014), so either precipitation patterns have changed or some other process is required to reach such negative values. The overlying Belmont Fm. beach has similar bulk Δ_{47} values as the older eolianite, with Δ_{47} values falling between 0.676‰ and 0.73‰. The two samples that display vadose features (~15% of rock by volume) have lower Δ_{47} values, while the sample containing solely primary marine and phreatic material has higher Δ_{47} values. Microsampling of components shows that the original grains in the beachrock section have not been as uniformly altered with fresh water as in the older eolianite, with some syntaxial cements probably being marine in origin (Figure 4.4D). Some meteoric vadose features in the beachrock were large enough to be microsampled and fall in the range of the other components, with the exception of one vadose cement which had a $\delta^{18}O$ of -8.7‰ and is likely the result of kinetic fractionation.

4.6.2.4 Horseshoe Bay

Modern beach sediment was sampled at Horseshoe Bay. $\delta^{18}O$ and $\delta^{13}C$ values are consistent with calcite and aragonite in equilibrium with modern seawater, and Δ_{47} was 0.716‰, or 17.5 °C.

4.6.2.5 Watch Hill Park

Watch Hill Park is an erosional shoreline, where the host rock is the Upper Town Hill Fm., containing pockets of the Belmont and Rocky Bay Fms. in erosional pits on the exposed surface. The Upper Town Hill Fm. in this location is composed of steeply dipping eolianite

foresets, and was sampled 8 meters above present sea level. Thin section analysis shows that all grains are coated with a 0.02 to 0.03 mm thick fibrous crust of likely former marine cement, which now has been altered in a vadose setting. In a few places small amounts of sparry phreatic cement (3% rock volume, compared to 43% vadose altered cement) can be observed.

Microsampling results from the Upper Town Hill Fm. show that both constituent grains as well as the encrusting fibrous cements have been altered by meteoric water (Figure 4.4E), as they have $\delta^{18}O$ values that are less than -1.5‰, and $\delta^{13}C$ values more negative than expected primary marine values. Bulk rock Δ_{47} was 0.640‰, or 47.0 °C.

4.6.2.6 Whalebone Bay

Whalebone Bay features a beachrock made of the Upper Town Hill (MIS 9) which extends below present sea level, and is overlain by a sequence that reflects the environmental transition from beach, to protosol, and to eolianite dunes of the Rocky Bay Fm. Samples were taken at the northern point of the bay at the well-studied section of Vollbrecht and Meischner (1993). Samples of the Upper Town Hill Fm. were collected from the present intertidal zone, and the Rocky Bay Fm. eolianite was sampled about a meter above the resistant bench formed by the Upper Town Hill Fm. beachrock.

Thin section analysis of the Upper Town Hill Fm. beach shows two stages of encrusting fibrous marine cement coating most grains, each 0.01-0.02 mm thick. Some grains have been neomorphically replaced by calcite spar. Porosity is variable from 9-24%, with pores contining micritic vadose pendants and meniscus cements and local occurrences of phreatic spar. The Upper Town Hill Fm. is very heterogeneous in this location, with point count data showing large variations in the type of cement, neomorphic replacement, and porosity over distances of 0.5

Figure 4.4: Plots of Microsampled $\delta^{18}O$ and $\delta^{13}C$

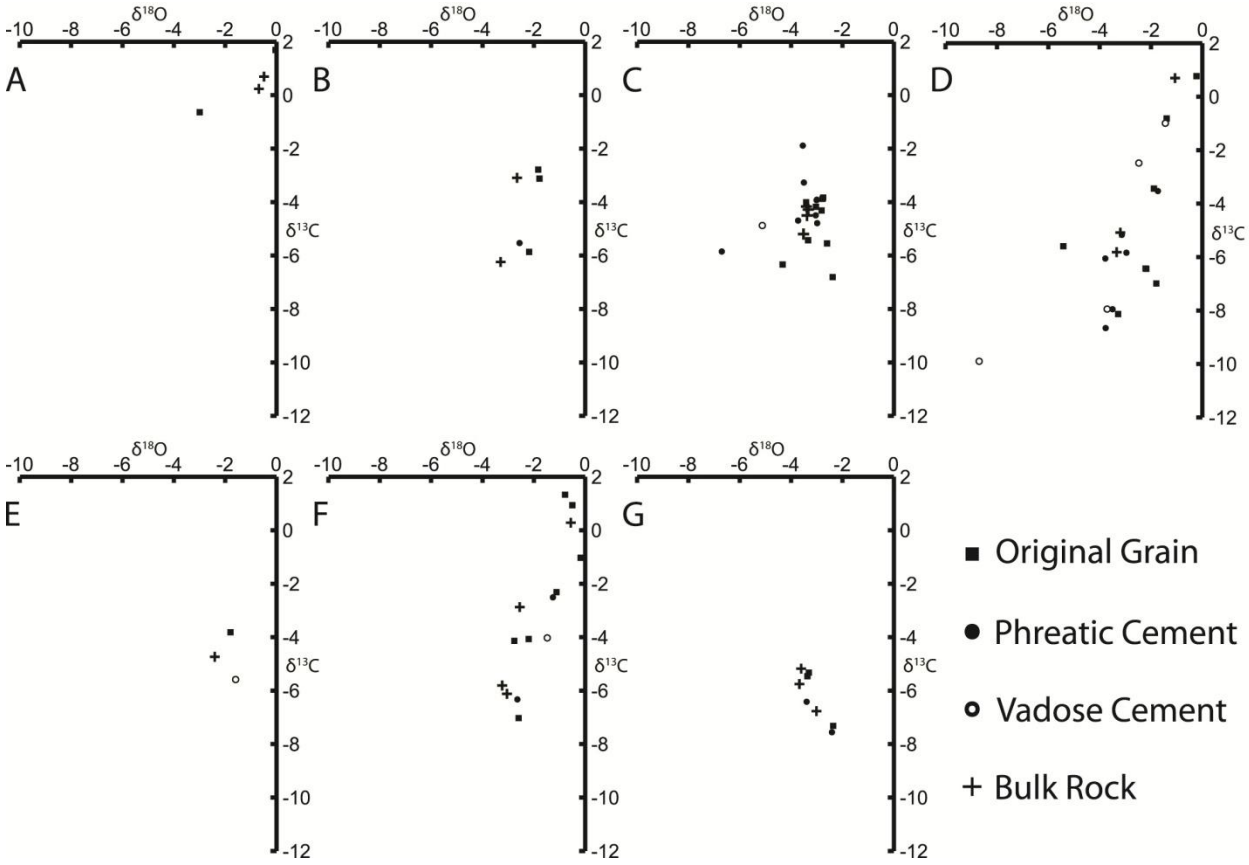

Figure 4.4 Notes: Plots of microsampled $\delta^{18}O$ and $\delta^{13}C$, sorted by sampling locality. A) Astwood Park B) Bierman Quarry C) Devonshire Bay/Rocky Bay older eolianite D) Devonshire Bay/Rocky Bay younger samples E) Watch Hill Park F) Whalebone Bay G) Wilkinson Quarry

meters or less. Isotopic analysis of microsampled components (Figure 4.4F) suggests that the fibrous rims of encrusting cement is marine in origin, while the grains and phreatic spar show evidence of interactions and replacement in meteoric water. Δ_{47} values varied with the contents of the sample – a sample containing 49% vadose features had a Δ_{47} of 0.647‰, while samples consisting of all other material types averaged 0.718‰.

The Rocky Bay Fm. eolianite is much less cemented and altered than the underlying Town Hill Fm, beachrock, with 28% porosity and insignificant amounts of cement or alteration observable in thin section. Microsampling of algae and bivalve fragments within the eolianite show mostly original marine isotopic values, with the possibility of slight interactions with meteoric water after deposition. Bulk Δ_{47} values for the eolianite were 0.720‰, which yield an average temperature estimate of 16.3 °C.

4.6.2.7 Wilkinson Quarry

Wilkinson Quarry is the largest quarry on the island, and features the Walsingham Formation (MIS 13+) and the Lower Town Hill Fm. (MIS 11), which are separated by a red soil zone up to 0.7 meters thick in places. The Walsingham Fm. samples are quite variable in appearance in thin section, with various expression and abundance of vadose features, phreatic spar, dissolution voids, travertine, and neomorphic replacive spar. Generally, samples stratigraphically lower in the quarry show more extensive alteration compared to samples from the upper sections. Samples from the quarry floor contain several layers of fibrous cement, which is interpreted to be originally precipitated in a marine environment. Two samples of the Walsingham Fm. from the quarry floor were analyzed by microdrilling of components for $\delta^{18}O$ and $\delta^{13}C$ and bulk Δ_{47} analysis. Algal grains as well as phreatic cement from the Walsingham

Fm. show extensive alteration by meteoric water, and exhibit a fairly uniform $\delta^{18}O$ composition (Figure 4.4G). The two samples had very different Δ_{47} values, with the sample possessing up to 13% vadose features having a value of 0.624‰, while the sample without significant vadose features had a Δ_{47} value of 0.726‰.

The Upper Town Hill Fm. at Wilkinson Quarry is not as heavily altered as the underlying Walsingham Fm., and possesses a smaller amount of intergranular cement. Cementation is patchy, with vadose meniscus cement in most places, as well as large bladed (dogtooth) spar of meteoric phreatic origin in some pore spaces. Wilkinson Quarry is the only locality where meteoric alteration features were observed more than 8 meters above present sea level. These include spectacular dogtooth spar crystals up to 8 cm in length that were present in cavities near the top of the quarry. Microsampling of samples adjacent to this cavity showed very uniform isotopic values for both phreatic spar and algal grains that indicate alteration by meteoric water (Figure 4.4G). Δ_{47} analysis gave a value of 0.707‰ for this sample, which only had primary marine and phreatic features.

4.7 Discussion

4.7.1 Point Count Analysis and Mixing Calculations

Clumped isotope studies are challenging because of the large amount of material required for accurate, repeatable analysis (~15-20 mg per sample, Huntington et al. 2009, Wacker et al. 2013, Defliese et al. in prep (this work, Chapter 2)). This sample size constraint means that most analyses are composed of bulk samples made up of multiple components, which is certainly the case for our samples. We used point counting and microsampling techniques to quantify the percent contribution of each end member (primary marine, meteoric phreatic, and vadose

components) to each overall bulk sample, such that these measurements can be used to separate the influences of each component from the bulk composition and account for the mixing effects on Δ_{47}. This approach works well for samples that are fairly homogenous, or with samples with multiple phases whose abundance is greater than >5% contribution by volume, but it can be difficult to obtain reasonable results when component contributions are small.

Some of our samples exhibit spatial heterogeneity that makes reconciling bulk results from Δ_{47} measurements with high resolution and point counting analysis difficult. Because we could not sample for Δ_{47} from the thin sections that were used for microsampling and point counting (bulk Δ_{47} sampling took place on the paired chips used for thin sections), there exists the possibility that the high resolution analysis does not accurately reflect the components in the bulk Δ_{47} samples. This is reflected in some of our estimates for $\delta^{18}O$, $\delta^{13}C$, and Δ_{47} for components that were not microsampled due to abundances smaller than the sampling resolution of the MicroMill; some of these estimates are clearly not geologically viable despite being necessary to achieve isotopic mass balance in our calculations. Meteoric vadose Δ_{47} values were calculated using mass balance and the mixing equations outlined in Defliese and Lohmann (in review (this work, Chapter 3)), and were quite variable, however the calculated values for samples containing >10% of the vadose component vary significantly less than the total range expressed by all samples. When discussing the implications of various cement types, we will focus on samples that have larger contributions of that cement type to avoid sampling bias issues.

4.7.2 Diagenetic Alteration of Original Grains

Diagenesis is the alteration and/or replacement of primary carbonate allochems, through a process ranging from microscale dissolution and precipitation to wholesale dissolution and

replacement by secondary cement precipitates. All diagenetic processes (excluding mechanical compaction) involve the interaction of water and results in changes in the petrologic fabric, mineralogic, and geochemical composition of the primary material. In samples of marine origin, this process is enhanced by the presence of marine-derived aragonite and magnesian calcites, that due their thermodynamic metastability, provide an internal mineralogical/geochemical drive that leads to the stabilization of the carbonate assemblage to low-magnesian calcites and/or dolomite process early in its burial history (Stehli and Hower 1961, Land 1967, James and Choquette 1990). The central role of water in this process of stabilization is of importance, as the process of water-rock interaction leads to the progressive modification of the geochemical and isotopic character of samples from the primary marine compositions to phases in equilibrium with the diagenetic fluids (Land and Epstein 1970; Lohmann, 1987; James and Choquette, 1990). Microscale alteration can be impossible to detect using standard petrographic microscopy as primary structures and fabrics can be preserved, and in such cases is only revealed by geochemical or isotopic analysis (James and Choquette 1990). Many of our Bermuda samples fall into this category, as isotopic microsampling on grains that appear to be unaltered shows that some feature geochemical indicators of replacement and rock/water interaction (Figure 4.5). This is most apparent in the older Bermuda samples, as they have had more time to interact with pore fluids and show the largest departure from modern beach sediment.

While many allochems in our samples no longer consist of the primary material, this is accounted for in our mixing calculations and estimated Δ_{47} values for the various components. The mixing calculations use empirically determined values of microsampled $\delta^{18}O$ and $\delta^{13}C$ components: the only assumption is the Δ_{47} value of the altered grains that visually appear to be original. We treated all allochem and diagenetic components separately based on the

Figure 4.5: Bermuda Thin Section Photos

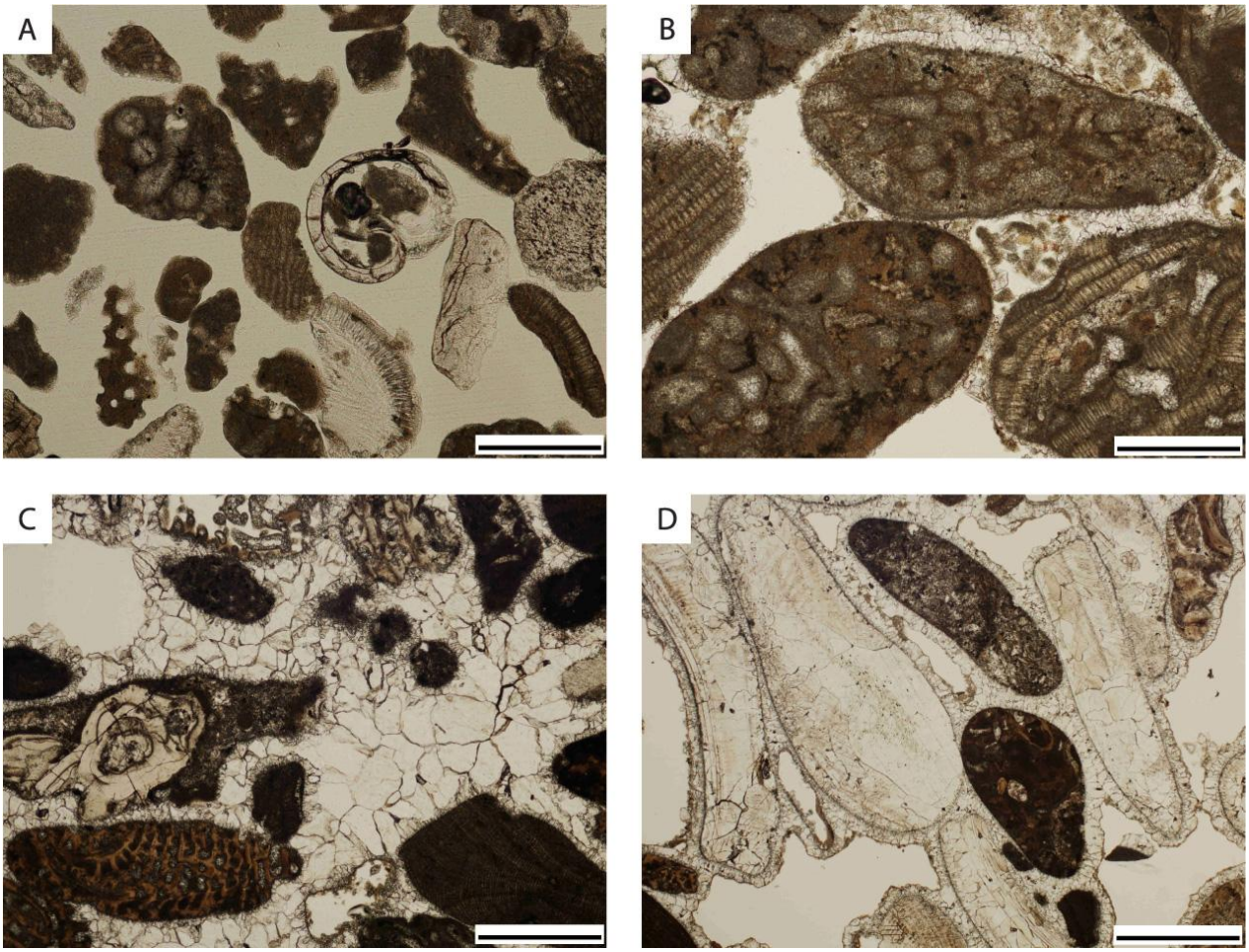

Figure 4.5 Notes: Thin section photos of various Bermuda samples showing varying degrees of diagenetic alteration. A) Sample B2011AP4, which is from the Southampton Fm at Astwood Park. There is very little cementation, and almost all original porosity remains. Scale bar = 0.25 mm. B) Sample B2011RB9, which is from the Belmont Fm in Rocky Bay. Note dissolution within algal grains, as well as vadose zone meniscus cements forming at grain contacts. Scale bar = 0.25 mm. C) Sample B2011DB9, which is from the older Belmont eolianite in Devonshire Bay. Most (but not all) porosity is filled with phreatic calcite spar, with many grains having dissolved out. Isotopic microsampling of algal grains that appeared to be unaltered reveals that they have been altered by meteoric waters. Scale bar = 0.5 mm. D) Sample B2011DB5, which is from the younger Belmont beach section in Devonshire Bay. Most aragonitic grains have been dissolved, with some exhibiting neomorphic replacement which preserves structures (such as the bands in the bivalve fragment). Note the cement evenly coating all grains, which was probably originally marine but is shown to be altered by meteoric waters by isotopic microsampling. Scale bar = 1 mm.

microsampling results. Samples that retain original grain $\delta^{18}O$ and $\delta^{13}C$ values reflecting primary seawater were treated as original and given a Δ_{47} value of 0.7201‰, while samples that have reset 'primary' grain $\delta^{18}O$ and $\delta^{13}C$ values were treated as part of the meteoric phreatic component in our calculations and given a Δ_{47} value of 0.7195‰. This should not significantly affect our results, as the difference between the two values is 0.0006‰, which is practically negligible and well within the average external measurement error of 0.0105‰ for Δ_{47}.

4.7.3 Meteoric Phreatic Cements as Recorders of Mean Annual Temperature

Meteoric phreatic cements develop within below the water table in a fresh water lens in pores that are continuously filled by fluid. On an island as small as Bermuda, the elevation of the water table relative to sealevel is negligible. A first order change in sea level is required to raise water table significantly; and thus, increase the stratigraphic level of carbonate sequence that is effected by meteoric phreatic diagenesis. (Figure 4.6, Meischner et al. 1995, Vollbrecht and Meischner 1996). All of our sample outcrops occur at or above current sea level in Bermuda, requiring that a combination of glacial eustacy and/or tectonic movement to raise the sea level to elevations higher than present. Several beach outcrops in Bermuda are recognized to exist at levels above current sea level despite forming during intervals when ice volume was greater than present (Rowe et al. 2014), so higher relative sea level in Bermuda is not necessarily linked to warmer global temperatures. Δ_{47} values from samples that exhibit significant phreatic cements and alteration and are without significant (<2%) vadose features vary from 0.7072 to 0.7298 ‰, which records a range in temperatures of 13.2 to 20.7 °C. Average temperatures for phreatic samples were 16.5 °C, which is very close to the average temperature of 16.2 °C recorded in unaltered Bermudan rocks and sediments. These temperatures are all below current MAT (Bermuda Weather Service 2014), however reconstructed sea surface temperatures from

Figure 4.6: Water Table Controls in Bermuda

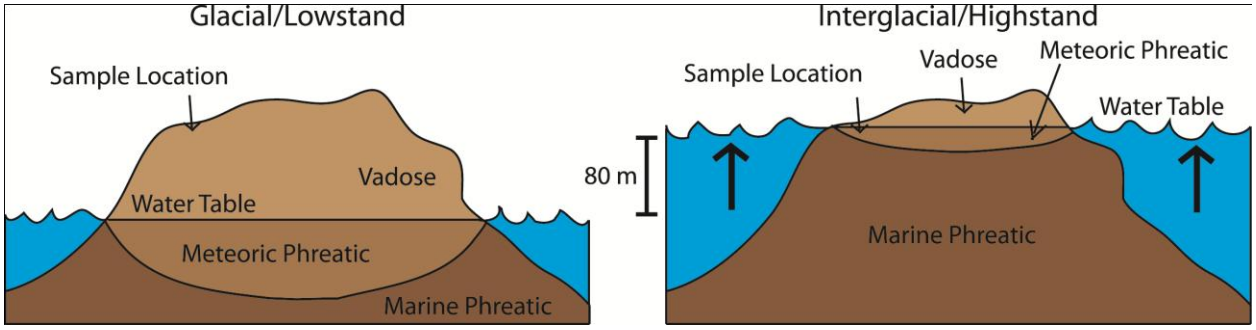

Figure 4.6 Notes: The water table is controlled by relative sea level in Bermuda. During a lowstand, the sample location lies in the vadose zone as there are no perched water tables in Bermuda. During a highstand, raising sea levels raise the water table, so that the sample location lies in the phreatic zone.

ocean cores in the nearby Bermuda Rise suggest that current MAT is the warmest since MIS 5e, and that temperatures in this region were typically ~ 4 degrees colder than present, with some cold periods being up to 6-8 degrees colder (Sachs and Lehman 1999, Lehman et al. 2002). Our samples fit this pattern, as all our samples are on average 5.1 °C colder than present MAT.

Pure phreatic cement samples from Barbados do not fall as close to current MAT as Bermuda samples. All Barbados samples fall below 21.8 °C, and average 18.6 °C, which is 7.6 degrees below the current MAT of 26.2 °C (Barbados Meteorological Services 2014). This may be partially explained by the differences in groundwater conditions between Bermuda and Barbados, as Barbados has a more complicated history of submergence and uplift than Bermuda. Barbados sits near a convergent plate boundary, and has been continually uplifted throughout the Pleistocene, which has produced the stepped coral terraces on the southwest shore (Schellman and Radtke 2004). Barbados also has many current perched aquifers, streams, and natural springs indicative of an elevated water table in many parts of the island, all of which are absent from Bermuda. The constant uplift history and modern evidence for higher water tables in Barbados makes it difficult to constrain the timing of Barbados phreatic diagenesis, as phreatic cements could form during both glacial and interglacial climates. Δ_{47} values from Barbados phreatic calcites suggest that most of them formed at times when the MAT was cooler than present, which would suggest that phreatic diagenesis in Barbados is not confined to interglacial time periods. Oxygen isotope and Mg/Ca evidence suggests that much of the Carribbean was 2-3 °C colder than present during much of the Pleistocene (Emiliani 1966, Schmidt et al. 2006), with temperatures for the last glacial maximum thought to be up to 5 degrees colder than present. Our Δ_{47} values are likely biased towards cooler intervals, as much more time has passed in glacial conditions as opposed to interglacial during the Pleistocene (eg Emiliani 1966), which

means that the volume of cement formed during cooler times is likely to predominate. Mixing of multiple generations of cement into a single measurement also could be contributing to our larger than present Δ_{47} values, as small variations in $\delta^{18}O$ coupled with larger variations in $\delta^{13}C$ typical of freshwater diagenetic systems can easily cause apparent temperature offsets of 2-3 degrees colder than actual precipitation temperatures (Defliese and Lohmann in review). The combination of cooler temperatures during much of the Pleistocene and mixing offsets is the likely cause for such cold temperatures in Barbados.

While Δ_{47} results from Barbados are harder to reconcile with past temperatures, Bermuda Δ_{47} results show that meteoric phreatic cements and original unaltered grains record very similar temperatures. Bermudan phreatic cements record temperatures that are slightly warmer than temperatures from original grains, which is consistent with a diagenetic model where phreatic cements are formed preferentially during highstands. Based on these findings, we believe that phreatic cements in Bermuda are forming in isotopic equilibrium with MAT, and provide a reliable paleothermometry proxy.

4.7.4 Vadose Disequilibrium and Kinetic Fractionation

Based only on bulk Δ_{47} results from Bermuda samples, it is clear that all samples that contain >2% vadose component are biased towards lower Δ_{47} values, and higher apparent precipitation temperatures (Figure 4.7). When point counting and microsampling data are taken into consideration, calculated meteoric vadose component Δ_{47} values are always less than 0.5655 ‰, corresponding to apparent formation temperatures in excess of 85 °C, with some samples exhibiting much higher temperatures. These values cannot represent equilibrium fractionation and precipitation processes in Bermuda, as there is no conceivable scenario in which Bermuda

sediments have been heated to such temperatures. There has been no volcanic activity in the area for 33 Ma (Reynolds and Aumento 1974), and processes such as solar heating from direct sunlight cannot be responsible for such high temperatures (Quade et al. 2013). Likewise, these samples have not been buried more than a few tens of meters at the most, so geothermal heating during burial and re-equilibration (Passey et al. 2012, Henkes et al. 2014) also cannot explain the anomalously low Δ_{47} values.

The remaining explanations for such low Δ_{47} values are kinetic fractionation occurring during the precipitation process, and the preservation of inherited non-equilibrium Δ_{47} values in dissolved inorganic carbon within the vadose cements. The vadose zone is subject to several processes, such as evaporation and CO_2 degassing (James and Choquette 1990, Quade et al. 2013), that may potentially cause kinetic effects, one or more of which is being recorded in the Δ_{47} signal. Infiltrating precipitation carries significant amounts of dissolved CO_2 from soil organic matter down through the vadose zone, where reactions with host carbonate can rapidly occur before isotopic equilibrium is reached. Evaporation and CO_2 degassing to air filled pore spaces causes precipitation to occur in the vadose zone, while also further driving dissolved CO_3^{2-} species away from isotopic equilibrium (eg, Affek 2013). Recent work (Affek 2013) has also shown that rapid precipitation of carbonate minerals can inherit disequilibrium Δ_{47} values from dissolved CO_3^{2-} species; such a process is likely happening in the vadose zone. Given the unique parameters (amount of precipitation, soil cover, etc) that accompany each individual cement forming event (Breecker et al. 2009), a range of Δ_{47} values could occur in the vadose zone despite a common temperature, thus precluding them from yielding meaningful temperature data.

Figure 4.7: Δ_{47} Temperatures Plotted Versus % Vadose Component

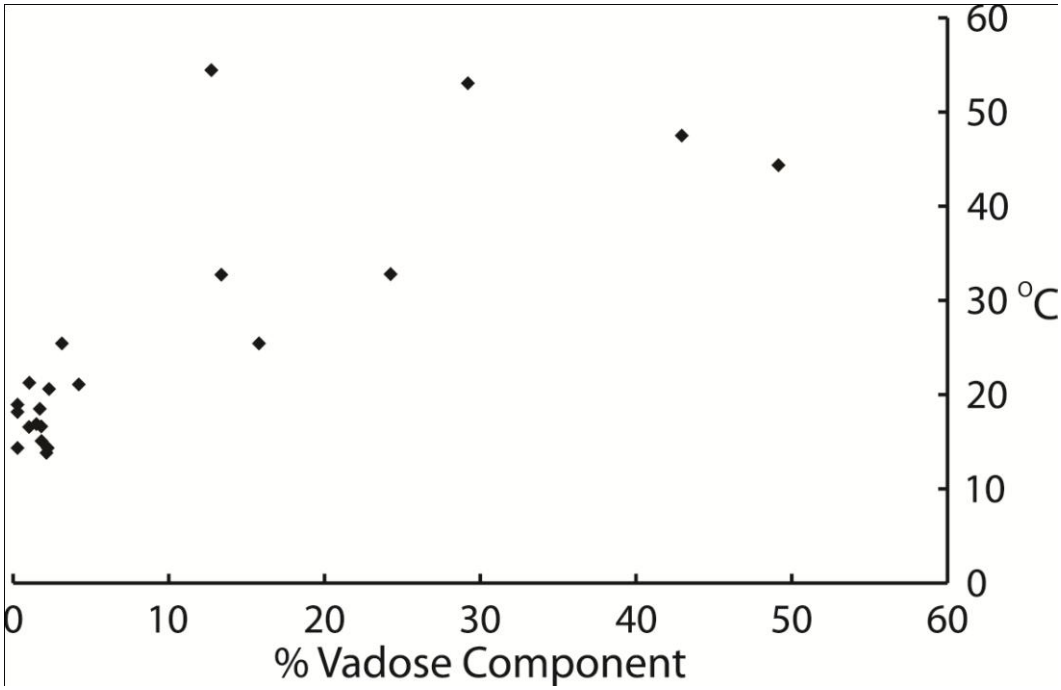

4.7.5 Implications for Paleoclimate Studies

Δ_{47} analysis of meteoric calcite cements reveals that meteoric phreatic cements have great promise as a paleothermometer, while vadose cements are problematic and should be avoided for temperature reconstructions. Samples from Bermuda and Barbados indicate that phreatic cement accurately records inferred mean annual temperatures, without being affected by some of the biases that can affect other proxies. The constant temperature and water saturation of the phreatic zone ensures that precipitation occurs slowly at isotopic equilibrium, without seasonal or other environmental effects that can influence other proxy materials. While we did not investigate other water saturated diagenetic environments, such as deeper burial and marine phreatic environments, they would likely behave in a similar manner as meteoric phreatic cements. The use of Δ_{47} thermometry on other types of phreatic and burial cements would greatly enhance the study of diagenetic systems, and allow better reconstructions of burial history and thermal regime. Meteoric calcite cements also offer the advantage of being relatively resistant to further dissolution and precipitation, as they consist of minerallogically stable low-magnesian calcite which has replaced the complex array of metastable phases comprising the primary marine sediment.

The largest obstacle towards further application of meteoric phreatic cements as a paleoproxy is the matter of dating the exposure. Our Barbados samples illustrate the difficulty in dating the alteration of host rocks, as it is not clear as to when diagenesis may have occurred. Dating of phreatic diagenesis will remain an obstacle for many locations, and may preclude the use of phreatic cements as a proxy for MAT in situations where the timing of diagenesis cannot be constrained.

Disequilibrium Δ_{47} values recorded in vadose cements demonstrates that some proxy materials do not form at isotopic equilibrium, and enhanced precipitation rates are likely the culprit (Daeron et al. 2011, Affek 2013). Cement precipitation within the vadose zone occurs rapidly as $CaCO_3$ solubility is lowered by a higher ionic concentration (evaporation of water), or rising pH (CO_2 degassing) (Daeron et al. 2011), and dissolved inorganic carbon precipitates before isotopic exchange with water reaches isotopic equilibrium. Affek (2013) has shown that the amount of time required to reach isotopic equilibrium with respect to Δ_{47} is controlled by temperature, with reactions at 22 °C taking 12+ hours to reach equilibrium. Given that our Bermudan vadose cements all display values that are clearly out of equilibrium with Δ_{47}, it suggests that cement forming events in the vadose zone occur on very rapid timescales on the order of several hours, and are essentially finished before equilibirum is reached.

Vadose zone disequilibrium raises concerns about other common proxy materials that are used for Δ_{47} analysis that are driven by the same processes governing vadose precipitation. Both speleothems (Affek et al. 2008, Daeron et al. 2011, Kluge and Affek 2012) and pedogenic carbonates (Passey et al. 2010, Suarez et al. 2011, VanDeVelde et al. 2013, Quade et al. 2013) have been extensively studied, with multiple attempts to address the documented offsets between known growth temperature and measured Δ_{47} temperatures (eg Kluge and Affek 2012, Quade et al. 2013). Speleothems, in particular have been shown to inherit non-equilibrium DIC Δ_{47} values caused by CO_2 degassing and rapid precipitation (Daeron et al. 2011, Kluge and Affek 2012), which has limited their application as a proxy for Δ_{47} analysis. Additionally, all pedogenic studies to date that have examined soil nodules have reported unusually warm reconstructed temperatures, which shows the same pattern of bias observed in Bermudan vadose cements. Whether this extends to all pedogenic carbonates is uncertain, but should be fully evaluated in

future studies, given that precipitation in the soil zone occurs rapidly driven by CO_2 degassing and evaporation, the same drivers effecting vadose precipitation.

4.7.6 Implications for Pleistocene Temperatures

Our results suggest that both Barbados and Bermuda were significantly colder than present for most of the Pleistocene. Temperatures on both islands were likely 5 °C colder for much of the Pleistocene, confirming that the current interglacial regime is likely the warmest to have occurred in the last 500,000 years. Colder temperatures occur in unaltered rocks as well as in meteoric phreatic cements from Bermuda, and suggest that Bermudan temperatures were likely colder than present even during warm intervals such as MIS 5e. Fossil evidence supports this conclusion, as coral reefs currently occur in Bermuda, but coral fragments make up very little of the older carbonate rocks and formations. Bermuda is currently near the northern limit of coral reefs today, and it is not difficult to imagine that cooler temperatures in the past would have prevented reef development.

Cooler temperatures from Barbados are more problematic, as traditionally it has been thought that the tropics are not as affected by glacial climates as higher latitudes closer to the poles. Our results suggest that Barbados has been significantly colder than present over much of the Pleistocene, perhaps averaging as much as 5-6 °C colder. Unfortunately our sampling did not include samples that contained unaltered material, so direct comparison with original Δ_{47} values is not possible for Barbados. Some of our results are undoubtedly due to mixing offsets, but they cannot account for more than 2-3 degrees of the 7.6 °C separating our average reconstructed temperature from current MAT (Defliese and Lohmann, in review (this work, Chapter 3)). Based on the tight correlation between original sediment and phreatic Δ_{47} values in

Bermuda, we have no reason to believe that our results are biased, and conclude that Barbados was at least 5-6 °C colder than current MAT for much of the Pleistocene.

4.8 Conclusions

Carbonate rocks from Bermuda and Barbados were analyzed to determine the effects of meteoric diagenesis on clumped isotope signals. A combination of thin section analysis and microsampling for $\delta^{18}O$ and $\delta^{13}C$ was used to characterize different cements and their origin, and show that meteoric phreatic cements likely record mean annual temperatures, while vadose cements are biased towards unrealistically hotter temperatures. Given that phreatic cements form slowly at mean annual temperature, and are insulated from temperature excursions by the host body of rock, they may be an ideal phase for climate reconstructions, particularly in deep geologic time.

Vadose cements are likely biased by kinetic fractionation caused by evaporation and CO_2 degassing mechanisms, which causes precipitation of cements before isotopic equilibrium can be achieved. This raises concerns about other common proxy materials used in Δ_{47} analysis such as speleothems and pedognic carbonates, as the processes which drive precipitation of carbonate are the same as those active in the vadose setting. Therefore, it is recommended that vadose related carbonate phases be avoided in future studies where paleotemperature reconstructions are made.

Our results also show that Bermuda and Barbados were about 5-6 °C colder during much of the Pleistocene. This confirms other work that has suggested that current MAT is higher for the subtropics than any time in the last 500 ka, and suggests that much of the Pleistocene may have been significantly colder in the tropics during glacial intervals than interglacials.

4.9 References

Affek, H. P. (2013), Clumped isotopic equilibrium and the rate of isotope exchange between CO2 and water, *American Journal of Science*, *313*(4), 309-325.

Allan, J. R., and R. K. Matthews (1982), Isotope signatures associated with early meteoric diagenesis, *Sedimentology*, *29*(6), 797-817.

Bergman, S. C., K. W. Huntington, and J. G. Crider (2013), Tracing paleofluid sources using clumped isotope thermometry of diagenetic cements along the Moab Fault, Utah, *American Journal of Science*, *313*(5), 490-515.

Breecker, D. O., Z. D. Sharp, and L. D. McFadden (2009), Seasonal bias in the formation and stable isotopic composition of pedogenic carbonate in modern soils from central New Mexico, USA, *Geological Society of America Bulletin*, *121*(3-4), 630-640.

Budd, D. A., E. L. Frost, K. W. Huntington, and P. F. Allwardt (2013), Syndepositional Deformation Features In High-Relief Carbonate Platforms: Long-Lived Conduits for Diagenetic Fluids, *Journal of Sedimentary Research*, *83*(1), 12-36.

Daëron, M., W. Guo, J. Eiler, D. Genty, D. Blamart, R. Boch, R. Drysdale, R. Maire, K. Wainer, and G. Zanchetta (2011), 13C18O clumping in speleothems: Observations from natural caves and precipitation experiments, *Geochimica et Cosmochimica Acta*, *75*(12), 3303-3317.

Dennis, K. J., H. P. Affek, B. H. Passey, D. P. Schrag, and J. M. Eiler (2011), Defining an absolute reference frame for 'clumped' isotope studies of CO2, *Geochimica et Cosmochimica Acta*, *75*(22), 7117-7131.

Eiler, J. M. (2007), "Clumped-isotope" geochemistry—The study of naturally-occurring, multiply-substituted isotopologues, *Earth and Planetary Science Letters*, *262*(3–4), 309-327.

Eiler, J. M. (2011), Paleoclimate reconstruction using carbonate clumped isotope thermometry, *Quaternary Science Reviews*, *30*(25–26), 3575-3588.

Emiliani, C. (1966), Paleotemperature Analysis of Caribbean Cores P6304-8 and P6304-9 and a Generalized Temperature Curve for the past 425,000 Years, *The Journal of Geology*, *74*(2), 109-124.

Ghosh, P., J. Adkins, H. Affek, B. Balta, W. Guo, E. A. Schauble, D. Schrag, and J. M. Eiler (2006), 13C–18O bonds in carbonate minerals: A new kind of paleothermometer, *Geochimica et Cosmochimica Acta*, *70*(6), 1439-1456.

Henkes, G. A., B. H. Passey, E. L. Grossman, B. J. Shenton, A. Pérez-Huerta, and T. E. Yancey (2014), Temperature limits for preservation of primary calcite clumped isotope paleotemperatures, *Geochimica et Cosmochimica Acta*, *139*(0), 362-382.

Huntington, K. W., et al. (2009), Methods and limitations of 'clumped' CO2 isotope (Δ47) analysis by gas-source isotope ratio mass spectrometry, *Journal of Mass Spectrometry*, *44*(9), 1318-1329.

IAEA/WMO (2014). Global Network of Isotopes in Precipitation. The GNIP Database. Accessible at: http://www.iaea.org/water

James, N. P., and P. W. Choquette (1990), Limestones - The Meteoric Diagenetic Environment, in *Diagenesis*, edited by I. A. McIlreath and D. W. Morrow, pp. 35-74, Geological Association of Canada, St. John's, Newfoundland.

Kluge, T., and H. P. Affek (2012), Quantifying kinetic fractionation in Bunker Cave speleothems using Δ47, *Quaternary Science Reviews*, *49*(0), 82-94.

LAND, L. S., F. T. MACKENZIE, and S. J. GOULD (1967), Pleistocene History of Bermuda, *Geological Society of America Bulletin*, *78*(8), 993-1006.

Land, L. S., and S. Epstein (1970), LATE PLEISTOCENE DIAGENESIS AND DOLOMITIZATION, NORTH JAMAICA1, *Sedimentology*, *14*(3-4), 187-200.

Lehman, S. J., J. P. Sachs, A. M. Crotwell, L. D. Keigwin, and E. A. Boyle (2002), Relation of subtropical Atlantic temperature, high-latitude ice rafting, deep water formation, and European climate 130,000–60,000 years ago, *Quaternary Science Reviews*, *21*(18–19), 1917-1924.

Loyd, S. J., J. A. D. Dickson, P. A. Scholle, and A. K. Tripati (2013), Extensive, uplift-related and non-fault-controlled spar precipitation in the Permian Capitan Formation, *Sedimentary Geology*, *298*, 17-27.

Meischner, D., R. Vollbrecht, and D. Wehmeyer (1995), Pleistocene sea-level yo-yo recorded in stacked beaches, Bermuda south shore, *Geological Society of America Special Papers*, *300*, 295-310.

Passey, B. H., N. E. Levin, T. E. Cerling, F. H. Brown, and J. M. Eiler (2010), High-temperature environments of human evolution in East Africa based on bond ordering in paleosol carbonates, *Proceedings of the National Academy of Sciences*.

Passey, B. H., and G. A. Henkes (2012), Carbonate clumped isotope bond reordering and geospeedometry, *Earth and Planetary Science Letters*, *351–352*(0), 223-236.

Quade, J., J. Eiler, M. Daëron, and H. Achyuthan (2013), The clumped isotope geothermometer in soil and paleosol carbonate, *Geochimica et Cosmochimica Acta*, *105*(0), 92-107.

Reynolds, P. H., and F. Aumento (1974), Deep Drill 1972. Potassium–Argon Dating of the Bermuda Drill Core, *Canadian Journal of Earth Sciences, 11*(9), 1269-1273.

Rowe, M. (1984), The freshwater "Central Lens" of Bermuda, *Journal of Hydrology*, *73*(1–2), 165-176.

Rowe, M. P., K. A. I. Wainer, C. S. Bristow, and A. L. Thomas (2014), Anomalous MIS 7 sea level recorded on Bermuda, *Quaternary Science Reviews*, *90*(0), 47-59.

Sachs, J. P., and S. J. Lehman (1999), Subtropical North Atlantic Temperatures 60,000 to 30,000 Years Ago, *Science*, *286*(5440), 756-759.

Schellmann, G., and U. Radtke (2004), A revised morpho- and chronostratigraphy of the Late and Middle Pleistocene coral reef terraces on Southern Barbados (West Indies), *Earth-Science Reviews*, *64*(3–4), 157-187.

Schmidt, M. W., M. J. Vautravers, and H. J. Spero (2006), Western Caribbean sea surface temperatures during the late Quaternary, *Geochemistry, Geophysics, Geosystems*, *7*(2), Q02P10.

Stehli, F. G., and J. Hower (1961), Mineralogy and early diagenesis of carbonate sediments, *Journal of Sedimentary Research*, *31*(3), 358-371.

Suarez, M. B., B. H. Passey, and A. Kaakinen (2011), Paleosol carbonate multiple isotopologue signature of active East Asian summer monsoons during the late Miocene and Pliocene, *Geology*, *39*(12), 1151-1154.

VanDeVelde, J. H., G. J. Bowen, B. H. Passey, and B. B. Bowen (2013), Climatic and diagenetic signals in the stable isotope geochemistry of dolomitic paleosols spanning the Paleocene–Eocene boundary, *Geochimica et Cosmochimica Acta*, *109*(0), 254-267.

Vacher, H. L., P. J. Hearty, and M. P. Rowe (1995), Stratigraphy of Bermuda: Nomenclature, concepts, and status of multiple systems of classification, *Geological Society of America Special Papers*, *300*, 271-294.

Vacher, H. L., and M. P. Rowe (1997), Chapter 2 Geology and hydrogeology of Bermuda, in *Developments in Sedimentology*, edited by H. L. Vacher and M. Q. Terrence, pp. 35-90, Elsevier.

Vollbrecht, R., and D. Meischner (1993), Sea level and diagenesis: a case study on Pleistocene beaches, Whalebone Bay, Bermuda, *Geol Rundsch*, *82*(2), 248-262.

Vollbrecht, R., and D. Meischner (1996), Diagenesis in coastal carbonates related to Pleistocene sea level, Bermuda Platform, *Journal of Sedimentary Research*, *66*(1), 243-258.

Wacker, U., J. Fiebig, and B. R. Schoene (2013), Clumped isotope analysis of carbonates: comparison of two different acid digestion techniques, *Rapid Communications in Mass Spectrometry*, *27*(14), 1631-1642.

Chapter 5

Warm Southern Ocean Temperatures in the Cenozoic: Eocene to Miocene of New Zealand

5.1 Abstract

The transition from the warm, ice-free conditions of the early Cenozoic to the current glaciated era is one of the largest climatic events of the past 65 million years. Most studies of this transition have utilized the $\delta^{18}O$ of carbonate, which is subject to various factors leading to uncertainty during interpretation. The mass-47 clumped isotope paleothermometer is a new isotopic technique that is independent of many of the unknowns in traditional $\delta^{18}O$ analysis. We measured the Δ_{47} and high resolution $\delta^{18}O$ and $\delta^{13}C$ of *Cucullaea* bivalves from the Canterbury Basin, New Zealand, that span three time slices (41 Ma, 27 Ma, 16 Ma) to constrain temperature and seasonality changes in the shallow shelf across the interval. Results show that the local climate warmed from average temperatures of 12.5 ± 3.3° C in the mid-Eocene to 15.8 ± 1.9 ° C in the mid-Oligocene, and reached average temperatures as high as 17.0 ± 2.2° C in the mid-Miocene climatic optimum. Warming of local ocean water suggests that New Zealand was insulated from Antarctic cooling by a combination of shifting ocean currents and tectonic movement, which likely transported equatorial heat south to New Zealand while at the same time moving New Zealand northward to its present latitude. Reconstructions of seawater $\delta^{18}O$ reveals an increase in global ice volume manifested by a shift to more positive $\delta^{18}O$ seawater values,

despite the warming climate in New Zealand over this interval. Our results contradict the cooling trend that would be interpreted from carbonate $\delta^{18}O$ values alone, and highlight the importance of independent reconstructions of temperature and/or water $\delta^{18}O$.

5.2 Introduction

The onset and evolution of Cenozoic glaciation has been debated over the last half century. Evidence has been accumulating that small continental ice sheets began forming as early as the middle Eocene in Antarctica (Pekar et al. 2005, Ehrmann and Mackenson 1992), while others advocate full bipolar glaciations as early as 42 Ma (Tripati et al. 2005), despite widespread evidence for warm climates at high latitudes (eg, Ivany et al. 2008, Dutton et al. 2002). Other studies have suggested that significant glaciation was delayed until the early Oligocene, when large ice sheets were fully established on Antarctica (Edgar et al. 2007, Zachos et al. 2001, Lear et al. 2000). Global climate cooled from the early Oligocene to the present, and ice volumes fluctuated through the Miocene, with the current bipolar ice dynamic established around 5 Ma (Zachos et al. 2001).

The causes of the global cooling trend from the mid-Eocene through the Miocene are equally controversial. Tectonic events are widely seen as potential drivers of Antarctic cooling, with the Tasman gateway and Drake passage thought to fully open at approximately 31 Ma and 23 Ma, repectively (Case 2007, Exon et al. 2002, Exon et al. 2001, Nelson and Cooke 2001, Kennett 1977). With the opening of these seaways, development of circumpolar currents would lead to diminished poleward heat transport and cooling of Antarctica (Exon et al. 2002, Exon et al. 2001, Kennett 1977). Other studies have pointed to diminished CO_2 levels as the primary cause (Pagani et al. 2011, Berner and Kothvala 2001), with CO_2 possibly being drawn down by

rapid weathering in the Himalayan orogeny (Berner and Kothvala 2001, Ekart et al. 1999, Raymo et al. 1992). CO_2 levels dropped below 400 ppm by the mid-Oligocene, enhancing global cooling, but paleoproxy data in the Eocene and earlier are far more uncertain, and the role of CO_2 is unknown. Regardless of the ultimate cause, it is certain that significant cooling and reduction of CO_2 levels has occurred between the Eocene and present.

Global ice volumes have been reconstructed by studies utilizing benthic and planktonic foraminfera, with the combination of $\delta^{18}O$ and Mg/Ca ratios used to calculate seawater $\delta^{18}O$ (Lear et al. 2000). Global records based on Mg/Ca in benthic foramifera shells (Lear et al. 2000) have shown that up to 1‰ variation in long-term $\delta^{18}O$ is due to ice-volume effects on seawater $\delta^{18}O$. Some reconstructions based on foraminfera have shown large amplitude variability in calculated water $\delta^{18}O$ (>1‰) over relatively short time scales, which have been alternatively interpreted as glacio-eustatic cycles (eg Hurley and Fluegeman 2003) or changes in temperature or salinity (Wade et al. 2001). Difficulty exists in interpreting such results, as much of the sample materials come from cores deposited below the carbonate compensation depth (CCD) where dissolution of primary carbonate can occur, and above the CCD where foraminifera can be readily altered by calcite overgrowths (Boussetta et al., 2011). Interpretation of $\delta^{18}O$ in carbonate alone cannot discriminate the influences of seawater $\delta^{18}O$ versus temperature, and possible secular variation in the Mg/Ca ratios of seawater are difficult to determine. These limitations necessitate the use of other methods to constrain the onset and magnitude of Antarctic glaciation.

We use shallow shelf (~50-100 m depth) bivalves from the Canterbury Basin of the South Island of New Zealand to reconstruct temperature and seawater $\delta^{18}O$ for the southern ocean across three time slices of the Cenozoic (41 Ma, 27 Ma, and 16 Ma). We have used a combined

approach of mass-47 clumped isotope thermometry (Δ_{47}) and high resolution $\delta^{18}O$ measurements on growth bands of *Cucullaea* bivalves to establish mean annual growth temperatures, seawater $\delta^{18}O$, and seasonal temperature variations over an interval of several years per specimen. *Cucullaea* is well suited for this task, as they are a fairly large genus (often 7-8 cm in size) with thick shells (>5 mm) and clearly visible growth banding (Buick and Ivany, 2004). They typically grow in water depths of 50-100 m, are thought to grow primarily in the cooler part of the year, and may live up to 100 years (Buick and Ivany, 2004, Buick thesis). This allows us to determine changes in both overall temperature and seasonality for a region in the Southern Ocean, as well as local seawater $\delta^{18}O$.

5.3 Geologic Setting

The Canterbury basin is a broad depositional basin located on the eastern side of the South Island of New Zealand (Figure 5.1). Rifting associated with the breakup of Gondwana began in the mid-Cretaceous, producing a series of localized terrigenous clastic deposits in the Early Albian (Browne and Field, 1988). Further subsidence in the late Cretaceous continued into the Eocene, producing a broad shallow marine sequence of glauconitic sandstones and carbonates, with proximal facies to the west and distal facies to the east. Regional uplifts and tectonics in the Oligocene created numerous local basins and highs, with the regionally extensive Marshall unconformity separating early Oligocene from mid-late Oligocene sediments across the entire Canterbury basin (Browne and Field 1988, Field and Browne 1986). Beginning in the early Miocene, uplift associated with the Alpine Fault and emergence of New Zealand caused regressive conditions and the eventual emergence of the Canterbury basin in the present. Over 5000 meters of sediment may have been deposited over this time, although the sequence is significantly thinner in the western part of the basin than the east (Browne and Field 1988).

Figure 5.1: Map of Sampling Area

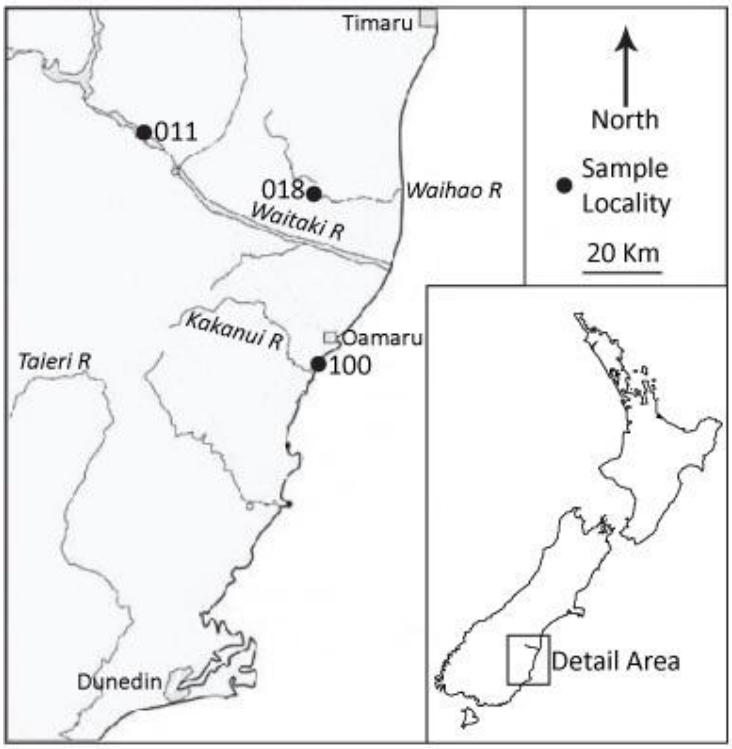

Figure 5.1 Notes: Map of the Canterbury Basin and location within New Zealand. Sampling locations are marked by open circles. 018 = Eocene, 011 = Oligocene, 100 = Miocene.

Marine fossils such as foraminifera, nannoplankton, and molluscs are widespread throughout the sequence, and are interpreted to indicate warm to tropical water assemblages until approximately 15 Ma (Nelson and Cooke, 2001, Maxwell, 1992, Beu and Maxwell, 1990).

Sampling focused on three units within the Canterbury basin; the middle Eocene Waihau Greensand (41 Ma), middle Oligocene Kekenodon Group (27 Ma), and the middle Miocene Mount Harris Fm (16 Ma) (Figure 1 for sampling locations). The Waihau Greensand was sampled on the bank of the South Branch Waihao River in South Canterbury, and consists of a glauconitic sandstone with numerous carbonate concretions. The Kekenodon Group consists of greensand interbedded with thin shelly layers, and was sampled just under the Marshall unconformity along the Lake Waitaki dam. The Mount Harris Formation records the most distal facies, consisting of fossiliferous siltstone with concretions and shelly lenses, and was sampled where it outcrops on the beach south of Awamoa Creek, North Otago. None of these formations are thought to have been buried very deeply, with maximum burial depths of less than 4 km (Fulthorpe et al. 1996, Browne and Field 1988, Field and Browne, 1989), so thermal resetting of Δ_{47} values is unlikely (Passey and Henkes, 2012) (see section 5.6.1 for discussion).

5.4 Methods

We used bivalves of the genus *Cucullaea* from three sites in the Caterbury Basin of New Zealand's South Island, as described in the above section. Each site is represented by three *Cucullaea* specimens. Two *Cucullaea* specimens from each site were chosen for high resolution sampling. Each shell was cross sectioned perpendicular to the sagittal plane, and powdered samples were taken along growth bands using a Merchantek MicroMill automated sampling device. The resulting powder was analyzed for $\delta^{13}C$ and $\delta^{18}O$ in the Stable Isotope Laboratory at

the University of Michigan using a Kiel I automated carbonate device attached to a Thermo-Finnigan MAT 251 dual inlet mass spectrometer.

Each specimen was also bulk sampled for clumped isotope analysis. Samples were prepared using a dental drill, with approximately ~5 mg of powder being used for each analysis. Powdered samples were reacted in 103% phosphoric acid at 75 °C in a common acid bath to release CO_2 gas, which was collected after two stages of cryogenic separation with cold traps held at -90 °C. Sample CO_2 was further purified by passing through a 20 cm U-trap packed with PoraPak Q held at -30 °C. Liquid N_2 was applied to a second U-trap on the downflow side of the PoraPak column, which progressively draws sample CO_2 through the column without the use of a carrier gas. Yields were checked after each step using a manometer to ensure complete transfer and to guard against fractionating the sample during the extraction process. Cleaned sample CO_2 was then transferred to a sealed glass tube for storage until run on the mass spectrometer.

Sample CO_2 was analyzed on a Thermo-Finnigan MAT 253 that has been specially configured to collect masses 44-49 (Huntington et al. 2009). Measurements were simultaneously taken for $\delta^{13}C$, $\delta^{18}O$, and Δ_{47}. The pressure was balanced to achieve 16 V on mass 44 for both sample and standard gasses in dual inlet mode. Each sample replicate was measured for 8 cycles of 10 acquisitions each, for a total of 80 acquisitions per replicate. Integration time was 8 seconds per acquisition with a 16 second changeover time, for a total integration time of 640 seconds per replicate, with a minimum of 3 replicates per sample. Δ_{47} and Δ_{47}-based $\delta^{13}C$ and $\delta^{18}O$ were averaged across all replicates, and errors are reported based on replicate measurments.

A suite of CO_2 gasses of varying isotopic composition equilibrated with water at several temperatures (25, 50, and 1000 °C) were run interspersed with samples to correct for non-

linearity of the source. It has been observed that samples of varying bulk isotopic composition (denoted δ^{47}) but equilibrated at the same temperature exhibit differences in Δ_{47}, which must be corrected for meaningful analysis (Ghosh et al. 2006). These differences are calculated and corrected by use of an Empirical Transfer Function (ETF) (Dennis et. al. 2011), which places all data on the absolute reference frame allowing interlaboratory comparison. The ETF is calculated by plotting the clumped isotope composition of the gasses versus their bulk isotopic composition (δ^{47}), and fitting a least squares regression to the data set, with a common slope (heated gas line) but separate intercepts for each temperature set. This regression was calculated using the R statistical package (www.Rproject.org) and the function 'lm'. The common slope is retained to correct samples for their bulk composition, and the intercepts for each temperature set are then plotted versus their calculated 'true' values from Dennis et al. (2011), with the resulting regression being the ETF. Each unknown sample was first corrected back to a common bulk isotopic composition using the heated gas line, and the resulting Δ_{47} is run through the ETF to give a final Δ_{47} value in the absolute reference frame. For a full description of the calculations, see Dennis et. al. (2011). Finally, Δ_{47} was corrected for acid fractionation using the empirical relationship calculated at the University of Michigan (Defliese et al., in prep (this work, Chapter 2)), and converted into temperatures using the composite calibration of Defliese et al. (in prep (this work, Chapter 2)).

An aliquot of powdered shell material was taken from each specimen to verify mineralogy via x-ray diffraction (XRD). Samples were analyzed using a Scintag X1 Powder Diffractometer housed in the Electron Microbeam Analysis Laboratory at the University of Michigan, and resulting diffraction patterns were compared to the Mindat.org database.

5.5 Results

XRD results indicate that all specimens consist of primary aragonite, with no traces of calcite or other phases indicative of diagenetic alteration. Visual inspection of shell cross sections reveals perfectly preserved growth bands and no evidence of recrystallization.

Δ_{47} values for individual C*ucullaea* specimens range between 0.7043 ± 0.0083‰ and 0.7486 ± 0.0177‰ (Table 5.1), with average values for the Eocene (41 Ma), Oligocene (27 Ma), and Miocene (16 Ma) of 0.7319 ± 0.0105‰, 0.7217 ± 0.0057‰, and 0.7181 ± 0.0066‰. Averages for each time period were calculated by averaging all replicate analyses for that time period, and all errors are reported as one standard error. These values were converted into temperature estimates using the mollusk-based calibration of Henkes et al. (2013). Average growth temperatures for individuals ranged from 21.7 ± 1.6 to 7.4 ± 5.3 °C, with average temperatures of 12.5 ± 3.3, 15.8 ± 1.9, and 17.0 ± 2.2 °C for the Eocene, Oligocene, and Miocene (Table 5.1, Figure 5.2). Bulk $\delta^{13}C$ and $\delta^{18}O$ were measured during clumped isotope analysis (Δ_{47}-derived $\delta^{13}C$ and $\delta^{18}O$). Δ_{47}-derived $\delta^{13}C$ decreases through time, with average values of 2.08 ± 0.14‰ for the Eocene, 1.61 ± 0.26‰ for the Oligocene, and 1.24 ± 0.35‰ for the Miocene. Δ_{47}-derived $\delta^{18}O$ shows the opposite trend and increases through time, with average values of -0.34 ± 0.08‰ for the Eocene, 0.56 ± 0.13‰ for the Oligocene, and 0.62 ± 0.16‰ for the Miocene (Table 5.1).

We constructed estimates of seawater $\delta^{18}O$ ($\delta^{18}O_{SW}$) (Figure 5.2) for each interval using the Δ_{47}-derived temperature estimates and Δ_{47}-derived $\delta^{18}O$ values. These values were used with the aragonite-water calibration of Dettman et al. (1999) to calculate $\delta^{18}O_{SW}$, and errors reflect the one standard error confidence interval in temperature estimates. Confidence intervals reflect errors from both temperature and $\delta^{18}O$ propogated through the Dettman calibration. Seawater $\delta^{18}O$ values range from -3.22 ± 1.22‰ to 0.74 ± 0.33‰ (VSMOW) for individual specimens,

Table 5.1: Stable Isotope Results

Sample	$\delta^{13}C$ High Resolution[a]	$\delta^{18}O$ High Resolution[a]	Δ_{47}-derived $\delta^{13}C$[a]	Δ_{47}-derived $\delta^{18}O$[a]	Δ_{47}[b]	Temperature (°C)[c]	Seawater δ18O[d]
018A	2.76	-0.24	2.04±0.15	-0.44±0.12	0.7486±0.0177	7.4±5.3	-3.22±1.22
018B	N/A	N/A	2.27±0.34	-0.29±0.12	0.7310±0.0226	12.8±7.2	-1.88±1.57
018C	3.15	-0.41	2.00±0.32	-0.24±0.16	0.7118±0.0126	19.1±4.2	-0.48±0.87
Eocene Average	3.01	-0.35	2.11±0.14	-0.33±0.08	0.7319±0.0105	12.5±3.3	-1.97±0.73
011A	2.38	0.67	2.17±0.51	0.44±0.12	0.7351±0.0085	11.5±2.6	-1.41±0.59
011B	2.64	0.72	1.50±0.43	0.75±0.23	0.7246±0.0086	14.9±2.8	-0.38±0.60
011C	N/A	N/A	1.71±0.59	0.45±0.32	0.7043±0.0083	21.7±1.6	0.74±0.33
Oligocene Average	2.54	0.70	1.61±0.26	0.56±0.13	0.7217±0.0057	15.8±1.9	-0.35±0.40
100A	1.98	0.58	1.66±0.39	0.39±0.17	0.7261±0.0117	14.4±3.8	-0.80±0.81
100B	N/A	N/A	1.30±0.79	1.00±0.37	0.7159±0.0085	17.7±2.8	0.48±0.59
100C	2.26	0.63	0.84±0.70	0.44±0.23	0.7244±0.0180	14.9±5.8	-0.67±1.24
Miocene Average	2.16	0.61	1.30±0.35	0.59±0.16	0.7181±0.0066	17.0±2.2	-0.05±0.46

Table 5.1 Notes: Summary data table. 018 = Eocene, 011 = Oligocene, 100 = Miocene. All values are plus/minus one standard error. a: Values reported as ‰ VPDB. b: Values reported as ‰ using the absolute reference frame and procedure of Dennis et al. (2011). c: Calculated using the Δ_{47}-temperature calibration of Defliese et al. (in prep). d: Values reported as ‰ VSMOW, calculated using Δ_{47}-derived $\delta^{18}O$ and Δ_{47}-derived temperature estimates in the aragonite-water thermometry equation of Dettman et al. (1999).

Figure 5.2: Calculated Δ_{47} Temperatures and $\delta^{18}O_{sw}$ Values

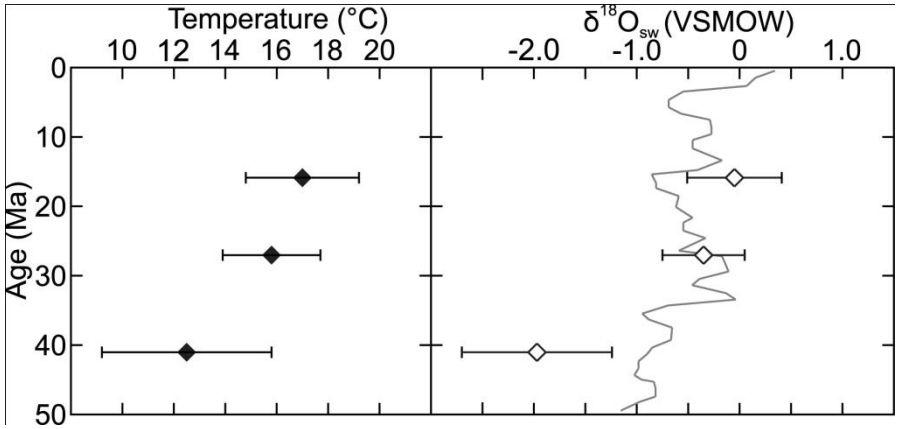

Figure 5.2 Notes: Calculated Δ_{47} temperatures and $\delta^{18}O_{sw}$ values. $\delta^{18}O_{sw}$ values were calculated from measured carbonate $\delta^{18}O$ and Δ_{47} temperatures as described in text. Error bars indicate +/- 1 standard error. Solid grey line is based off the benthic Mg/Ca-$\delta^{18}O$ reconstruction in Lear et al. (2000).

and average values for the Eocene, Oligocene, and Miocene are -1.97 ± 0.73‰, -0.35 ± 0.40‰, and -0.05 ± 0.46‰ (Table 5.1, Figure 5.2).

High resolution $\delta^{13}C$ and $\delta^{18}O$ values are reported for two C*ucullaea* specimens per time interval. Each specimen was sampled over multiple growth bands, and sinusoidality in $\delta^{18}O$ values (Figure 5.3) indicates that sampling covered a period of several years in each clam. Average values for $\delta^{13}C$ and $\delta^{18}O$ were calculated by averaging the entire sampled period, these values are reported without confidence intervals as they represent the average of all measurements and the resulting error would reflect climatic variability over the year, and not sampling error. Values for $\delta^{13}C$ range between a minimum of 1.76‰ and maximum of 3.46‰ for individual measurements, with a total range of 1.98‰ to 3.15‰ for averaged specimens (Figure 5.3). The variability between measurements within a single individual ranged from 0.39‰ to 1.7‰, with the average intra-specimen variability being 0.87‰. Average $\delta^{13}C$ values for the Eocene (Appendix 4), Oligocene (Appendix 5), and Miocene (Appendix 6) were 3.01‰, 2.55‰, and 2.16‰, indicating a trend towards more negative values through time. Averaged $\delta^{13}C$ from high resolution measurements are more positive than Δ_{47}-derived $\delta^{13}C$ for all 6 samples, which may arise due to sample heterogeneity. Gas values for Δ_{47}-derived $\delta^{18}O$ were found to be offset from high resolution $\delta^{18}O$, and were corrected by the use of in-house reference materials (Carrara Marble, Joulter's Key Ooids, and *Adamussium*) to establish an empirical fractionation factor for oxygen isotopes in CO_2 produced by phosphoric acid digestion using our common acid bath reaction line. This fractionation factor differed slightly from published values (Swart et al., 1991, Friedman and O'Neil, 1977), with an α-acid of 1.008051 at 75 °C. Values for high resolution $\delta^{18}O$ range between a minimum of -1.16‰ and a maximum of 1.62‰ for individual measurements, with a total range of -0.41‰ to 0.73‰ for the mean high resolution

Figure 5.3: High Resolution Stable Isotope Data

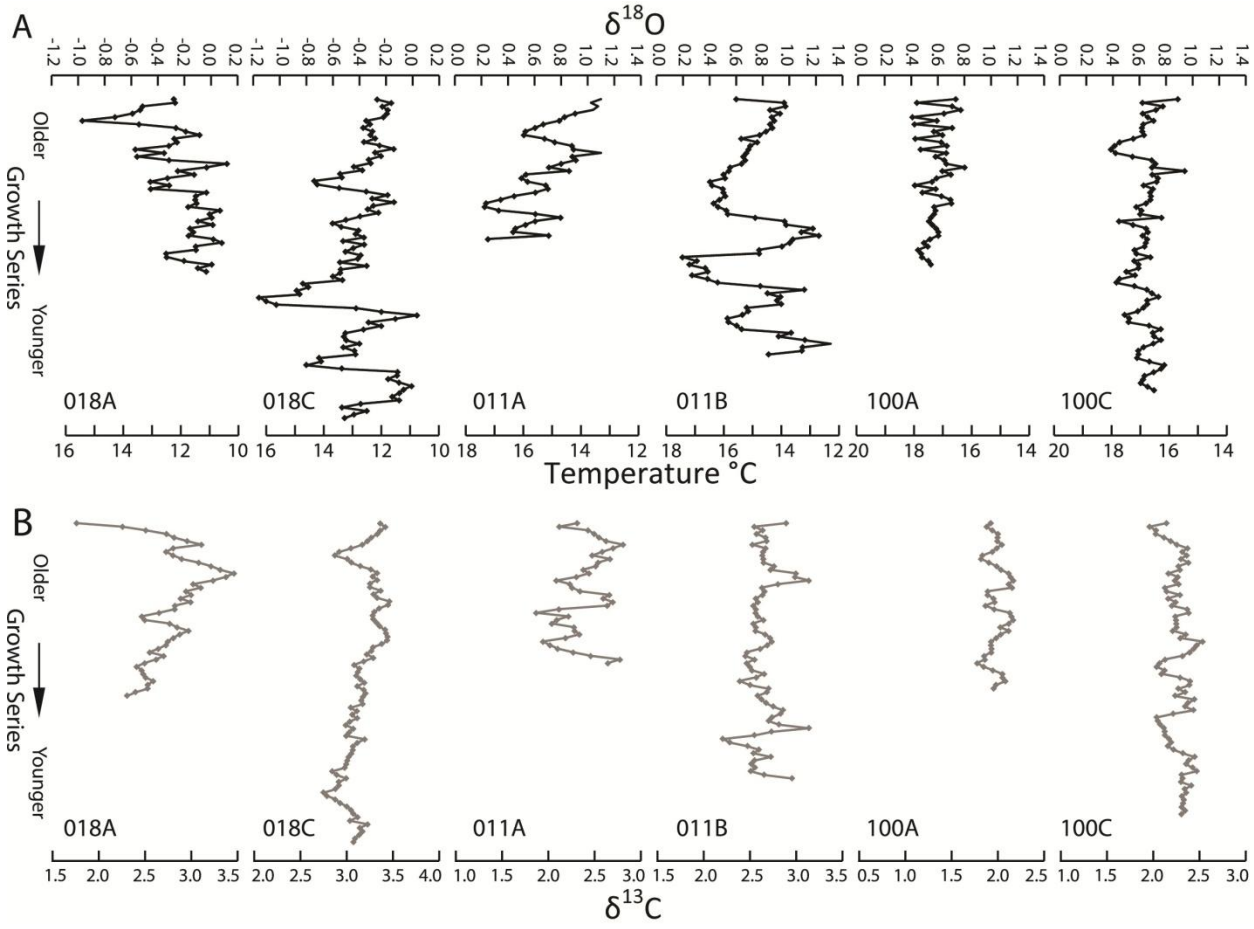

Figure 5.3 Notes: High resolution stable isotope data for each shell. 018 = Eocene, 011 = Miocene, 100 = Miocene. A: $\delta^{18}O$ and temperature data. Temperatures were calculated using Δ_{47} – calculated $\delta^{18}O_{SW}$ and the aragonite – water calibration of Dettman et al. (1999). B: Corresponding $\delta^{13}C$ data.

measurements for individual specimens. The variability in a single individual ranged from 0.39‰ to 1.43‰, with an average intra-specimen variability of 0.93‰. Average $\delta^{18}O$ values were -0.35‰, 0.71‰, and 0.61‰ for the Eocene, Oligocene, and Miocene, respectively.

Seasonal temperature ranges were calculated by using the Δ_{47}-derived seawater $\delta^{18}O$ along with high resolution $\delta^{18}O$ with the thermometry equation of Dettman et al. (1999). Using this method, growth temperatures for the Eocene ranged from 10.4 to 16.3 °C, growth temperatures for the Oligocene ranged from 12.3 to 17.5 °C, and temperatures ranged from 15.4 to 18.1 °C in the Miocene (Figure 5.3). Average temperatures using this method were 12.5 °C for the Eocene, 14.8 °C for the Oligocene, and 17.0 °C for the Miocene, closely matching the Δ_{47}-based temperature reconstruction.

5.6 Discussion

5.6.1 Evaluating Potential Diagenesis and Alteration

In order to provide accurate paleoenvironmental interepretations, the potential for diagenetic alteration must be considered. Clumped isotope paleothermometry is susceptible to two types of diagenesis – recrystallization and bulk exchange of isotopes, and scrambling of ^{13}C-^{18}O bonds within the solid state (Henkes et al. 2014, Passey and Henkes, 2012, Eiler 2011). Both types of diagenesis result in overprinting of the original signals, however we do not believe that either case is likely exhibited in our samples. Meteoric and burial recrystallization will result in changes in both mineralogy and preserved structure, neither of which are observed in our samples. XRD analysis reveals that all specimens consist solely of aragonite with no traces of other mineral phases, as would be expected for samples that have not been altered with various fluids during burial. All of the samples are perfectly preserved under visual inspection, with

clearly defined growth bands showing no signs of reworking. High resolution stable isotope analysis reveals nothing indicative of bulk isotopic exchange, as all values are tightly clustered for both $\delta^{18}O$ and $\delta^{13}C$ while still exhibiting sinusoidality as would be expected from growth patterns (Jones and Quitmyer 1996). $\delta^{13}C$ in all specimens is slightly positive and indicative of an oceanic environment, which would be an unlikely result if they were exchanging with fluids in the meteoric or burial diagenetic environments (Lohmann 1988).

Solid state reordering of ^{13}C-^{18}O bonds is harder to eliminate as a possible source of bias in our reconstruction, as it does not leave physical signs to interpret (Henkes et al. 2014, Passey and Henkes, 2012). Nevertheless, we do not believe that our samples have been buried deeply enough for solid state reordering to be a significant factor. If this type of diagenesis was affecting our samples, we would expect that the Eocene samples would be the most affected as they were buried the deepest and for the longest amount of time (Field and Browne, 1989). However, we do not see that in our Δ_{47} results, as the Eocene samples are the coldest on average, and reconstructed seawater $\delta^{18}O$ values for the Eocene and Oligocene closely match estimates from other proxies, which would not be the case if significant reordering took place. The Miocene samples do show hotter temperatures, and reconstructed seawater values for the Miocene are slightly more positive than compared to other proxies, which is a cause of possible concern. However, it is unlikely that they have experienced significant solid state reordering when the other samples have not, as they were the most shallowly buried and for the shortest amount of time. As such, we do not think that diagenesis has affected our samples, and believe they accurately represent paleoenvironmental conditions.

5.6.2 Sample Distribution

Our sampling interval is very course, with only 9 specimens total from three sites spanning approximately 26 million years. As such, our results cannot reveal much detail about the intricacies of New Zealand climate, but can be used to test the broad hypothesis that New Zealand experienced a cooling climate through the Cenozoic similar to global trends (Zachos et al. 2001). A danger in using only three time periods could be that we capture different Milankovitch cycles, and sampling from one period occurs during an interglacial while a second period captures a glacial episode. The use of multiple shells from each time period lessens this risk, as our compiled estimates of the climate for each time period is based on the aggregate of each set of shells. It is unlikely that all three specimens from a location would be capturing exactly the same period of time and portion on a Milankovitch cycle.

Our results from the Eocene would fit the pattern of capturing different phases of a Milankovitch cycle, as there is a spread from 7.4 °C to 19.1 °C in the Δ_{47}-based temperature results, with relatively constant bulk shell $\delta^{18}O$. It is likely in this case that we have captured a range of climates during a Milankovitch cycle, and that the average of the three shells represents a baseline for Eocene climate. Our records from the Oligocene are similar to the Eocene, with a large variation between the three shells. In contrast, the Miocene results are tightly clustered, and may represent a common depositional mode. It is impossible to rule out the chance that we have captured a relative warm period during the Miocene, but even if this were true, we see no pattern of cooling when comparing the warmest Δ_{47}-based growth temperatures in the Eocene (19.1 ± 4.2 °C, specimen 018C) and Oligocene (21.7 ± 1.6 °C, 011C) to the Miocene reconstruction (17.7 ± 2.8 °C, 100B). As such, this does not change our conclusion that our data shows no evidence of regional cooling during this interval, and may even record a slight warming trend.

5.6.3 Climatic Reconstructions of the Eocene – Miocene New Zealand

Our results indicate that temperatures in the Canterbury Basin remained constant or increased slightly from the Eocene to the Oligocene, and likely increased from the Oligocene to Miocene. Our results are consistent with recent high latitude records based on newer proxies such as TEX_{86} and Mg/Ca ratios (Liu et al. 2009, Bijl et al. 2009, Burgess et al. 2008, etc) that have indicated that sea surface temperatures were higher than previously estimated from foraminifera (eg, Zachos et al. 1994, Shackleton and Kennett 1975), which may be explained by a combination of secondary calcification of foraminifera (eg Lohmann 1995) and uncertainty in the value of seawater $\delta^{18}O$. Because newer proxies such as Δ_{47} and TEX_{86} (eg, Schouten et al. 2009, Liu et al. 2009, Bijl et al. 2009, Burgess et al. 2008) are independent of seawater $\delta^{18}O$, they avoid uncertainties associated with constraining $\delta^{18}O_{sw}$ and can provide more accurate paleoclimatic information, or even be used in conjunction with $\delta^{18}O$ measurements to provide estimates of $\delta^{18}O_{sw}$.

We have combined our paleotemperature estimates based on Δ_{47} with carbonate $\delta^{18}O$ measurements to reconstruct $\delta^{18}O_{sw}$ for each time interval. Our reconstruction indicates an ice free world in the Eocene with $\delta^{18}O_{sw}$ of -1.97‰, moderate glaciation in the Oligocene with $\delta^{18}O_{sw}$ of -0.35‰, and glaciation close to present volumes in the Miocene with $\delta^{18}O_{sw}$ of -0.05‰. These values fall within the range of recent Eocene benthic foramineferal Mg/Ca reconstructions of seawater $\delta^{18}O$ provided by Burgess et al. (2008) from the nearby Hampden Beach site in the Canterbury Basin, and are close to the Mg/Ca curve of Lear et al. (2000) for the Eocene and Oligocene. There is no evidence of a restricted marine system existing in New Zealand at this time, and all paleontological and tectonic evidence indicates an open shelf environment (Fordyce and Maxwell 2003, Sutherland 1999, Maxwell 1992, Beu and Maxwell

1990, Hornibrook 1984), so it is likely that our reconstruction reflects oceanic influences for the Eocene and Oligocene, with the potential of terrestrial meteoric runoff inputs. Carbon isotope data supports full exchange with the open ocean, as a slight trend towards more negative values and reduced global productivity are in line with the global climate cooling (Ivany et al. 2008, Zachos et al. 2001). Our averaged Eocene Δ_{47} temperature reconstruction of 12.5 °C for the shallow shelf is comparable to deeper shelf temperatures (11-13 °C for water at ~300 m depth, Mg/Ca) recorded by benthic formanifera (Liu et al. 2009, Burgess et al. 2008), and our Miocene temperature reconstruction of 17.0 °C is slightly cooler than nearby terrestrial estimates (18-21 °C, CLAMP analysis (Reichgelt et al. 2013)). Taken together, there is no evidence that New Zealand experienced significant cooling during the middle Eocene to middle Miocene interval.

5.6.3.1 Comparison to Traditional ($\delta^{18}O$) Interpretation

Interestingly, our results contradict what would be concluded based on the temporal change observed in carbonate $\delta^{18}O$ alone. Both the high resolution $\delta^{18}O$ and bulk Δ_{47}-derived $\delta^{18}O$ show a large shift towards more positive values from the Eocene to Oligocene, and then similar values from the Oligocene to Miocene. If temperatures were interpreted based exclusively on carbonate $\delta^{18}O$, they would indicate a large decrease in temperature from the Eocene to Oligocene. When combined with global $\delta^{18}O_{sw}$ reconstructions based on benthic Mg/Ca ratios (Lear et al. 2000) the high resolution carbonate $\delta^{18}O$ data indicates that temperatures cooled from the Eocene to Miocene (Figure 5.4). Our estimates of $\delta^{18}O_{sw}$ may not reflect the global oceans, but rather local conditions and processes that may deviate local $\delta^{18}O_{sw}$. The difference between approaches based solely on $\delta^{18}O$ and our reconstruction highlights the importance of constraining $\delta^{18}O_{sw}$ by obtaining independent measurements of paleotemperature, such as Δ_{47}-clumped isotope methods.

Figure 5.4: Comparison of High Resolution Temperature Reconstructions

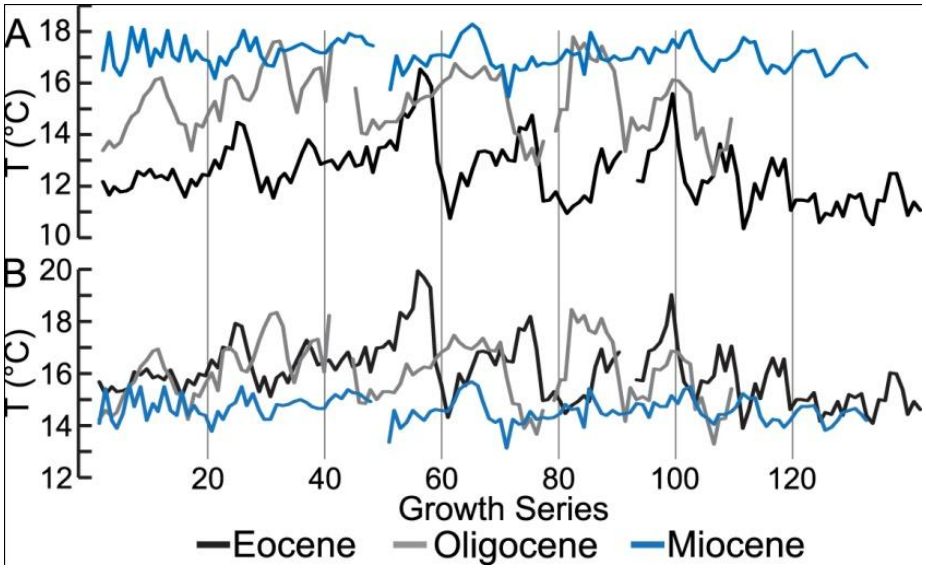

Figure 5.4 Notes: Comparison of high resolution temperature reconstructions using differing estimates of seawater $\delta^{18}O$ with our high resolution carbonate $\delta^{18}O$ data, and the aragonite-H_2O equation of Dettman et al. (1999). Data from multiple shells in each time interval are plotted together and are separated by gaps, this is done for ease of comparison and does not indicate continuity between shells. A: Our Δ_{47} derived seawater $\delta^{18}O$ estimates, with Eocene = -1.56‰, Oligocene = -0.28‰, and Miocene = 0.48‰. B: Mg/Ca derived seawater $\delta^{18}O$ estimates based on Lear et al. (2000) and adjusted to reflect latitude. Eocene = -1.20‰, Oligocene = -0.15‰, and Miocene = -0.55‰.

5.6.3.2 Growth Seasonality

It is necessary to note that our temperature estimates apply only to the times of the year that *Cucullaea* was growing, and may not record the full year's temperature. In particular, *Cucullaea* is thought to grow primarily during the cool season (Buick and Ivany 2004, Buick thesis), and as such our temperature estimates would actually be temperature minima. This could especially impact our seasonality estimates – an alternative scenario to our hypothesis of diminished seasonality could be reduced growth seasons in the year. Under this scenario, the apparent decrease in seasonality seen in the Miocene high resolution temperature reconstruction could be caused by temperatures becoming too hot for *Cucullaea* to grow and precipitate carbonate, with a maximum growth temperature around 18 °C (Figure 5.3). This does not hold if we use global Mg/Ca-derived $\delta^{18}O_{sw}$ estimates, as the reduced Miocene seasonality range is bracketed by the temperature range of the Eocene and Oligocene (Figure 5.4). This also cannot be explained by temperature falling below growth conditions, as *Cucullaea* is commonly found in colder environments during these times, such as the Antarctic peninsula (Ivany et al. 2008, Buick and Ivany 2004, Dutton et al. 2002). Similarly, it is likely that our Eocene and Oligocene high resolution reconstructions cover a broader range of temperatures, as they all fall below the maximum temperatures recorded for the Miocene, and it is unlikely that growth was limited by excessive temperatures.

5.6.4 New Zealand Warming in the Cenozoic

Our reconstruction shows that average temperatures in the shallow shelf (50-100 meters water depth, Buick and Ivany 2004, Maxwell 1992, Beu and Maxwell 1990, etc) warmed from 12.5 °C on average in the Eocene to 15.8 °C and 17.0 °C by 27 and 16 Ma, respectively. This

trend indicates that New Zealand was not influenced (Bijl et al. 2009) by either the circumpolar current or to the 'Antarctic gyre' suggested by Huber et al. (2004), but was continuously bathed in warmer subtropical waters until full operation of the Antarctic circumpolar current at around 15 Ma (Figure 5.5) (Nelson and Cooke, 2001). The high-resolution $\delta^{18}O$ data indicates that seasonality decreased though time, with maximal growth temperature variability of 5.9 °C in the Eocene, compared to 5.2 °C and 2.7 °C in the Oligocene and Miocene. This decrease indicates that the climate in New Zealand was becoming more moderate despite global cooling during this interval, as decreased seasonal extremes and hotter average temperatures are indicative of a more equatorial environment, particularly at 16 Ma. This conclusion is supported by paleogeographic and paleontological reconstructions, which indicate that warm tropical waters flowed south to New Zealand, which created a climate optimum around 16 Ma in the New Zealand area (Nelson and Cooke 2001, Jaques and Robinson 1977), characterized by abundant warm-water fauna (Maxwell 1992, Beu and Maxwell 1990). This climatic optimum ended by the late middle Miocene, caused by the closure of the Indonesian gateway (Kennett et al. 1985) and enhancement of the Antarctic circumpolar current through the unrestricted Tasman gateway, although our record does not extend to this time. Our calculated $\delta^{18}O_{sw}$ values from this site supports the view of global increases in ice volume from 41 to 16 Ma, and indicate an ice free world at 41 Ma, a moderate amount of ice at 27 Ma, and glaciation comparable to modern by 16 Ma; however the global cooling trend is not mimicked by the temperatures recorded in New Zealand and the Canterbury Basin during the intervals we have studied.

A component of New Zealand's apparent warming during this interval is likely due to its tectonic movement north during the Eocene-Miocene time interval. New Zealand drifted north a total of 8° of latitude from 41 Ma to 16 Ma, with the Canterbury Basin moving from ~55 °S to

Figure 5.5: Paleogeographic Reconstruction of New Zealand

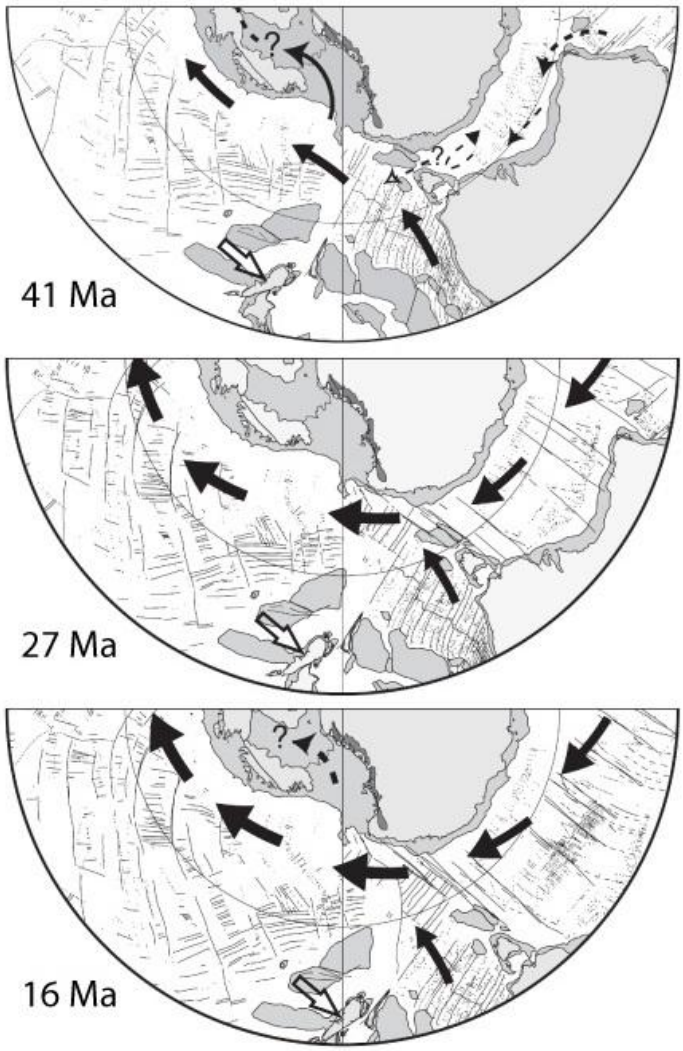

Figure 5.5 Notes: Paleogeographic reconstruction of New Zealand, based on Nelson and Cooke (2001), and Lawver and Gahagan (2003). Solid black arrows indicate supposed paleocurrents, hollow arrow indicates the location of New Zealand and the Canterbury Basin at each time interval.

~47 °S during this time (Figure 5.5) (Lawver and Gahagan 2003, Sutherland 1995). This would have the effect of raising the mean annual temperature, but likely cannot account for all the warming in our record. For comparison, modern mean annual sea surface temperatures across the interval of 55 to 47 °S at 171 °E (near the Canterbury Basin's present location) increase from 6.5 °C to 11.5 °C, and hence differ by ~5 °C (NOAA/NCEP NOMADS). Our reconstruction shows a similar increase of 4.5 °C, however given the widespread evidence of cooling during the interval (Zachos et al. 2001), it is likely that only some of our temperature increase is due to latitudinal positioning, as that would require that the latitudinal difference be greater than 5 °C to offset effects of cooling. This interpretation is consistent with the notion that a large gradient such as in the modern is unlikely to have existed before the formation of full polar ice caps (Herold et al. 2011, Bijl et al. 2009, Zachos et al. 2001, Nelson and Cooke, 2001). Our data likely reflects changes in oceanic heat transport, such as redirection of warm waters towards New Zealand caused by repositioning of ocean currents with an open Indonesian gateway (Herold et al. 2012), and a combination of equatorial movement and global cooling to produce a trend towards warmer climates.

5.7 Conclusion

We have reconstructed temperatures, $\delta^{18}O_{SW}$ and seasonality estimates for the Eocene, Oligocene, and Miocene of New Zealand. Δ_{47} temperature records in *Cucullaea* bivalves show that temperatures increased from 12.5 ± 3.3 °C at 41 Ma to 15.8 ± 1.9°C and 17.0 ± 2.2°C at 27 and 16 Ma, respectively. At the same time, high resolution $\delta^{18}O$ data shows that apparent seasonality changes diminished across the interval, indicating that the climate likely became more tropical from the Eocene to the Miocene at this site, despite global cooling. Our estimates of seawater $\delta^{18}O$ fall within the range predicted by other methods for the Eocene, Oligocene, and

Miocene, and show a trend towards increasing glaciation. Our results also show the importance of independent measures of temperature such as Δ_{47}-paleothermometry, as any interpretation of our data based solely on carbonate $\delta^{18}O$ would identify a cooling trend as opposed to the warming trend revealed in our analysis.

5.8 Acknowledgements

The authors would like to thank the late Phil Maxwell, who generously provided samples from his personal collection. We would also like to thank Lora Wingate at the University of Michigan Stable Isotope Lab, who performed the high resolution isotope measurements.

5.9 References

Berner, R. A., and Z. Kothavala (2001), GEOCARB III: A revised model of atmospheric CO2 over phanerozoic time, *Am. J. Sci.*, *301*(2), 182-204.

Beu, A. G., P. A. Maxwell, and R. C. Brazier (1990), Cenozoic Mollusca of New Zealand, *Paleontological Bulletin*, *58*, 518-518.

Bijl, P. K., S. Schouten, A. Sluijs, G.-J. Reichart, J. C. Zachos, and H. Brinkhuis (2009), Early Palaeogene temperature evolution of the southwest Pacific Ocean, *Nature*, *461*(7265), 776-779.

Boussetta, S., F. Bassinot, A. Sabbatini, N. Caillon, J. Nouet, N. Kallel, H. Rebaubier, G. Klinkhammer, and L. Labeyrie (2011), Diagenetic Mg-rich calcite in Mediterranean sediments: Quantification and impact on foraminiferal Mg/Ca thermometry, *Marine Geology*, *280*(1-4), 195-204.

Browne, G. H., and B. D. Field (1988), A review of Cretaceous-Cenozoic sedimentation and tectonics, east coast, South Island, New Zealand, Canadian Society of Petroleum Geologists, Calgary, AB, Canada (CAN), Canada (CAN), September 1988.

Buick, D. P., and L. C. Ivany (2004), 100 years in the dark: Extreme longevity of Eocene bivalves from Antarctica, *Geology*, *32*(10), 921-924.

Burgess, C. E., P. N. Pearson, C. H. Lear, H. E. G. Morgans, L. Handley, R. D. Pancost, and S. Schouten (2008), Middle Eocene climate cyclicity in the southern Pacific: Implications for global ice volume, *Geology*, *36*(8), 651-654.

Case, J. A. (2007), Opening of the Drake Passage; does this event correlate to climate change and biotic events from the Eocene La Meseta Formation, Seymour Island, Antarctic Peninsula?, U. S. Geological Survey, Reston, VA, United States (USA), United States (USA), 2007.

Defliese, W.F., M.T. Hren, and K.C. Lohmann (in prep), Compositional and temperature effects of phosphoric acid fractionation on Δ47 analysis and implications for discrepant calibrations.

Dennis, K. J., and D. P. Schrag (2010), Clumped isotope thermometry of carbonatites as an indicator of diagenetic alteration, *Geochim. Cosmochim. Acta*, *74*(14), 4110-4122.

Dennis, K. J., H. P. Affek, B. H. Passey, D. P. Schrag, and J. M. Eiler (2011), Defining an absolute reference frame for 'clumped' isotope studies of CO2, *Geochim. Cosmochim. Acta*, *75*(22), 7117-7131.

Dettman, D. L., A. K. Reische, and K. C. Lohmann (1999), Controls on the stable isotope composition of seasonal growth bands in aragonitic fresh-water bivalves (unionidae), *Geochim. Cosmochim. Acta*, *63*(7–8), 1049-1057.

Dutton, A. L., K. C. Lohmann, and W. J. Zinsmeister (2002), Stable isotope and minor element proxies for Eocene climate of Seymour Island, Antarctica, *Paleoceanography*, *17*(2), 6-1-6-13.

Edgar, K. M., P. A. Wilson, P. F. Sexton, and Y. Suganuma (2007), No extreme bipolar glaciation during the main Eocene calcite compensation shift, *Nature*, *448*(7156), 908-911.

Ehrmann, W. U., and A. Mackensen (1992), Sedimentological evidence for the formation of an East Antarctic ice sheet in Eocene/Oligocene time, *Palaeogeography, Palaeoclimatology, Palaeoecology*, *93*(1-2), 85-112.

Ekart, D. D., T. E. Cerling, I. P. Montanez, and N. J. Tabor (1999), A 400 million year carbon isotope record of pedogenic carbonate; implications for paleoatomospheric carbon dioxide, *Am. J. Sci.*, *299*(10), 805-827.

Exon, N. F., et al. (2001), Proceedings of the Ocean Drilling Program, initial reports, the Tasmanian Gateway, Cenozoic climatic and oceanographic development; covering Leg 189 of the cruises of the drilling vessel JOIDES Resolution; Hobart, Tasmania, to Sydney, Australia; sites 1168-1172, 11 March-6 May 2000, *Proceedings of the Ocean Drilling Program, Part A: Initial Reports*, *189*, variously paginated-variously paginated.

Exon, N., et al. (2002), Drilling reveals climatic consequences of Tasmanian Gateway opening, *Eos, Transactions, American Geophysical Union*, *83*(23), 253-259.

Field, B. D., G. H. Browne, and Anonymous (1986), Cretaceous-Cenozoic development of Canterbury and Northeast Otago, Geological Society of New Zealand, Christchurch, New Zealand (NZL), New Zealand (NZL), 1986.

Field, B. D., G. H. Browne, and others (1989), Cretaceous and Cenozoic sedimentary basins and geological evolution of the Canterbury Region, South Island, New Zealand, *New Zealand Geological Survey Basin Studies 2*.

Fordyce, E., P. Maxwell, S. Cox, and B. Smith Lyttle (2003), Canterbury Basin paleontology and stratigraphy; field trip 8, *Geological Society of New Zealand Miscellaneous Publication, 116B*, 1-18.

Friedman, I., J. R. O'Neil, and M. Fleischer (1977), Compilation of stable isotope fractionation factors of geochemical interest [modified], *U. S. Geological Survey Professional Paper*, 12-12.

Fulthorpe, C. S., R. M. Carter, K. G. Miller, and J. Wilson (1996), Marshall Paraconformity: a mid-Oligocene record of inception of the Antarctic circumpolar current and coeval glacio-eustatic lowstand?, *Marine and Petroleum Geology*, *13*(1), 61-77.

Ghosh, P., J. Adkins, H. Affek, B. Balta, W. F. Guo, E. A. Schauble, D. Schrag, and J. M. Eller (2006), C-13-O-18 bonds in carbonate minerals: A new kind of paleothermometer, *Geochim. Cosmochim. Acta*, *70*(6), 1439-1456.

Henkes, G. A., B. H. Passey, E. L. Grossman, B. J. Shenton, A. Pérez-Huerta, and T. E. Yancey (2014), Temperature limits for preservation of primary calcite clumped isotope paleotemperatures, *Geochimica et Cosmochimica Acta*, *139*(0), 362-382.

Herold, N., M. Huber, and R. D. Müller (2011), Modeling the Miocene Climatic Optimum. Part I: Land and Atmosphere*, *Journal of Climate*, *24*(24), 6353-6372.

Herold, N., M. Huber, R. D. Müller, and M. Seton (2012), Modeling the Miocene climatic optimum: Ocean circulation, *Paleoceanography*, *27*(1), PA1209.

Hornibrook, N. d. B. (1984), Guide book for tour BW2 (B13); upper Eocene, Oligocene and lower Miocene biostratigraphy of North Otago and South Canterbury, *N.Z.G.S. Report PAL*, 20-20.

Huber, M., H. Brinkhuis, C. E. Stickley, K. Doos, A. Sluijs, J. Warnaar, S. A. Schellenberg, and G. L. Williams (2004), Eocene circulation of the Southern Ocean; was Antarctica kept warm by subtropical waters?, *Paleoceanography*, *19*(4), 12.

Huntington, K. W., et al. (2009), Methods and limitations of 'clumped' CO2 isotope (Delta(47)) analysis by gas-source isotope ratio mass spectrometry, *J. Mass Spectrom.*, *44*(9), 1318-1329.

Hurley, J. V., and R. H. Fluegeman (2003), *Late middle Eocene glacioeustasy; stable isotopes and Foraminifera from the Gulf Coastal Plain from greenhouse to icehouse; the marine*

Eocene-Oligocene transition, 223-231 pp., Columbia University Press, New York, NY, United States (USA), United States (USA).

Ivany, L. C., K. C. Lohmann, F. Hasiuk, D. B. Blake, A. Glass, R. B. Aronson, and R. M. Moody (2008), Eocene climate record of a high southern latitude continental shelf: Seymour Island, Antarctica, *Geological Society of America Bulletin*, *120*(5-6), 659-678.

Jaques, A. L., and G. P. Robinson (1977), The continent/island-arc collision in northern Papua New Guinea, *BMR Journal of Australian Geology and Geophysics*, *2*(4), 289.

Jones, D. S., and I. R. Quitmyer (1996), Marking Time with Bivalve Shells: Oxygen Isotopes and Season of Annual Increment Formation, *PALAIOS*, *11*(4), 340-346.

Kennett, J. P. (1977), Cenozoic evolution of Antarctic glaciation, the Circum-Antarctic Ocean, and their impact on global paleoceanography, American Geophysical Union, Washington, DC, United States (USA), United States (USA), 1977 Sep 20.

Kennett, J. P., G. Keller, and M. S. Srinivasan (1985), Miocene planktonic foraminiferal biogeography and paleoceanographic development of the Indo-Pacific region, *Memoir - Geological Society of America*, *163*, 197-236.

Lawver, L. A., and L. M. Gahagan (2003), Evolution of Cenozoic seaways in the circum-Antarctic region, *Palaeogeography, Palaeoclimatology, Palaeoecology*, *198*, 11-37.

Lear, C. H., H. Elderfield, and P. A. Wilson (2000), Cenozoic deep-sea temperatures and global ice volumes from Mg/Ca in benthic foraminiferal calcite, *Science*, *287*(5451), 269-272.

Liu, Z., M. Pagani, D. Zinniker, R. DeConto, M. Huber, H. Brinkhuis, S. R. Shah, R. M. Leckie, and A. Pearson (2009), Global cooling during the Eocene-Oligocene climate transition, *Science*, *323*(5918), 1187-1190.

Lohmann, G. P. (1995), A model for variation in the chemistry of planktonic foraminifera due to secondary calcification and selective dissolution, *Paleoceanography*, *10*(3), 445-457.

Maxwell, P. A. (1992), Eocene Mollusca from the vicinity of McCulloch's Bridge, Waihao River, South Canterbury, New Zealand; paleoecology and systematics, *New Zealand Geological Survey Paleontological Bulletin*, 280-280.

Nelson, C. S., and P. J. Cooke (2001), History of oceanic front development in the New Zealand sector of the Southern Ocean during the Cenozoic; a synthesis, *New Zealand Journal of Geology and Geophysics*, *44*(4), 535-553.

NOAA/National Centers for Environmental Prediction (NCEP)/Environmental Modeling Center (EMC)/NOAA Operational Model Archive Distribution System (NOMADS) development group, accessed 8/13/2012.

Pagani, M., M. Huber, Z. Liu, S. M. Bohaty, J. Henderiks, W. Sijp, S. Krishnan, and R. M. DeConto (2011), The role of carbon dioxide during the onset of Antarctic glaciation, *Science*, *334*(6060), 1261-1264.

Passey, B. H., and G. A. Henkes (2012), Carbonate clumped isotope bond reordering and geospeedometry, *Earth Planet. Sci. Lett.*, *351–352*(0), 223-236.

Pekar, S. F., A. Hucks, M. Fuller, and S. Li (2005), Glacioeustatic changes in the early and middle Eocene (51-42 Ma): Shallow- water stratigraphy from ODP Leg 189 Site 1171 (South Tasman Rise) and deep-sea delta super(18)O records, *Bulletin of the Geological Society of America*, *117*(7), 1081-1093.

Raymo, M. E., and W. F. Ruddiman (1992), Tectonic forcing of late Cenozoic climate, *Nature (London), 359*(6391), 117-122.

Reichgelt, T., E. M. Kennedy, D. C. Mildenhall, J. G. Conran, D. R. Greenwood, and D. E. Lee (2013), Quantitative palaeoclimate estimates for Early Miocene southern New Zealand: Evidence from Foulden Maar, *Palaeogeography, Palaeoclimatology, Palaeoecology*, *378*(0), 36-44.

Schouten, S., et al. (2009), An interlaboratory study of TEX86 and BIT analysis using high-performance liquid chromatography–mass spectrometry, *Geochemistry, Geophysics, Geosystems*, *10*(3), Q03012.

Shackleton, N. J., and J. P. Kennett (1975), Paleotemperature history of the Cenozoic and the initiation of Antarctic glaciation; oxygen and carbon isotope analyses in DSDP sites 277, 279, and 281, *Initial Reports of the Deep Sea Drilling Project*, *29*, 743-755.

Sutherland, R. (1995), The Australia-Pacific boundary and Cenozoic plate motions in the southwest Pacific: some constraints from GEOSAT data, *Tectonics, 14*, 819-831.

Sutherland, R. (1999), Basement geology and tectonic development of the greater New Zealand region; an interpretation from regional magnetic data, *Tectonophysics*, *308*(3), 341-362.

Swart, P. K., S. J. Burns, and J. J. Leder (1991), Fractionation of the stable isotopes of oxygen and carbon in carbon dioxide during the reaction of calcite with phosphoric acid as a function of temperature and technique, *Chemical Geology; Isotope Geoscience Section*, *86*(2), 89-96.

Tripati, A., J. Backman, H. Elderfield, and P. Ferretti (2005), Eocene bipolar glaciation associated with global carbon cycle changes, *Nature*, *436*(7049), 341-346.

Wade, B. S., D. Kroon, and R. D. Norris (2001), Orbitally forced climate change in late mid-Eocene time at Blake Nose (Leg 171B); evidence from stable isotopes in Foraminifera, *Geological Society Special Publications*, *183*, 273-291.

Zachos, J. C., L. D. Stott, and K. C. Lohmann (1994), Evolution of early Cenozoic marine temperatures, *Paleoceanography*, *9*(2), 353-387.

Zachos, J., M. Pagani, L. Sloan, E. Thomas, and K. Billups (2001), Trends, Rhythms, and Aberrations in Global Climate 65 Ma to Present, *Science*, *292*(5517), 686-693.

Chapter 6

Summary and Conclusions

6.1 Summary of Results

This chapter summarizes the major results of each chapter and provides an overview of the contributions of this thesis to the science and application of mass-47 clumped isotope paleothermometry. This dissertation revolves around two themes: development and refinement of the mass-47 clumped isotope paleothermometer in the laboratory (Chapters 2 & 3); and the application of the thermometer to new and exciting proxy materials (Chapters 4 & 5), utilizing the developments outlined in the first part of this thesis.

6.1.1 Chapter 2 Summary

This work provides empirical measurements of two critical calibrations that must be used to convert raw Δ_{47} measurements into useful temperature data: 1) The phosphoric acid fractionation factor for Δ_{47}, which places data acquired at higher digestion temperatures in the same reference frame as data produced at 25 °C, and; 2) The Δ_{47}-temperature relationship, which allows conversion of Δ_{47} values into meaningful temperature data. A critical finding of both studies is that mineralogy does not seem to play a role in either the phosphoric acid fractionation factor or the Δ_{47}-temperature calibration, which allows our results to be applied to multiple mineralogical systems. This research also produces the first reported inorganic aragonite Δ_{47}-

temperature calibration, and combines this with previously published work by other authors to produce a composite Δ_{47}-temperature calibration that is statistically robust relative to calibrations produced by earlier studies. Unfortunately, these results do not resolve the discrepancy between published calibrations produced using 25 °C digestions versus those produced at higher temperatures, and we suggest that the discrepancy lies outside of the effects of the phosphoric acid fractionation factor.

6.1.2 Chapter 3 Summary

This work builds on prior studies to fully investigate the effects of end-member mixing of materials of differing bulk composition on measured clumped isotope analyses. Given the large sample size required for clumped isotope analyses, sample homogeneity cannot be assumed. We investigate all possible effects of end-member mixing using numerical modeling, and quantify the scale on which mixing introduces a biasing of clumped isotope temperature estimates. This theoretical model is validated empirically through a comparison of analyses of laboratory mixtures to model output. Finally, guidelines are presented for future studies, recommending the combination of high resolution sub-sampling for conventional $\delta^{18}O$ and $\delta^{13}C$ to define the compositional heterogeneity of materials utilized for clumped isotope analysis.

6.1.3 Chapter 4 Summary

This chapter evaluated the utility of clumped isotope paleothermometry on carbonates that have been altered within the meteoric diagenetic environment and evaluates the potential of meteoric diagenetic phases as a proxy materials for temperature estimates in ancient carbonate sequences. Samples of Pleistocene and Holocene rocks and sediments collected from Bermuda and Barbados were analyzed using a variety of petrographic and isotopic approaches, including the calibrations and model constructed in chapters 2 and 3 of this work. The results

indicate that clumped isotope analysis of meteoric phreatic cements provides an accurate reconstruction of mean annual surface temperature, suggesting that this diagenetic phase may be an ideal proxy material for paleoclimate studies spanning deep geologic time, as they are comparatively resilient to further diagenetic alteration. In contrast, clumped isotope temperature estimates derived from meteoric vadose cements and alteration products yield unreasonably high temperatures. Given the abbreviated diagenetic history of these carbonates, featuring minimal burial or exposure to higher geothermal temperatures, this higher temperature offset cannot possibly reflect either a resetting of the original Δ_{47} temperature record or subsequent equilibrium with other diagenetic fluids. Results presented here suggest disequilibrium fractionation occurs in the meteoric vadose diagentic environment in response to a combination of CO_2 degassing and evaporation that control the carbonate precipitation. Significantly, such findings cast doubt on the utility of other proxy materials precipitated by similar processes, such as speleothems and pedogenic carbonates.

6.1.4 Chapter 5 Summary

This chapter applies the mass-47 clumped isotope paleothermometer to Eocene through Miocene bivalves from the Canterbury Basin of the South Island of New Zealand'. Here, the Δ_{47} paleothermometer is combined with high resolution traditional $\delta^{18}O$ and $\delta^{13}C$ analyses of growth bands within the bivalves to reconstruct detailed climate histories. The results indicate that New Zealand climate progressively warmed from the Eocene to the mid-Miocene. Significantly, these results contrast with an interpretation of cooling that would be assumed from traditional $\delta^{18}O$ analysis studies that do not incorporate clumped isotope analysis as a means of independently constraining temperature. This study highlights the power of the clumped isotope approach and

lays the foundation for future studies by using a combination of isotopic techniques to challenge long-held beliefs about the evolution of Cenozoic climate.

6.2 Conclusions and Future Directions

The mass-47 clumped isotope paleothermometer is one of the most exciting developments in field of paleoclimate reconstruction, presenting an unparalleled ability to simultaneously reconstruct temperature and the $\delta^{18}O$ of the precipitating fluid in a single measurement. This dissertation contributes to the development and further application of this thermometer in several ways. Chapters 2 and 3 provide the calibrations and tools necessary to produce informed temperature data from raw Δ_{47} measurements, represening considerable improvements over prior works. These tools are later applied in the case studies presented in chapters 4 and 5 to illustrate the utility of the Δ_{47} carbonate thermometer in paleoclimate reconstructions of Earth history.

Several questions and opportunities for future research arise from this dissertation, listed in order of when they are brought up by the text:

1) What is the cause and origin of discrepant Δ_{47}-temperature calibrations produced by phosphoric acid digestion at 25 °C versus higher reaction temperatures? This issue must be resolved for the broader community to fully embrace the power of Δ_{47} analysis.

2) What are the implications of end-member mixing as well as apparent vadose zone disequilibrium on proxy materials such as speleothems and pedogenic carbonates? Both of these materials are commonly used for a variety of paleoclimate proxy reconstructions based on isotopic techniques, but this dissertation raises questions about whether they accurately record equilibrium conditions. This issue is particularly acute for pedogenic carbonates, where there has been very little work on understanding the equilibrium-disequilibrium state of their

precipitation. Nevertheless, numerous studies have presented paleotemperature reconstructions, some with far reaching implications, despite this lack of fundamental understanding.

3) What is the temperature history of New Zealand and the southern ocean during the Cenozoic? The results of Chapter 5 are surprising yet exciting, though unfortunately very coarse in temporal resolution. Despite this issue, this study challenges the long held belief that New Zealand and the southern ocean progressively cooled (with a few brief warming intervals) across the Eocene to the recent, resulting in today's glaciated climate. Further work in New Zealand at higher temporal resolution will enhance our understanding of the paleoclimate evolution of the southern ocean and of climate evolution during the Cenozoic.

Future work with the mass-47 clumped isotope paleothermometer will no doubt lead to groundbreaking research in the fields of paleoclimate and diagenesis.

Appendices

Appendix 1: Stable isotope results for phosphoric acid digestion of carbonates. All Δ_{47} values are in the Universal Reference Frame (Dennis et al. 2011). Each entry is a single analysis of ~5 mg.

Date Analyzed	Sample	Reaction T (°C)	Cleanup	$\delta^{13}C$	$\delta^{18}O$	Δ_{47}
1/12/2010	Adamussium	25	GC	2.12	4.50	0.7650
10/7/2010	Adamussium	25	GC	2.06	4.37	0.7618
1/12/2011	Adamussium	25	GC	2.12	4.50	0.7627
7/11/2011	Adamussium	50	PP	1.96	4.04	0.7105
7/11/2011	Adamussium	50	PP	1.96	4.04	0.7105
7/12/2011	Adamussium	50	PP	2.00	4.21	0.7219
3/12/2010	Adamussium	60	GC	2.16	3.99	0.7159
3/28/2010	Adamussium	75	GC	1.72	4.15	0.6851
3/28/2010	Adamussium	75	GC	1.96	4.12	0.6811
1/14/2011	Adamussium	75	GC	1.93	4.06	0.6789
7/11/2011	Adamussium	75	PP	2.13	4.33	0.6806
7/12/2011	Adamussium	75	PP	2.13	4.33	0.6788
7/15/2011	Adamussium	75	PP	1.90	4.35	0.7141
10/12/2011	Adamussium	75	PP	1.96	3.92	0.7357
1/14/2011	Adamussium	90	GC	2.01	4.01	0.6365
1/14/2011	Adamussium	90	GC	1.97	4.29	0.7026
1/15/2011	Adamussium	90	GC	1.86	3.91	0.6545
1/15/2011	Adamussium	90	GC	1.90	4.07	0.6911
7/11/2011	Adamussium	90	PP	1.93	3.99	0.6702
7/12/2011	Adamussium	90	PP	1.92	4.01	0.6473
10/11/2011	Adamussium	90	PP	2.06	4.21	0.6909
10/13/2011	Adamussium	90	PP	1.97	3.92	0.7080
3/28/2010	Carrara	25	GC	2.24	-1.65	0.3985
3/28/2010	Carrara	25	GC	1.71	-2.09	0.4141

9/22/2010	Carrara	25	GC	2.13	-1.67	0.3961
9/29/2011	Carrara	25	PP	1.99	-1.86	0.3865
3/15/2010	Carrara	50	GC	2.04	-1.70	0.3669
4/1/2010	Carrara	50	GC	2.13	-1.57	0.3476
10/11/2010	Carrara	50	GC	2.19	-1.75	0.3662
7/11/2011	Carrara	50	PP	2.07	-1.91	0.3612
10/4/2011	Carrara	50	PP	2.17	-1.58	0.3555
3/28/2010	Carrara	75	GC	2.27	-1.55	0.2923
3/28/2010	Carrara	75	GC	2.24	-1.61	0.3306
9/15/2010	Carrara	75	GC	2.05	-1.98	0.3369
1/14/2011	Carrara	75	GC	2.17	-1.65	0.3540
1/14/2011	Carrara	75	GC	2.10	-1.80	0.3155
4/2/2011	Carrara	75	GC	1.97	-1.75	0.3285
7/6/2011	Carrara	75	PP	1.97	-2.21	0.3179
7/10/2011	Carrara	75	PP	1.99	-2.35	0.3125
7/10/2011	Carrara	75	PP	1.96	-2.36	0.3202
9/29/2011	Carrara	75	PP	1.99	-2.17	0.3582
9/30/2011	Carrara	75	PP	1.97	-2.16	0.3483
10/2/2011	Carrara	75	PP	1.99	-2.11	0.3400
1/12/2011	Carrara	90	GC	2.13	-1.62	0.3234
1/12/2011	Carrara	90	GC	2.08	-1.72	0.3318
7/15/2011	Carrara	90	PP	2.13	-1.62	0.2993
10/11/2011	Carrara	90	PP	2.15	-1.63	0.3450
9/15/2010	Jolters Cay	25	GC	4.33	-0.46	0.7037
10/8/2010	Jolters Cay	25	GC	4.86	0.04	0.6945
1/15/2011	Jolters Cay	25	GC	4.89	0.18	0.6466
9/26/2011	Jolters Cay	25	PP	4.70	-0.71	0.6916
9/29/2011	Jolters Cay	25	PP	4.83	-0.05	0.7173
4/4/2010	Jolters Cay	50	GC	4.41	0.24	0.6315
7/19/2011	Jolters Cay	50	PP	4.84	-0.08	0.6583

9/28/2011	Jolters Cay	50	PP	4.81	0.22	0.6695
9/29/2011	Jolters Cay	50	PP	4.79	0.26	0.6770
10/5/2011	Jolters Cay	50	PP	4.95	0.35	0.6424
3/28/2010	Jolters Cay	75	GC	4.87	0.07	0.6287
7/18/2011	Jolters Cay	75	PP	4.93	0.31	0.6454
9/26/2011	Jolters Cay	75	PP	4.85	-0.20	0.6402
9/26/2011	Jolters Cay	75	PP	4.81	-0.25	0.6125
10/2/2011	Jolters Cay	75	PP	5.01	0.40	0.6140
1/12/2011	Jolters Cay	90	GC	4.91	0.20	0.5808
1/12/2011	Jolters Cay	90	GC	4.44	-0.04	0.5847
7/16/2011	Jolters Cay	90	PP	4.91	0.31	0.6133
10/9/2011	Jolters Cay	90	PP	4.88	-0.08	0.6103
10/13/2011	Jolters Cay	90	PP	5.01	0.40	0.6202
10/5/2011	SRM 88b	25	PP	2.14	-5.88	0.6014
10/7/2011	SRM 88b	25	PP	2.16	-5.85	0.5938
10/7/2011	SRM 88b	25	PP	2.03	-5.93	0.5993
10/7/2011	SRM 88b	25	PP	2.12	-5.63	0.6162
10/6/2011	SRM 88b	50	PP	2.17	-5.66	0.5544
10/7/2011	SRM 88b	50	PP	2.20	-5.68	0.5494
10/7/2011	SRM 88b	50	PP	2.40	-5.46	0.6051
10/5/2011	SRM 88b	75	PP	2.36	-6.34	0.5251
10/8/2011	SRM 88b	75	PP	2.34	-5.75	0.5288
10/12/2011	SRM 88b	75	PP	2.19	-5.88	0.5450
10/13/2011	SRM 88b	75	PP	2.17	-6.05	0.5481
10/6/2011	SRM 88b	90	PP	2.24	-5.89	0.5405
10/9/2011	SRM 88b	90	PP	2.28	-6.03	0.5153
10/10/2011	SRM 88b	90	PP	2.32	-5.83	0.5203
10/10/2011	SRM 88b	90	PP	2.26	-6.04	0.5091
10/10/2011	SRM 88b	90	PP	2.33	-5.89	0.5343

Appendix 2: All reported clumped isotope data from literature sources used for calculating the composite calibrations in Chapter 2. See Chapter 2 text for citation information.

Publication	Material	Mineralogy	Reaction Temperature	Δ_{47}
Ghosh et al. 2006	Synthetic	Calcite	25	0.59803
Ghosh et al. 2006	Synthetic	Calcite	25	0.82603
Ghosh et al. 2006	Synthetic	Calcite	25	0.64903
Ghosh et al. 2006	Synthetic	Calcite	25	0.70103
Ghosh et al. 2006	Synthetic	Calcite	25	0.76403
Ghosh et al. 2006	Synthetic	Calcite	25	0.67003
Ghosh et al. 2006	Synthetic	Calcite	25	0.59803
Ghosh et al. 2007	Biogenic	Aragonite	25	0.77903
Ghosh et al. 2007	Biogenic	Aragonite	25	0.69303
Ghosh et al. 2007	Biogenic	Aragonite	25	0.81703
Ghosh et al. 2007	Biogenic	Aragonite	25	0.69803
Ghosh et al. 2007	Biogenic	Aragonite	25	0.75703
Ghosh et al. 2007	Biogenic	Aragonite	25	0.74603
Ghosh et al. 2007	Biogenic	Aragonite	25	0.70103
Ghosh et al. 2007	Biogenic	Aragonite	25	0.79403
Came et al. 2007	Biogenic	Calcite	25	0.70103
Came et al. 2007	Biogenic	Calcite	25	0.69103
Came et al. 2007	Biogenic	Calcite	25	0.77403
Came et al. 2007	Biogenic	Aragonite	25	0.76403
Came et al. 2007	Biogenic	Aragonite	25	0.79503
Came et al. 2007	Biogenic	Aragonite	25	0.69103
Tripati et al. 2010	Biogenic	Calcite	25	0.70703
Tripati et al. 2010	Biogenic	Calcite	25	0.71003
Tripati et al. 2010	Biogenic	Calcite	25	0.68803
Tripati et al. 2010	Biogenic	Calcite	25	0.68803
Tripati et al. 2010	Biogenic	Calcite	25	0.70503
Tripati et al. 2010	Biogenic	Calcite	25	0.70503
Tripati et al. 2010	Biogenic	Calcite	25	0.67603
Tripati et al. 2010	Biogenic	Calcite	25	0.67903
Tripati et al. 2010	Biogenic	Calcite	25	0.67903
Tripati et al. 2010	Biogenic	Calcite	25	0.67903
Tripati et al. 2010	Biogenic	Calcite	25	0.67903
Tripati et al. 2010	Biogenic	Calcite	25	0.67703
Tripati et al. 2010	Biogenic	Calcite	25	0.67703
Tripati et al. 2010	Biogenic	Calcite	25	0.68803
Tripati et al. 2010	Biogenic	Calcite	25	0.68803
Tripati et al. 2010	Biogenic	Calcite	25	0.68403

Tripati et al. 2010	Biogenic	Calcite	25	0.69403
Tripati et al. 2010	Biogenic	Calcite	25	0.71003
Tripati et al. 2010	Biogenic	Calcite	25	0.72003
Tripati et al. 2010	Biogenic	Calcite	25	0.72003
Tripati et al. 2010	Biogenic	Calcite	25	0.69503
Tripati et al. 2010	Biogenic	Calcite	25	0.69503
Tripati et al. 2010	Biogenic	Calcite	25	0.70803
Tripati et al. 2010	Biogenic	Calcite	25	0.75003
Tripati et al. 2010	Biogenic	Calcite	25	0.77703
Tripati et al. 2010	Biogenic	Calcite	25	0.71003
Tripati et al. 2010	Biogenic	Calcite	25	0.74403
Tripati et al. 2010	Biogenic	Calcite	25	0.75603
Tripati et al. 2010	Biogenic	Calcite	25	0.75603
Tripati et al. 2010	Biogenic	Calcite	25	0.69203
Tripati et al. 2010	Biogenic	Calcite	25	0.71103
Tripati et al. 2010	Biogenic	Calcite	25	0.71303
Tripati et al. 2010	Biogenic	Calcite	25	0.72103
Tripati et al. 2010	Biogenic	Calcite	25	0.71603
Tripati et al. 2010	Biogenic	Calcite	25	0.75603
Tripati et al. 2010	Biogenic	Calcite	25	0.73803
Tripati et al. 2010	Biogenic	Calcite	25	0.73803
Tripati et al. 2010	Biogenic	Calcite	25	0.73603
Tripati et al. 2010	Biogenic	Calcite	25	0.73603
Tripati et al. 2010	Biogenic	Calcite	25	0.73603
Tripati et al. 2010	Biogenic	Calcite	25	0.73603
Tripati et al. 2010	Biogenic	Calcite	25	0.71203
Tripati et al. 2010	Biogenic	Calcite	25	0.81003
Tripati et al. 2010	Biogenic	Calcite	25	0.81003
Tripati et al. 2010	Biogenic	Calcite	25	0.80703
Tripati et al. 2010	Biogenic	Calcite	25	0.80703
Tripati et al. 2010	Biogenic	Calcite	25	0.81003
Tripati et al. 2010	Biogenic	Calcite	25	0.79503
Tripati et al. 2010	Biogenic	Calcite	25	0.78603
Tripati et al. 2010	Biogenic	Calcite	25	0.80603
Tripati et al. 2010	Biogenic	Calcite	25	0.81303
Tripati et al. 2010	Biogenic	Calcite	25	0.73703
Tripati et al. 2010	Biogenic	Calcite	25	0.76703
Tripati et al. 2010	Biogenic	Calcite	25	0.77703
Tripati et al. 2010	Biogenic	Calcite	25	0.75203
Tripati et al. 2010	Biogenic	Calcite	25	0.80103
Tripati et al. 2010	Biogenic	Calcite	25	0.68403
Tripati et al. 2010	Biogenic	Calcite	25	0.68403
Tripati et al. 2010	Biogenic	Calcite	25	0.68403

Tripati et al. 2010	Biogenic	Calcite	25	0.68403
Tripati et al. 2010	Biogenic	Calcite	25	0.68403
Tripati et al. 2010	Biogenic	Calcite	25	0.79403
Tripati et al. 2010	Biogenic	Calcite	25	0.78903
Tripati et al. 2010	Biogenic	Calcite	25	0.78303
Zaarur et al. 2013	Synthetic	Calcite	25	0.80103
Zaarur et al. 2013	Synthetic	Calcite	25	0.80603
Zaarur et al. 2013	Synthetic	Calcite	25	0.81103
Zaarur et al. 2013	Synthetic	Mixture	25	0.80003
Zaarur et al. 2013	Synthetic	Mixture	25	0.77103
Zaarur et al. 2013	Synthetic	Mixture	25	0.73903
Zaarur et al. 2013	Synthetic	Calcite	25	0.71003
Zaarur et al. 2013	Synthetic	Calcite	25	0.72103
Zaarur et al. 2013	Synthetic	Calcite	25	0.78303
Zaarur et al. 2013	Synthetic	Calcite	25	0.70003
Zaarur et al. 2013	Synthetic	Calcite	25	0.71303
Zaarur et al. 2013	Synthetic	Calcite	25	0.70303
Zaarur et al. 2013	Synthetic	Calcite	25	0.67403
Zaarur et al. 2013	Synthetic	Calcite	25	0.67003
Zaarur et al. 2013	Synthetic	Calcite	25	0.66803
Zaarur et al. 2013	Synthetic	Mixture	25	0.61903
Zaarur et al. 2013	Synthetic	Mixture	25	0.60203
Zaarur et al. 2013	Synthetic	Mixture	25	0.61503
Zaarur et al. 2013	Synthetic	Mixture	25	0.58303
Zaarur et al. 2013	Synthetic	Mixture	25	0.55903
Zaarur et al. 2013	Synthetic	Mixture	25	0.55303
Eagle et al. 2010	Biogenic	Bioapitite	90	0.656339
Eagle et al. 2010	Biogenic	Bioapitite	90	0.656339
Eagle et al. 2010	Biogenic	Bioapitite	90	0.656339
Eagle et al. 2010	Biogenic	Bioapitite	90	0.656339
Eagle et al. 2010	Biogenic	Bioapitite	90	0.656339
Eagle et al. 2010	Biogenic	Bioapitite	90	0.656339
Eagle et al. 2010	Biogenic	Bioapitite	90	0.655339
Eagle et al. 2010	Biogenic	Bioapitite	90	0.655339
Eagle et al. 2010	Biogenic	Bioapitite	90	0.655339
Eagle et al. 2010	Biogenic	Bioapitite	90	0.655339
Eagle et al. 2010	Biogenic	Bioapitite	90	0.700342
Eagle et al. 2010	Biogenic	Bioapitite	90	0.700342
Eagle et al. 2010	Biogenic	Bioapitite	90	0.700342
Eagle et al. 2010	Biogenic	Bioapitite	90	0.700342
Eagle et al. 2010	Biogenic	Bioapitite	90	0.700342
Eagle et al. 2010	Biogenic	Bioapitite	90	0.700342
Eagle et al. 2010	Biogenic	Bioapitite	90	0.700342

Eagle et al. 2010	Biogenic	Bioapitite	90	0.701342
Eagle et al. 2010	Biogenic	Bioapitite	90	0.701342
Eagle et al. 2010	Biogenic	Bioapitite	90	0.701342
Eagle et al. 2010	Biogenic	Bioapitite	90	0.703343
Eagle et al. 2010	Biogenic	Bioapitite	90	0.703343
Eagle et al. 2010	Biogenic	Bioapitite	90	0.703343
Eagle et al. 2010	Biogenic	Bioapitite	90	0.703343
Eagle et al. 2010	Biogenic	Bioapitite	90	0.703343
Eagle et al. 2010	Biogenic	Bioapitite	90	0.717344
Eagle et al. 2010	Biogenic	Bioapitite	90	0.717344
Eagle et al. 2010	Biogenic	Bioapitite	90	0.717344
Dennis and Schrag 2010	Synthetic	Unknown	90	0.720344
Dennis and Schrag 2010	Synthetic	Unknown	90	0.720344
Dennis and Schrag 2010	Synthetic	Unknown	90	0.742346
Dennis and Schrag 2010	Synthetic	Unknown	90	0.742346
Dennis and Schrag 2010	Synthetic	Unknown	90	0.742346
Dennis and Schrag 2010	Synthetic	Unknown	90	0.712343
Dennis and Schrag 2010	Synthetic	Unknown	90	0.712343
Dennis and Schrag 2010	Synthetic	Unknown	90	0.682341
Dennis and Schrag 2010	Synthetic	Unknown	90	0.682341
Dennis and Schrag 2010	Synthetic	Unknown	90	0.682341
Dennis and Schrag 2010	Synthetic	Unknown	90	0.691342
Dennis and Schrag 2010	Synthetic	Unknown	90	0.691342
Dennis and Schrag 2010	Synthetic	Unknown	90	0.757347
Dennis and Schrag 2010	Synthetic	Unknown	90	0.757347
Dennis and Schrag 2010	Synthetic	Unknown	90	0.703343
Dennis and Schrag 2010	Synthetic	Unknown	90	0.703343
Dennis and Schrag 2010	Synthetic	Unknown	90	0.66934
Dennis and Schrag 2010	Synthetic	Unknown	90	0.66934
Dennis and Schrag 2010	Synthetic	Unknown	90	0.66934
Dennis and Schrag 2010	Synthetic	Unknown	90	0.67334
Dennis and Schrag 2010	Synthetic	Unknown	90	0.67334
Dennis and Schrag 2010	Synthetic	Unknown	90	0.646338
Dennis and Schrag 2010	Synthetic	Unknown	90	0.646338
Dennis and Schrag 2010	Synthetic	Unknown	90	0.646338
Dennis and Schrag 2010	Synthetic	Unknown	90	0.646338
Dennis and Schrag 2010	Synthetic	Unknown	90	0.607335
Dennis and Schrag 2010	Synthetic	Unknown	90	0.607335
Dennis and Schrag 2010	Synthetic	Unknown	90	0.607335
Dennis and Schrag 2010	Synthetic	Unknown	90	0.607335
Dennis and Schrag 2010	Synthetic	Unknown	90	0.607335
Dennis and Schrag 2010	Synthetic	Unknown	90	0.621336
Dennis and Schrag 2010	Synthetic	Unknown	90	0.621336

Dennis and Schrag 2010	Synthetic	Unknown	90	0.621336
Dennis and Schrag 2010	Synthetic	Unknown	90	0.621336
Dennis and Schrag 2010	Synthetic	Unknown	90	0.587333
Dennis and Schrag 2010	Synthetic	Unknown	90	0.587333
Dennis and Schrag 2010	Synthetic	Unknown	90	0.587333
Dennis and Schrag 2010	Synthetic	Unknown	90	0.587333
Dennis and Schrag 2010	Synthetic	Unknown	90	0.613335
Dennis and Schrag 2010	Synthetic	Unknown	90	0.613335
Dennis and Schrag 2010	Synthetic	Unknown	90	0.613335
Dennis and Schrag 2010	Synthetic	Unknown	90	0.583333
Dennis and Schrag 2010	Synthetic	Unknown	90	0.583333
Dennis and Schrag 2010	Synthetic	Unknown	90	0.583333
Henkes et al. 2013	Biogenic	Aragonite	90	0.770348
Henkes et al. 2013	Biogenic	Aragonite	90	0.770348
Henkes et al. 2013	Biogenic	Aragonite	90	0.770348
Henkes et al. 2013	Biogenic	Aragonite	90	0.785349
Henkes et al. 2013	Biogenic	Aragonite	90	0.785349
Henkes et al. 2013	Biogenic	Aragonite	90	0.785349
Henkes et al. 2013	Biogenic	Aragonite	90	0.778349
Henkes et al. 2013	Biogenic	Aragonite	90	0.778349
Henkes et al. 2013	Biogenic	Aragonite	90	0.778349
Henkes et al. 2013	Biogenic	Aragonite	90	0.774348
Henkes et al. 2013	Biogenic	Aragonite	90	0.774348
Henkes et al. 2013	Biogenic	Aragonite	90	0.774348
Henkes et al. 2013	Biogenic	Aragonite	90	0.759347
Henkes et al. 2013	Biogenic	Aragonite	90	0.759347
Henkes et al. 2013	Biogenic	Aragonite	90	0.759347
Henkes et al. 2013	Biogenic	Aragonite	90	0.759347
Henkes et al. 2013	Biogenic	Aragonite	90	0.777349
Henkes et al. 2013	Biogenic	Aragonite	90	0.777349
Henkes et al. 2013	Biogenic	Aragonite	90	0.777349
Henkes et al. 2013	Biogenic	Calcite	90	0.784349
Henkes et al. 2013	Biogenic	Calcite	90	0.784349
Henkes et al. 2013	Biogenic	Calcite	90	0.784349
Henkes et al. 2013	Biogenic	Calcite	90	0.765348
Henkes et al. 2013	Biogenic	Calcite	90	0.765348
Henkes et al. 2013	Biogenic	Calcite	90	0.765348
Henkes et al. 2013	Biogenic	Calcite	90	0.786349
Henkes et al. 2013	Biogenic	Calcite	90	0.786349
Henkes et al. 2013	Biogenic	Calcite	90	0.786349
Henkes et al. 2013	Biogenic	Calcite	90	0.786349
Henkes et al. 2013	Biogenic	Calcite	90	0.786349
Henkes et al. 2013	Biogenic	Aragonite	90	0.783349

Henkes et al. 2013	Biogenic	Aragonite	90	0.783349
Henkes et al. 2013	Biogenic	Aragonite	90	0.783349
Henkes et al. 2013	Biogenic	Aragonite	90	0.766348
Henkes et al. 2013	Biogenic	Aragonite	90	0.766348
Henkes et al. 2013	Biogenic	Aragonite	90	0.766348
Henkes et al. 2013	Biogenic	Aragonite	90	0.775349
Henkes et al. 2013	Biogenic	Aragonite	90	0.775349
Henkes et al. 2013	Biogenic	Aragonite	90	0.775349
Henkes et al. 2013	Biogenic	Aragonite	90	0.760347
Henkes et al. 2013	Biogenic	Aragonite	90	0.760347
Henkes et al. 2013	Biogenic	Aragonite	90	0.760347
Henkes et al. 2013	Biogenic	Aragonite	90	0.755347
Henkes et al. 2013	Biogenic	Aragonite	90	0.755347
Henkes et al. 2013	Biogenic	Aragonite	90	0.755347
Henkes et al. 2013	Biogenic	Aragonite	90	0.747346
Henkes et al. 2013	Biogenic	Aragonite	90	0.79035
Henkes et al. 2013	Biogenic	Aragonite	90	0.79035
Henkes et al. 2013	Biogenic	Aragonite	90	0.79035
Henkes et al. 2013	Biogenic	Aragonite	90	0.761347
Henkes et al. 2013	Biogenic	Aragonite	90	0.761347
Henkes et al. 2013	Biogenic	Aragonite	90	0.761347
Henkes et al. 2013	Biogenic	Aragonite	90	0.758347
Henkes et al. 2013	Biogenic	Aragonite	90	0.758347
Henkes et al. 2013	Biogenic	Aragonite	90	0.758347
Henkes et al. 2013	Biogenic	Aragonite	90	0.760347
Henkes et al. 2013	Biogenic	Aragonite	90	0.760347
Henkes et al. 2013	Biogenic	Aragonite	90	0.760347
Henkes et al. 2013	Biogenic	Aragonite	90	0.767348
Henkes et al. 2013	Biogenic	Aragonite	90	0.767348
Henkes et al. 2013	Biogenic	Aragonite	90	0.767348
Henkes et al. 2013	Biogenic	Aragonite	90	0.731345
Henkes et al. 2013	Biogenic	Aragonite	90	0.731345
Henkes et al. 2013	Biogenic	Aragonite	90	0.731345
Henkes et al. 2013	Biogenic	Aragonite	90	0.658339
Henkes et al. 2013	Biogenic	Aragonite	90	0.658339
Henkes et al. 2013	Biogenic	Aragonite	90	0.658339
Henkes et al. 2013	Biogenic	Aragonite	90	0.694342
Henkes et al. 2013	Biogenic	Aragonite	90	0.694342
Henkes et al. 2013	Biogenic	Aragonite	90	0.694342
Henkes et al. 2013	Biogenic	Aragonite	90	0.699342
Henkes et al. 2013	Biogenic	Aragonite	90	0.699342
Henkes et al. 2013	Biogenic	Aragonite	90	0.699342
Henkes et al. 2013	Biogenic	Aragonite	90	0.692342

Henkes et al. 2013	Biogenic	Aragonite	90	0.692342
Henkes et al. 2013	Biogenic	Aragonite	90	0.692342
Henkes et al. 2013	Biogenic	Aragonite	90	0.701342
Henkes et al. 2013	Biogenic	Aragonite	90	0.701342
Henkes et al. 2013	Biogenic	Aragonite	90	0.701342
Henkes et al. 2013	Biogenic	Aragonite	90	0.695342
Henkes et al. 2013	Biogenic	Aragonite	90	0.695342
Henkes et al. 2013	Biogenic	Aragonite	90	0.695342
Henkes et al. 2013	Biogenic	Aragonite	90	0.742346
Henkes et al. 2013	Biogenic	Aragonite	90	0.742346
Henkes et al. 2013	Biogenic	Aragonite	90	0.720344
Henkes et al. 2013	Biogenic	Aragonite	90	0.720344
Henkes et al. 2013	Biogenic	Aragonite	90	0.720344
Henkes et al. 2013	Biogenic	Aragonite	90	0.717344
Henkes et al. 2013	Biogenic	Aragonite	90	0.717344
Henkes et al. 2013	Biogenic	Aragonite	90	0.717344
Henkes et al. 2013	Biogenic	Calcite	90	0.778349
Henkes et al. 2013	Biogenic	Calcite	90	0.778349
Henkes et al. 2013	Biogenic	Calcite	90	0.778349
Henkes et al. 2013	Biogenic	Calcite	90	0.778349
Henkes et al. 2013	Biogenic	Calcite	90	0.778349
Henkes et al. 2013	Biogenic	Calcite	90	0.759347
Henkes et al. 2013	Biogenic	Calcite	90	0.759347
Henkes et al. 2013	Biogenic	Calcite	90	0.759347
Henkes et al. 2013	Biogenic	Calcite	90	0.759347
Henkes et al. 2013	Biogenic	Calcite	90	0.771348
Henkes et al. 2013	Biogenic	Calcite	90	0.771348
Henkes et al. 2013	Biogenic	Calcite	90	0.743346
Henkes et al. 2013	Biogenic	Calcite	90	0.743346
Henkes et al. 2013	Biogenic	Calcite	90	0.743346
Henkes et al. 2013	Biogenic	Calcite	90	0.743346
Henkes et al. 2013	Biogenic	Calcite	90	0.737345
Henkes et al. 2013	Biogenic	Calcite	90	0.737345
Henkes et al. 2013	Biogenic	Calcite	90	0.737345
Henkes et al. 2013	Biogenic	Calcite	90	0.688341
Henkes et al. 2013	Biogenic	Calcite	90	0.688341
Henkes et al. 2013	Biogenic	Calcite	90	0.710343
Henkes et al. 2013	Biogenic	Calcite	90	0.710343
Henkes et al. 2013	Biogenic	Calcite	90	0.710343
Henkes et al. 2013	Biogenic	Aragonite	90	0.728345
Henkes et al. 2013	Biogenic	Aragonite	90	0.728345
Henkes et al. 2013	Biogenic	Aragonite	90	0.728345
Henkes et al. 2013	Biogenic	Aragonite	90	0.719344

Henkes et al. 2013	Biogenic	Aragonite	90	0.719344
Henkes et al. 2013	Biogenic	Aragonite	90	0.719344
Henkes et al. 2013	Biogenic	Aragonite	90	0.728345
Henkes et al. 2013	Biogenic	Aragonite	90	0.728345
Henkes et al. 2013	Biogenic	Aragonite	90	0.728345
Henkes et al. 2013	Biogenic	Aragonite	90	0.698342
Henkes et al. 2013	Biogenic	Aragonite	90	0.698342
Henkes et al. 2013	Biogenic	Aragonite	90	0.698342
Henkes et al. 2013	Biogenic	Aragonite	90	0.708343
Henkes et al. 2013	Biogenic	Aragonite	90	0.708343
Henkes et al. 2013	Biogenic	Aragonite	90	0.708343
Henkes et al. 2013	Biogenic	Aragonite	90	0.711343
Henkes et al. 2013	Biogenic	Aragonite	90	0.711343
Henkes et al. 2013	Biogenic	Aragonite	90	0.711343
Henkes et al. 2013	Biogenic	Calcite	90	0.78735
Henkes et al. 2013	Biogenic	Calcite	90	0.78735
Henkes et al. 2013	Biogenic	Calcite	90	0.78735
Henkes et al. 2013	Biogenic	Calcite	90	0.775349
Henkes et al. 2013	Biogenic	Calcite	90	0.775349
Henkes et al. 2013	Biogenic	Calcite	90	0.775349
Henkes et al. 2013	Biogenic	Calcite	90	0.758347
Henkes et al. 2013	Biogenic	Calcite	90	0.758347
Henkes et al. 2013	Biogenic	Calcite	90	0.758347
Henkes et al. 2013	Biogenic	Calcite	90	0.759347
Henkes et al. 2013	Biogenic	Calcite	90	0.759347
Henkes et al. 2013	Biogenic	Calcite	90	0.759347
Henkes et al. 2013	Biogenic	Calcite	90	0.756347
Henkes et al. 2013	Biogenic	Calcite	90	0.756347
Henkes et al. 2013	Biogenic	Calcite	90	0.678341
Henkes et al. 2013	Biogenic	Calcite	90	0.678341
Henkes et al. 2013	Biogenic	Calcite	90	0.678341
Eagle et al. 2013	Biogenic	Aragonite	90	0.842354
Eagle et al. 2013	Biogenic	Aragonite	90	0.851355
Eagle et al. 2013	Biogenic	Aragonite	90	0.761347
Eagle et al. 2013	Biogenic	Aragonite	90	0.79435
Eagle et al. 2013	Biogenic	Aragonite	90	0.743346
Eagle et al. 2013	Biogenic	Aragonite	90	0.743346
Eagle et al. 2013	Biogenic	Aragonite	90	0.731345
Eagle et al. 2013	Biogenic	Aragonite	90	0.731345
Eagle et al. 2013	Biogenic	Aragonite	90	0.731345
Eagle et al. 2013	Biogenic	Mixture	90	0.78835
Eagle et al. 2013	Biogenic	Mixture	90	0.79435
Eagle et al. 2013	Biogenic	Mixture	90	0.836354

Eagle et al. 2013	Biogenic	Calcite	90	0.802351
Eagle et al. 2013	Biogenic	Calcite	90	0.767348
Eagle et al. 2013	Biogenic	Calcite	90	0.775349
Eagle et al. 2013	Biogenic	Calcite	90	0.821352
Eagle et al. 2013	Biogenic	Calcite	90	0.765348
Eagle et al. 2013	Biogenic	Calcite	90	0.764348
Eagle et al. 2013	Biogenic	Calcite	90	0.745346
Eagle et al. 2013	Biogenic	Calcite	90	0.756347
Eagle et al. 2013	Biogenic	Calcite	90	0.720344
Eagle et al. 2013	Biogenic	Calcite	90	0.714344
Eagle et al. 2013	Biogenic	Calcite	90	0.79635
Eagle et al. 2013	Biogenic	Calcite	90	0.759347
Eagle et al. 2013	Biogenic	Calcite	90	0.742346
Eagle et al. 2013	Biogenic	Calcite	90	0.737345
Eagle et al. 2013	Biogenic	Calcite	90	0.737345
Eagle et al. 2013	Biogenic	Calcite	90	0.743346
Eagle et al. 2013	Biogenic	Calcite	90	0.753347
Eagle et al. 2013	Biogenic	Calcite	90	0.687341
Eagle et al. 2013	Biogenic	Mixture	90	0.763348
Eagle et al. 2013	Biogenic	Mixture	90	0.742346
Eagle et al. 2013	Biogenic	Calcite	90	0.784349
Eagle et al. 2013	Biogenic	Calcite	90	0.777349
Eagle et al. 2013	Biogenic	Calcite	90	0.753347
Eagle et al. 2013	Biogenic	Calcite	90	0.725344
Eagle et al. 2013	Biogenic	Calcite	90	0.739346
Eagle et al. 2013	Biogenic	Calcite	90	0.739346
Eagle et al. 2013	Biogenic	Calcite	90	0.749346
Eagle et al. 2013	Biogenic	Calcite	90	0.735345
Eagle et al. 2013	Biogenic	Calcite	90	0.728345
Eagle et al. 2013	Biogenic	Calcite	90	0.748346
Eagle et al. 2013	Biogenic	Calcite	90	0.751347
Eagle et al. 2013	Biogenic	Calcite	90	0.762347
Eagle et al. 2013	Biogenic	Calcite	90	0.730345
Eagle et al. 2013	Biogenic	Calcite	90	0.730345
Eagle et al. 2013	Biogenic	Calcite	90	0.730345
Eagle et al. 2013	Biogenic	Calcite	90	0.730345
Eagle et al. 2013	Biogenic	Calcite	90	0.747346
Eagle et al. 2013	Biogenic	Calcite	90	0.747346
Eagle et al. 2013	Biogenic	Calcite	90	0.747346
Eagle et al. 2013	Biogenic	Calcite	90	0.747346
Eagle et al. 2013	Biogenic	Mixture	90	0.741346
Eagle et al. 2013	Biogenic	Mixture	90	0.741346
Eagle et al. 2013	Biogenic	Mixture	90	0.741346

Eagle et al. 2013	Biogenic	Mixture	90	0.741346
Eagle et al. 2013	Biogenic	Mixture	90	0.741346
Eagle et al. 2013	Biogenic	Mixture	90	0.741346
Eagle et al. 2013	Biogenic	Mixture	90	0.729345
Eagle et al. 2013	Biogenic	Mixture	90	0.729345
Eagle et al. 2013	Biogenic	Mixture	90	0.729345
Eagle et al. 2013	Biogenic	Mixture	90	0.729345
Eagle et al. 2013	Biogenic	Mixture	90	0.716344
Eagle et al. 2013	Biogenic	Mixture	90	0.716344
Eagle et al. 2013	Biogenic	Mixture	90	0.716344
Eagle et al. 2013	Biogenic	Mixture	90	0.718344
Eagle et al. 2013	Biogenic	Mixture	90	0.718344
Eagle et al. 2013	Biogenic	Mixture	90	0.718344
Eagle et al. 2013	Biogenic	Mixture	90	0.718344
Eagle et al. 2013	Biogenic	Calcite	90	0.717344
Eagle et al. 2013	Biogenic	Calcite	90	0.717344
Eagle et al. 2013	Biogenic	Calcite	90	0.717344
Eagle et al. 2013	Biogenic	Calcite	90	0.717344
Eagle et al. 2013	Biogenic	Calcite	90	0.717344
Eagle et al. 2013	Biogenic	Calcite	90	0.717344
Eagle et al. 2013	Biogenic	Aragonite	90	0.79335
Eagle et al. 2013	Biogenic	Aragonite	90	0.79335
Eagle et al. 2013	Biogenic	Aragonite	90	0.79335
Eagle et al. 2013	Biogenic	Aragonite	90	0.79335
Eagle et al. 2013	Biogenic	Aragonite	90	0.79135
Eagle et al. 2013	Biogenic	Aragonite	90	0.79135
Eagle et al. 2013	Biogenic	Aragonite	90	0.79135
Eagle et al. 2013	Biogenic	Aragonite	90	0.810351
Eagle et al. 2013	Biogenic	Aragonite	90	0.810351
Eagle et al. 2013	Biogenic	Aragonite	90	0.810351
Eagle et al. 2013	Biogenic	Aragonite	90	0.810351
Eagle et al. 2013	Biogenic	Calcite	90	0.79835
Eagle et al. 2013	Biogenic	Calcite	90	0.79835
Eagle et al. 2013	Biogenic	Calcite	90	0.79835
Eagle et al. 2013	Biogenic	Calcite	90	0.79835
Eagle et al. 2013	Biogenic	Calcite	90	0.801351
Eagle et al. 2013	Biogenic	Calcite	90	0.801351
Eagle et al. 2013	Biogenic	Mixture	90	0.767348
Eagle et al. 2013	Biogenic	Mixture	90	0.767348
Eagle et al. 2013	Biogenic	Mixture	90	0.767348
Eagle et al. 2013	Biogenic	Mixture	90	0.767348
Eagle et al. 2013	Biogenic	Mixture	90	0.767348
Eagle et al. 2013	Biogenic	Mixture	90	0.78735

Eagle et al. 2013	Biogenic	Mixture	90	0.78735
Eagle et al. 2013	Biogenic	Mixture	90	0.78735
Eagle et al. 2013	Biogenic	Mixture	90	0.78735
Eagle et al. 2013	Biogenic	Mixture	90	0.780349
Eagle et al. 2013	Biogenic	Mixture	90	0.780349
Eagle et al. 2013	Biogenic	Mixture	90	0.780349
Eagle et al. 2013	Biogenic	Mixture	90	0.776349
Eagle et al. 2013	Biogenic	Mixture	90	0.776349
Eagle et al. 2013	Biogenic	Mixture	90	0.776349
Eagle et al. 2013	Biogenic	Mixture	90	0.776349
Eagle et al. 2013	Biogenic	Aragonite	90	0.756347
Eagle et al. 2013	Biogenic	Aragonite	90	0.756347
Eagle et al. 2013	Biogenic	Aragonite	90	0.756347
Eagle et al. 2013	Biogenic	Aragonite	90	0.743346
Eagle et al. 2013	Biogenic	Aragonite	90	0.743346
Eagle et al. 2013	Biogenic	Aragonite	90	0.743346
Eagle et al. 2013	Biogenic	Aragonite	90	0.743346
Eagle et al. 2013	Biogenic	Aragonite	90	0.743346
Eagle et al. 2013	Biogenic	Aragonite	90	0.743346
Eagle et al. 2013	Biogenic	Aragonite	90	0.743346
Eagle et al. 2013	Biogenic	Calcite	90	0.751347
Eagle et al. 2013	Biogenic	Calcite	90	0.751347
Eagle et al. 2013	Biogenic	Calcite	90	0.751347
Eagle et al. 2013	Biogenic	Calcite	90	0.751347
Eagle et al. 2013	Biogenic	Calcite	90	0.751347
Eagle et al. 2013	Biogenic	Calcite	90	0.751347
Eagle et al. 2013	Biogenic	Mixture	90	0.689341
Eagle et al. 2013	Biogenic	Mixture	90	0.685341
Eagle et al. 2013	Biogenic	Aragonite	90	0.685341
Eagle et al. 2013	Biogenic	Aragonite	90	0.685341
Eagle et al. 2013	Biogenic	Aragonite	90	0.685341
Eagle et al. 2013	Biogenic	Aragonite	90	0.705343
Eagle et al. 2013	Biogenic	Aragonite	90	0.705343
Eagle et al. 2013	Biogenic	Aragonite	90	0.705343
Eagle et al. 2013	Biogenic	Aragonite	90	0.713343
Eagle et al. 2013	Biogenic	Aragonite	90	0.713343
Eagle et al. 2013	Biogenic	Aragonite	90	0.713343
Eagle et al. 2013	Biogenic	Aragonite	90	0.713343
Eagle et al. 2013	Biogenic	Aragonite	90	0.713343
Tang et al. 2014	Synthetic	Calcite	90	0.763698
Tang et al. 2014	Synthetic	Calcite	90	0.715694
Tang et al. 2014	Synthetic	Calcite	90	0.747696
Tang et al. 2014	Synthetic	Calcite	90	0.741696

Tang et al. 2014	Synthetic	Calcite	90	0.755697
Tang et al. 2014	Synthetic	Calcite	90	0.738696
Tang et al. 2014	Synthetic	Calcite	90	0.736695
Tang et al. 2014	Synthetic	Calcite	90	0.740696
Tang et al. 2014	Synthetic	Calcite	90	0.759697
Tang et al. 2014	Synthetic	Calcite	90	0.732695
Tang et al. 2014	Synthetic	Calcite	90	0.695692
Tang et al. 2014	Synthetic	Calcite	90	0.734695
Tang et al. 2014	Synthetic	Calcite	90	0.757697
Tang et al. 2014	Synthetic	Calcite	90	0.776699
Tang et al. 2014	Synthetic	Calcite	90	0.757697
Tang et al. 2014	Synthetic	Calcite	90	0.757697
Tang et al. 2014	Synthetic	Calcite	90	0.754697
Tang et al. 2014	Synthetic	Calcite	90	0.738696
Tang et al. 2014	Synthetic	Calcite	90	0.748696
Tang et al. 2014	Synthetic	Calcite	90	0.768698
Tang et al. 2014	Synthetic	Calcite	90	0.741696
Tang et al. 2014	Synthetic	Calcite	90	0.777699
Tang et al. 2014	Synthetic	Calcite	90	0.778699
Tang et al. 2014	Synthetic	Calcite	90	0.728695
Tang et al. 2014	Synthetic	Calcite	90	0.771698
Tang et al. 2014	Synthetic	Calcite	90	0.691692
Tang et al. 2014	Synthetic	Calcite	90	0.703693
Tang et al. 2014	Synthetic	Calcite	90	0.746696
Tang et al. 2014	Synthetic	Calcite	90	0.702693
Tang et al. 2014	Synthetic	Calcite	90	0.727695
Tang et al. 2014	Synthetic	Calcite	90	0.724694
Tang et al. 2014	Synthetic	Calcite	90	0.738696
Tang et al. 2014	Synthetic	Calcite	90	0.727695
Tang et al. 2014	Synthetic	Calcite	90	0.750697
Tang et al. 2014	Synthetic	Calcite	90	0.701692
Tang et al. 2014	Synthetic	Calcite	90	0.66669
Tang et al. 2014	Synthetic	Calcite	90	0.67269
Tang et al. 2014	Synthetic	Calcite	90	0.708693
Tang et al. 2014	Synthetic	Calcite	90	0.693692
Tang et al. 2014	Synthetic	Calcite	90	0.681691
Tang et al. 2014	Synthetic	Calcite	90	0.746696
Tang et al. 2014	Synthetic	Calcite	90	0.652688
Tang et al. 2014	Synthetic	Calcite	90	0.711693
Tang et al. 2014	Synthetic	Calcite	90	0.691692
Tang et al. 2014	Synthetic	Calcite	90	0.691692
Tang et al. 2014	Synthetic	Calcite	90	0.67169
Tang et al. 2014	Synthetic	Calcite	90	0.661689

Tang et al. 2014	Synthetic	Calcite	90	0.702693
Tang et al. 2014	Synthetic	Calcite	90	0.679691
Tang et al. 2014	Synthetic	Calcite	90	0.684691
Tang et al. 2014	Synthetic	Calcite	90	0.642688
Tang et al. 2014	Synthetic	Calcite	90	0.652688
Tang et al. 2014	Synthetic	Calcite	90	0.654689
Tang et al. 2014	Synthetic	Calcite	90	0.638687
Tang et al. 2014	Synthetic	Calcite	90	0.687691
Tang et al. 2014	Synthetic	Calcite	90	0.622686
Tang et al. 2014	Synthetic	Calcite	90	0.653689
Tang et al. 2014	Synthetic	Calcite	90	0.67269
Tang et al. 2014	Synthetic	Calcite	90	0.678691
Tang et al. 2014	Synthetic	Calcite	90	0.634687
Tang et al. 2014	Synthetic	Calcite	90	0.620686
Tang et al. 2014	Synthetic	Calcite	90	0.637687
Tang et al. 2014	Synthetic	Calcite	90	0.578682
Tang et al. 2014	Synthetic	Calcite	90	0.632687
Tang et al. 2014	Synthetic	Calcite	90	0.66969
Tang et al. 2014	Synthetic	Calcite	90	0.633687
Tang et al. 2014	Synthetic	Calcite	90	0.660689
Tang et al. 2014	Synthetic	Calcite	90	0.661689
Defliese	Synthetic	Calcite	75	0.731299
Defliese	Synthetic	Calcite	75	0.742532
Defliese	Synthetic	Calcite	75	0.745072
Defliese	Synthetic	Calcite	75	0.741196
Defliese	Synthetic	Calcite	75	0.716095
Defliese	Synthetic	Calcite	75	0.702321
Defliese	Synthetic	Calcite	75	0.705647
Defliese	Synthetic	Calcite	75	0.657086
Defliese	Synthetic	Calcite	75	0.637267
Defliese	Synthetic	Calcite	75	0.621473
Defliese	Synthetic	Calcite	75	0.597655
Defliese	Synthetic	Calcite	75	0.621772
Defliese	Synthetic	Calcite	75	0.614867
Defliese	Synthetic	Calcite	75	0.632787
Defliese	Synthetic	Calcite	75	0.599419
Defliese	Synthetic	Calcite	75	0.59274
Defliese	Synthetic	Aragonite	75	0.806235
Defliese	Synthetic	Aragonite	75	0.782618
Defliese	Synthetic	Aragonite	75	0.735599
Defliese	Synthetic	Aragonite	75	0.73679
Defliese	Synthetic	Aragonite	75	0.720873
Defliese	Synthetic	Aragonite	75	0.696149

Defliese	Synthetic	Aragonite	75	0.72422
Defliese	Synthetic	Aragonite	75	0.69487
Defliese	Synthetic	Aragonite	75	0.630319
Defliese	Synthetic	Aragonite	75	0.615996
Defliese	Synthetic	Aragonite	75	0.644643
Defliese	Synthetic	Aragonite	75	0.627957
Defliese	Synthetic	Aragonite	75	0.613687
Defliese	Synthetic	Aragonite	75	0.616749
Defliese	Synthetic	Aragonite	75	0.630614
Defliese	Synthetic	Aragonite	75	0.579986
Defliese	Synthetic	Aragonite	75	0.593754
Fernandez et al. 2014	Synthetic	Siderite	100	0.588333
Fernandez et al. 2014	Synthetic	Siderite	100	0.567331
Fernandez et al. 2014	Synthetic	Siderite	100	0.55333
Fernandez et al. 2014	Synthetic	Siderite	100	0.531328
Fernandez et al. 2014	Synthetic	Siderite	100	0.486324
Fernandez et al. 2014	Synthetic	Siderite	100	0.528328
Fernandez et al. 2014	Synthetic	Siderite	100	0.533328
Fernandez et al. 2014	Synthetic	Siderite	100	0.476323
Fernandez et al. 2014	Synthetic	Siderite	100	0.44832
Fernandez et al. 2014	Synthetic	Siderite	100	0.538329
Fernandez et al. 2014	Synthetic	Siderite	100	0.483324
Fernandez et al. 2014	Synthetic	Siderite	100	0.538329
Dennis et al. 2013	Biogenic	Aragonite	90	0.692342
Dennis et al. 2013	Biogenic	Aragonite	90	0.692342
Dennis et al. 2013	Biogenic	Aragonite	90	0.664339
Dennis et al. 2013	Biogenic	Aragonite	90	0.664339
Dennis et al. 2013	Biogenic	Aragonite	90	0.67234
Dennis et al. 2013	Biogenic	Aragonite	90	0.67234
Dennis et al. 2013	Biogenic	Aragonite	90	0.67234
Dennis et al. 2013	Biogenic	Aragonite	90	0.67234
Dennis et al. 2013	Biogenic	Aragonite	90	0.67234
Dennis et al. 2013	Biogenic	Aragonite	90	0.663339
Dennis et al. 2013	Biogenic	Aragonite	90	0.663339
Dennis et al. 2013	Biogenic	Aragonite	90	0.663339
Dennis et al. 2013	Biogenic	Aragonite	90	0.663339
Dennis et al. 2013	Biogenic	Aragonite	90	0.663339
Dennis et al. 2013	Biogenic	Aragonite	90	0.67534
Dennis et al. 2013	Biogenic	Aragonite	90	0.67534
Dennis et al. 2013	Biogenic	Aragonite	90	0.67534
Dennis et al. 2013	Biogenic	Aragonite	90	0.67534
Dennis et al. 2013	Biogenic	Aragonite	90	0.67434
Dennis et al. 2013	Biogenic	Aragonite	90	0.67434

Dennis et al. 2013	Biogenic	Aragonite	90	0.67434
Dennis et al. 2013	Biogenic	Aragonite	90	0.67434
Dennis et al. 2013	Biogenic	Aragonite	90	0.665339
Dennis et al. 2013	Biogenic	Aragonite	90	0.665339
Dennis et al. 2013	Biogenic	Aragonite	90	0.665339
Dennis et al. 2013	Biogenic	Aragonite	90	0.661339
Dennis et al. 2013	Biogenic	Aragonite	90	0.661339
Dennis et al. 2013	Biogenic	Aragonite	90	0.661339
Dennis et al. 2013	Biogenic	Aragonite	90	0.661339
Dennis et al. 2013	Biogenic	Aragonite	90	0.661339
Dennis et al. 2013	Biogenic	Aragonite	90	0.67134
Dennis et al. 2013	Biogenic	Aragonite	90	0.67134
Dennis et al. 2013	Biogenic	Aragonite	90	0.67134
Dennis et al. 2013	Biogenic	Aragonite	90	0.67134
Dennis et al. 2013	Biogenic	Aragonite	90	0.67234
Dennis et al. 2013	Biogenic	Aragonite	90	0.67234
Dennis et al. 2013	Biogenic	Aragonite	90	0.67234
Dennis et al. 2013	Biogenic	Aragonite	90	0.700342
Dennis et al. 2013	Biogenic	Aragonite	90	0.700342
Dennis et al. 2013	Biogenic	Aragonite	90	0.700342
Dennis et al. 2013	Biogenic	Aragonite	90	0.704343
Dennis et al. 2013	Biogenic	Aragonite	90	0.704343
Dennis et al. 2013	Biogenic	Aragonite	90	0.704343
Dennis et al. 2013	Biogenic	Aragonite	90	0.697342
Dennis et al. 2013	Biogenic	Aragonite	90	0.697342
Dennis et al. 2013	Biogenic	Aragonite	90	0.697342
Dennis et al. 2013	Biogenic	Aragonite	90	0.67434
Dennis et al. 2013	Biogenic	Aragonite	90	0.67434
Dennis et al. 2013	Biogenic	Aragonite	90	0.67434
Dennis et al. 2013	Biogenic	Aragonite	90	0.663339
Dennis et al. 2013	Biogenic	Aragonite	90	0.663339
Dennis et al. 2013	Biogenic	Aragonite	90	0.663339
Dennis et al. 2013	Biogenic	Aragonite	90	0.696342
Dennis et al. 2013	Biogenic	Aragonite	90	0.696342
Dennis et al. 2013	Biogenic	Aragonite	90	0.696342
Dennis et al. 2013	Biogenic	Aragonite	90	0.67734
Dennis et al. 2013	Biogenic	Aragonite	90	0.67734
Dennis et al. 2013	Biogenic	Aragonite	90	0.67734
Dennis et al. 2013	Biogenic	Aragonite	90	0.66834
Dennis et al. 2013	Biogenic	Aragonite	90	0.66834
Dennis et al. 2013	Biogenic	Aragonite	90	0.66834
Dennis et al. 2013	Biogenic	Aragonite	90	0.661339
Dennis et al. 2013	Biogenic	Aragonite	90	0.661339

Dennis et al. 2013	Biogenic	Aragonite	90	0.661339
Dennis et al. 2013	Biogenic	Aragonite	90	0.712343
Dennis et al. 2013	Biogenic	Aragonite	90	0.712343
Dennis et al. 2013	Biogenic	Aragonite	90	0.712343
Dennis et al. 2013	Biogenic	Aragonite	90	0.726345
Dennis et al. 2013	Biogenic	Aragonite	90	0.726345
Dennis et al. 2013	Biogenic	Aragonite	90	0.726345
Dennis et al. 2013	Biogenic	Aragonite	90	0.707343
Dennis et al. 2013	Biogenic	Aragonite	90	0.707343
Dennis et al. 2013	Biogenic	Aragonite	90	0.707343
Dennis et al. 2013	Biogenic	Aragonite	90	0.682341
Dennis et al. 2013	Biogenic	Aragonite	90	0.682341
Dennis et al. 2013	Biogenic	Aragonite	90	0.682341
Dennis et al. 2013	Biogenic	Aragonite	90	0.682341
Dennis et al. 2013	Biogenic	Aragonite	90	0.678341
Dennis et al. 2013	Biogenic	Aragonite	90	0.678341
Dennis et al. 2013	Biogenic	Aragonite	90	0.678341
Dennis et al. 2013	Biogenic	Aragonite	90	0.678341
Saenger et al. 2012	Biogenic	Aragonite	25	0.76103
Saenger et al. 2012	Biogenic	Aragonite	25	0.75503
Saenger et al. 2012	Biogenic	Aragonite	25	0.74703
Saenger et al. 2012	Biogenic	Aragonite	25	0.75203
Saenger et al. 2012	Biogenic	Aragonite	25	0.74103
Saenger et al. 2012	Biogenic	Aragonite	25	0.72903
Saenger et al. 2012	Biogenic	Aragonite	25	0.73203
Saenger et al. 2012	Biogenic	Aragonite	25	0.73603
Saenger et al. 2012	Biogenic	Aragonite	25	0.73003
Saenger et al. 2012	Biogenic	Aragonite	25	0.75003
Saenger et al. 2012	Biogenic	Aragonite	25	0.76203
Saenger et al. 2012	Biogenic	Aragonite	25	0.74703
Saenger et al. 2012	Biogenic	Aragonite	25	0.72503
Saenger et al. 2012	Biogenic	Aragonite	25	0.73703
Saenger et al. 2012	Biogenic	Aragonite	25	0.71903
Saenger et al. 2012	Biogenic	Aragonite	25	0.71803
Saenger et al. 2012	Biogenic	Aragonite	25	0.73003
Saenger et al. 2012	Biogenic	Aragonite	25	0.74603
Saenger et al. 2012	Biogenic	Aragonite	25	0.73703
Saenger et al. 2012	Biogenic	Aragonite	25	0.75303
Saenger et al. 2012	Biogenic	Aragonite	25	0.71803
Zaarur et al. 2011	Biogenic	Aragonite	25	0.62903
Zaarur et al. 2011	Biogenic	Aragonite	25	0.62903
Zaarur et al. 2011	Biogenic	Aragonite	25	0.62903
Zaarur et al. 2011	Biogenic	Aragonite	25	0.65603

Zaarur et al. 2011	Biogenic	Aragonite	25	0.65603
Zaarur et al. 2011	Biogenic	Aragonite	25	0.65603
Zaarur et al. 2011	Biogenic	Aragonite	25	0.66303
Zaarur et al. 2011	Biogenic	Aragonite	25	0.66303
Zaarur et al. 2011	Biogenic	Aragonite	25	0.66303
Zaarur et al. 2011	Biogenic	Aragonite	25	0.66303
Zaarur et al. 2011	Biogenic	Aragonite	25	0.63903
Zaarur et al. 2011	Biogenic	Aragonite	25	0.63903
Zaarur et al. 2011	Biogenic	Aragonite	25	0.63903
Zaarur et al. 2011	Biogenic	Aragonite	25	0.64403
Zaarur et al. 2011	Biogenic	Aragonite	25	0.64403
Zaarur et al. 2011	Biogenic	Aragonite	25	0.64403
Zaarur et al. 2011	Biogenic	Aragonite	25	0.64603
Zaarur et al. 2011	Biogenic	Aragonite	25	0.64603
Zaarur et al. 2011	Biogenic	Aragonite	25	0.64603
Zaarur et al. 2011	Biogenic	Aragonite	25	0.64603
Zaarur et al. 2011	Biogenic	Aragonite	25	0.65103
Zaarur et al. 2011	Biogenic	Aragonite	25	0.65103
Zaarur et al. 2011	Biogenic	Aragonite	25	0.65103
Zaarur et al. 2011	Biogenic	Aragonite	25	0.64003
Zaarur et al. 2011	Biogenic	Aragonite	25	0.64003
Zaarur et al. 2011	Biogenic	Aragonite	25	0.64003
Zaarur et al. 2011	Biogenic	Aragonite	25	0.64603
Zaarur et al. 2011	Biogenic	Aragonite	25	0.64603
Zaarur et al. 2011	Biogenic	Aragonite	25	0.64603
Zaarur et al. 2011	Biogenic	Aragonite	25	0.64603
Zaarur et al. 2011	Biogenic	Aragonite	25	0.65303
Zaarur et al. 2011	Biogenic	Aragonite	25	0.65303
Zaarur et al. 2011	Biogenic	Aragonite	25	0.65303
Zaarur et al. 2011	Biogenic	Aragonite	25	0.65303
Zaarur et al. 2011	Biogenic	Aragonite	25	0.65303
Zaarur et al. 2011	Biogenic	Aragonite	25	0.63303
Zaarur et al. 2011	Biogenic	Aragonite	25	0.63303
Zaarur et al. 2011	Biogenic	Aragonite	25	0.63303
Zaarur et al. 2011	Biogenic	Aragonite	25	0.63303
Zaarur et al. 2011	Biogenic	Aragonite	25	0.63303
Zaarur et al. 2011	Biogenic	Aragonite	25	0.63303
Zaarur et al. 2011	Biogenic	Aragonite	25	0.64203
Zaarur et al. 2011	Biogenic	Aragonite	25	0.64203
Zaarur et al. 2011	Biogenic	Aragonite	25	0.64203
Zaarur et al. 2011	Biogenic	Aragonite	25	0.65603
Zaarur et al. 2011	Biogenic	Aragonite	25	0.65603
Zaarur et al. 2011	Biogenic	Aragonite	25	0.65603

Zaarur et al. 2011	Biogenic	Aragonite	25	0.65603
Zaarur et al. 2011	Biogenic	Aragonite	25	0.62303
Zaarur et al. 2011	Biogenic	Aragonite	25	0.62303
Zaarur et al. 2011	Biogenic	Aragonite	25	0.62303
Zaarur et al. 2011	Biogenic	Aragonite	25	0.62303
Zaarur et al. 2011	Biogenic	Aragonite	25	0.62303
Zaarur et al. 2011	Biogenic	Aragonite	25	0.60703
Zaarur et al. 2011	Biogenic	Aragonite	25	0.60703
Zaarur et al. 2011	Biogenic	Aragonite	25	0.60703
Zaarur et al. 2011	Biogenic	Aragonite	25	0.63403
Zaarur et al. 2011	Biogenic	Aragonite	25	0.63403
Zaarur et al. 2011	Biogenic	Aragonite	25	0.63403
Zaarur et al. 2011	Biogenic	Aragonite	25	0.62303
Zaarur et al. 2011	Biogenic	Aragonite	25	0.62303
Zaarur et al. 2011	Biogenic	Aragonite	25	0.62303
Zaarur et al. 2011	Biogenic	Aragonite	25	0.67303
Zaarur et al. 2011	Biogenic	Aragonite	25	0.67303
Zaarur et al. 2011	Biogenic	Aragonite	25	0.67303
Zaarur et al. 2011	Biogenic	Aragonite	25	0.66503
Zaarur et al. 2011	Biogenic	Aragonite	25	0.66503
Zaarur et al. 2011	Biogenic	Aragonite	25	0.66503

Appendix 3: Derivation of Equation 3.16

We start with equation 5 of Dennis et al. (2011):

$$\Delta_{47[SGvsWG]0} = \Delta_{47[SGvsWG]} - \delta^{47} \times EGL_{Slope} \quad \text{(A3.1)}$$

Where $\Delta_{47[SGvsWG]}$ is the raw uncorrected Δ_{47} value. We are attempting to rewrite this equation in order to solve for δ^{47}. To begin, we use eq. 19 to substitute for $\Delta_{47[SGvsWG]}$:

$$\Delta_{47[SGvsWG]0} = \left[\left(\frac{R^{47}}{R^{47*}} - 1\right) - \left(\frac{R^{46}}{R^{46*}} - 1\right) - \left(\frac{R^{45}}{R^{45*}} - 1\right)\right] \times 1000 - \delta^{47} \times EGL_{Slope} \quad \text{(A3.2)}$$

To proceed with the calculation, it is assumed that only δ^{47} contributes to Δ_{47}. This is necessary to solve the equation as otherwise there are too many unknowns, and introduces little error into the calculation as described in the text. In this case, R^{46}/R^{46*} and R^{45}/R^{45*} are assumed to each equal 1. Therefore:

$$\Delta_{47[SGvsWG]0} = \left[\frac{R^{47}}{R^{47*}} - 1\right] \times 1000 - \delta^{47} \times EGL_{Slope} \quad \text{(A3.3)}$$

Eq. 18 is then substituted in for R^{47} in order to describe it in terms of δ^{47}:

$$\Delta_{47[SGvsWG]0} = \left[\frac{\left(\frac{\delta 47}{1000}+1\right)\times R_{WG}^{47*}}{R^{47*}} - 1\right] \times 1000 - \delta^{47} \times EGL_{Slope} \quad \text{(A3.4)}$$

From here it is a matter of rearranging the terms to solve for δ^{47} in terms of the other variables, all of which are known:

$$\Delta_{47[SGvsWG]0} = \delta^{47} \times \left(\frac{R_{WG}^{47*}}{R^{47*}} - EGL_{Slope}\right) + 1000 \times \frac{R_{WG}^{47*}}{R^{47*}} - 1000 \quad \text{(A3.5)}$$

$$\Delta_{47[SGvsWG]0} + 1000 - 1000 \times \frac{R_{WG}^{47*}}{R^{47*}} = \delta^{47} \times \left(\frac{R_{WG}^{47*}}{R^{47*}} - EGL_{Slope}\right) \quad \text{(A3.6)}$$

Both sides are multiplied by R^{47*} for convenience:

$$\left(\Delta_{47[SGvsWG]0} + 1000\right) \times R^{47*} - 1000 \times R_{WG}^{47*} = \delta^{47} \times \left(R_{WG}^{47*} - EGL_{Slope} \times R^{47*}\right) \quad \text{(A3.7)}$$

A final rearrangement yields eq. 3.16:

$$\delta^{47} = \frac{\left(\Delta_{47[SGvsWG]0} + 1000\right) \times R^{47*} - 1000 \times R_{WG}^{47*}}{R_{WG}^{47*} - \mathrm{EGL}_{Slope} \times R^{47*}} \quad \text{(A3.8)}$$

Appendix 4: Eocene High Resolution Data. $\delta^{18}O_{sw}$ values calculated using Δ_{47} temperature estimates and Δ_{47}-derived $\delta^{18}O$, and are relative to VSMOW.

Sample	Subsample	$\delta^{13}C$ (‰) (VPDB)	$\delta^{18}O$ (‰) (VPDB)	T (°C) $\delta^{18}O_{sw}$ = -1.97‰
018A	1.0	1.76	-0.28	12.2
018A	1.1	2.26	-0.27	12.2
018A	1.2	2.51	-0.52	13.3
018A	1.3	2.73	-0.54	13.4
018A	1.4	2.81	-0.59	13.6
018A	1.5	2.96	-0.73	14.2
018A	1.6	3.11	-0.97	15.4
018A	1.7	2.80	-0.54	13.4
018A	2.0	2.73	-0.27	12.1
018A	2.1	2.80	-0.19	11.8
018A	2.2	2.90	-0.09	11.3
018A	2.3	3.08	-0.28	12.2
018A	2.4	3.21	-0.26	12.1
018A	2.5	3.31	-0.32	12.4
018A	2.6	3.46	-0.57	13.5
018A	2.7	3.37	-0.36	12.5
018A	2.8	3.23	-0.56	13.5
018A	3.0	3.02	-0.32	12.4
018A	3.1	3.10	0.12	10.4
018A	3.2	2.94	-0.04	11.1
018A	3.3	3.00	-0.25	12.1
018A	3.4	2.88	-0.13	11.5
018A	3.5	2.99	-0.33	12.4
018A	3.6	2.82	-0.46	13.0
018A	3.7	2.82	-0.32	12.4
018A	3.8	2.65	-0.46	13.0
018A	4.0	2.47	-0.04	11.1
018A	4.1	2.50	-0.12	11.5
018A	4.2	2.77	-0.12	11.5
018A	4.3	2.85	-0.11	11.4
018A	4.4	2.97	-0.17	11.7
018A	4.5	2.87	0.07	10.6
018A	5.0	2.81	-0.01	11.0
018A	5.1	2.75	0.00	10.9
018A	5.2	2.73	-0.10	11.4
018A	5.3	2.64	0.01	10.9
018A	5.4	2.55	-0.16	11.7
018A	5.5	2.70	-0.14	11.5
018A	5.6	2.62	-0.17	11.7
018A	5.7	2.50	0.02	10.9
018A	6.0	2.41	0.08	10.6

018A	6.1	2.46	-0.12	11.5
018A	6.2	2.48	-0.12	11.5
018A	6.3	2.51	-0.34	12.5
018A	6.4	2.59	-0.34	12.4
018A	6.5	2.53	-0.21	11.9
018A	6.6	2.53	0.00	10.9
018A	6.7	2.40	-0.10	11.4
018A	7.0	2.31	-0.04	11.1
018C	1.0	3.36	-0.27	12.1
018C	1.1	3.42	-0.16	11.7
018C	1.2	3.36	-0.23	12.0
018C	1.3	3.33	-0.19	11.8
018C	1.4	3.27	-0.19	11.8
018C	1.5	3.23	-0.22	11.9
018C	1.6	3.17	-0.35	12.5
018C	1.7	3.05	-0.32	12.4
018C	1.8	2.92	-0.37	12.6
018C	1.9	2.87	-0.30	12.3
018C	1.10	3.01	-0.32	12.4
018C	1.11	3.05	-0.28	12.2
018C	1.12	3.15	-0.37	12.6
018C	1.13	3.26	-0.25	12.1
018C	1.14	3.33	-0.14	11.6
018C	1.16	3.28	-0.28	12.2
018C	1.17	3.33	-0.24	12.0
018C	1.18	3.25	-0.33	12.4
018C	1.19	3.25	-0.32	12.4
018C	1.20	3.37	-0.44	12.9
018C	1.21	3.29	-0.38	12.7
018C	1.22	3.33	-0.55	13.4
018C	1.23	3.46	-0.54	13.4
018C	1.24	3.45	-0.74	14.3
018C	2.0	3.35	-0.72	14.2
018C	2.1	3.30	-0.56	13.5
018C	2.2	3.28	-0.35	12.5
018C	2.3	3.29	-0.19	11.8
018C	2.4	3.32	-0.31	12.3
018C	2.5	3.36	-0.14	11.6
018C	2.6	3.42	-0.30	12.3
018C	2.7	3.43	-0.34	12.5
018C	2.8	3.44	-0.26	12.1
018C	2.9	3.44	-0.40	12.7
018C	2.10	3.38	-0.50	13.2
018C	2.11	3.28	-0.61	13.7
018C	2.12	3.27	-0.54	13.4
018C	2.13	3.22	-0.41	12.8
018C	2.14	3.29	-0.43	12.9
018C	2.16	3.18	-0.37	12.6
018C	2.17	3.08	-0.53	13.3

018C	2.18	3.14	-0.37	12.6
018C	2.19	3.12	-0.45	13.0
018C	2.20	3.10	-0.51	13.2
018C	2.21	3.15	-0.39	12.7
018C	2.22	3.19	-0.42	12.8
018C	2.23	3.12	-0.55	13.4
018C	2.24	3.18	-0.35	12.5
018C	2.25	3.20	-0.54	13.4
018C	2.26	3.18	-0.55	13.4
018C	2.27	3.16	-0.60	13.7
018C	2.28	3.17	-0.53	13.3
018C	2.29	3.05	-0.83	14.7
018C	2.30	3.11	-0.79	14.5
018C	3.0	3.06	-0.88	14.9
018C	3.1	3.12	-0.86	14.8
018C	3.2	3.03	-1.16	16.3
018C	3.3	2.99	-1.11	16.0
018C	3.4	3.07	-1.03	15.7
018C	3.5	3.03	-0.43	12.9
018C	3.6	3.00	-0.24	12.0
018C	3.7	3.20	0.03	10.8
018C	3.8	3.11	-0.13	11.5
018C	3.9	3.07	-0.33	12.4
018C	3.10	3.07	-0.24	12.0
018C	3.11	3.05	-0.37	12.6
018C	3.12	3.02	-0.51	13.2
018C	3.13	3.01	-0.52	13.3
018C	3.14	3.00	-0.50	13.2
018C	3.15	2.98	-0.40	12.8
018C	3.16	2.85	-0.52	13.3
018C	3.17	2.89	-0.44	12.9
018C	3.18	3.00	-0.43	12.9
018C	3.19	2.92	-0.71	14.2
018C	4.0	2.92	-0.69	14.1
018C	4.1	2.88	-0.80	14.6
018C	4.2	2.75	-0.54	13.4
018C	4.3	2.79	-0.11	11.4
018C	4.4	2.88	-0.12	11.5
018C	4.5	2.93	-0.19	11.8
018C	4.6	3.00	-0.10	11.4
018C	4.7	3.05	-0.01	11.0
018C	4.8	3.07	-0.07	11.2
018C	4.9	3.12	-0.10	11.4
018C	4.10	3.04	-0.15	11.6
018C	4.11	3.23	-0.10	11.4
018C	4.12	3.14	-0.39	12.7
018C	4.13	3.17	-0.53	13.4
018C	4.14	3.14	-0.35	12.5
018C	4.15	3.09	-0.44	12.9
018C	5.0	3.08	-0.51	13.3

Appendix 5: Oligocene High Resolution Data. $\delta^{18}O_{sw}$ values calculated using Δ_{47} temperature estimates and Δ_{47}-derived $\delta^{18}O$, and are relative to VSMOW.

Sample	Subsample	$\delta^{13}C$ (‰) (VPDB)	$\delta^{18}O$ (‰) (VPDB)	T (°C) $\delta^{18}O_{sw}$ = -0.35‰
011A	1.0	2.31	1.10	13.3
011A	1.1	2.12	1.02	13.6
011A	1.2	2.43	1.07	13.4
011A	1.3	2.50	1.04	13.6
011A	1.4	2.55	0.90	14.2
011A	1.5	2.62	0.82	14.5
011A	1.6	2.81	0.78	14.7
011A	1.7	2.70	0.66	15.3
011A	1.8	2.58	0.60	15.6
011A	1.9	2.47	0.53	15.9
011A	2.0	2.67	0.52	16.0
011A	2.1	2.54	0.67	15.2
011A	2.2	2.51	0.75	14.9
011A	2.3	2.38	0.88	14.3
011A	2.4	2.44	0.89	14.2
011A	2.5	2.30	1.10	13.3
011A	3.0	2.09	0.88	14.3
011A	3.1	2.23	0.91	14.1
011A	3.2	2.26	0.80	14.7
011A	3.3	2.34	0.71	15.1
011A	3.4	2.66	0.86	14.4
011A	3.5	2.59	0.53	15.9
011A	3.6	2.70	0.50	16.1
011A	4.0	2.63	0.54	15.8
011A	4.1	2.12	0.68	15.2
011A	4.2	1.87	0.70	15.1
011A	4.3	2.22	0.60	15.6
011A	4.4	2.09	0.44	16.3
011A	4.5	2.04	0.34	16.8
011A	4.6	2.28	0.23	17.3
011A	4.7	2.28	0.22	17.4
011A	5.0	2.34	0.33	16.9
011A	5.1	2.19	0.60	15.6
011A	5.2	1.94	0.79	14.7
011A	5.3	2.02	0.60	15.6
011A	5.4	2.10	0.53	15.9
011A	5.5	2.27	0.45	16.3
011A	5.6	2.46	0.44	16.4
011A	5.7	2.77	0.70	15.1
011A	5.8	2.64	0.25	17.3
011B	1.0	2.89	0.60	13.4

011B	1.1	2.55	0.96	13.3
011B	1.2	2.64	0.97	13.9
011B	1.3	2.57	0.85	13.5
011B	1.4	2.67	0.93	13.8
011B	1.5	2.68	0.86	13.7
011B	1.5	2.53	0.88	13.9
011B	1.6	2.67	0.85	13.8
011B	1.7	2.64	0.87	14.0
011B	1.8	2.63	0.82	14.2
011B	1.9	2.65	0.77	14.9
011B	1.10	2.65	0.63	14.3
011B	1.11	2.76	0.76	14.6
011B	1.12	2.72	0.70	14.6
011B	1.13	3.00	0.69	14.7
011B	1.14	2.99	0.67	14.8
011B	1.15	3.13	0.65	14.7
011B	1.16	2.80	0.67	14.9
011B	2.0	2.63	0.64	15.3
011B	2.1	2.66	0.55	15.3
011B	2.2	2.64	0.54	15.5
011B	2.3	2.56	0.50	15.5
011B	2.4	2.59	0.51	16.0
011B	2.5	2.54	0.40	15.9
011B	2.6	2.57	0.42	15.5
011B	2.7	2.56	0.50	15.5
011B	2.8	2.59	0.50	15.5
011B	2.9	2.65	0.52	15.7
011B	2.10	2.54	0.47	15.9
011B	2.11	2.56	0.43	15.7
011B	2.12	2.56	0.46	15.4
011B	2.13	2.67	0.52	15.4
011B	2.14	2.72	0.53	14.4
011B	3.0	2.74	0.74	13.4
011B	3.1	2.69	0.96	13.3
011B	3.2	2.61	0.97	12.4
011B	3.3	2.47	1.17	12.8
011B	3.4	2.45	1.09	12.2
011B	3.5	2.55	1.22	13.1
011B	3.6	2.47	1.02	13.2
011B	3.7	2.52	0.94	13.5
011B	3.8	2.65	0.77	14.3
011B	3.9	2.57	0.77	14.3
011B	3.10	2.39	0.19	17.0
011B	4.0	2.50	0.30	16.5
011B	4.1	2.70	0.24	16.7
011B	6.0	2.68	0.36	16.2
011B	6.1	2.58	0.38	16.1
011B	6.2	2.63	0.26	16.6
011B	6.3	2.67	0.38	16.1
011B	6.4	2.75	0.46	15.7

011B	6.5	2.86	0.78	14.2
011B	6.6	2.83	1.11	12.7
011B	6.7	2.74	0.83	14.0
011B	6.8	2.70	0.93	13.5
011B	6.9	2.81	0.90	13.6
011B	6.10	3.14	0.94	13.5
011B	6.11	2.73	0.68	14.7
011B	7.0	2.55	0.69	14.6
011B	7.1	2.21	0.64	14.9
011B	7.2	2.28	0.53	15.4
011B	7.3	2.47	0.54	15.3
011B	7.4	2.60	0.60	15.1
011B	7.5	2.54	0.64	14.9
011B	7.6	2.73	1.01	13.2
011B	7.7	2.55	0.92	13.6
011B	7.8	2.52	1.11	12.7
011B	7.9	2.55	1.31	11.8
011B	7.10	2.51	1.10	12.8
011B	7.11	2.65	1.09	12.8
011B	8.0	2.95	0.84	13.9

Appendix 6: Miocene High Resolution Data. $\delta^{18}O_{sw}$ values calculated using Δ_{47} temperature estimates and Δ_{47}-derived $\delta^{18}O$, and are relative to VSMOW.

Sample	Subsample	$\delta^{13}C$ (‰) (VPDB)	$\delta^{18}O$ (‰) (VPDB)	T (°C) $\delta^{18}O_{sw}$ = -0.05‰
100A	1.0	1.92	0.73	16.4
100A	1.1	1.88	0.44	17.8
100A	1.2	1.94	0.71	16.5
100A	1.3	2.00	0.77	16.2
100A	1.4	2.00	0.64	16.8
100A	1.5	1.99	0.41	18.0
100A	1.6	2.04	0.59	17.1
100A	1.7	1.99	0.42	17.9
100A	1.8	1.94	0.71	16.5
100A	2.0	1.83	0.57	17.2
100A	2.1	1.82	0.63	16.9
100A	2.2	1.90	0.43	17.8
100A	2.3	1.99	0.62	16.9
100A	2.4	2.03	0.66	16.7
100A	2.5	2.12	0.47	17.7
100A	2.6	2.14	0.66	16.7
100A	2.7	2.17	0.58	17.1
100A	2.8	2.12	0.65	16.8
100A	2.9	2.15	0.66	16.7
100A	3.0	1.89	0.80	16.1
100A	3.1	1.89	0.63	16.9
100A	3.2	1.95	0.70	16.6
100A	3.3	1.96	0.59	17.1
100A	3.4	1.87	0.55	17.2
100A	3.5	1.96	0.42	17.9
100A	3.6	2.13	0.58	17.1
100A	3.7	2.15	0.48	17.6
100A	3.8	2.16	0.62	16.9
100A	4.0	2.12	0.69	16.6
100A	4.1	2.02	0.70	16.5
100A	4.2	2.11	0.57	17.2
100A	4.3	2.03	0.58	17.1
100A	4.4	1.98	0.57	17.2
100A	4.5	1.93	0.54	17.3
100A	4.6	1.92	0.53	17.4
100A	4.7	1.93	0.56	17.2
100A	4.8	1.93	0.58	17.1
100A	5.0	1.85	0.60	17.0
100A	5.1	1.86	0.60	17.0
100A	5.2	1.78	0.54	17.3
100A	5.3	1.85	0.49	17.5

100A	5.4	1.95	0.52	17.4
100A	5.5	2.05	0.45	17.7
100A	5.6	2.05	0.47	17.6
100A	5.7	2.08	0.48	17.6
100A	5.8	1.98	0.53	17.4
100A	6.0	1.95	0.54	17.3
100C	1.0	2.14	0.89	15.7
100C	1.1	1.96	0.62	16.9
100C	1.2	2.03	0.77	16.2
100C	1.3	2.03	0.72	16.4
100C	1.4	2.12	0.62	16.9
100C	1.5	2.19	0.66	16.7
100C	1.6	2.26	0.70	16.5
100C	1.7	2.37	0.63	16.9
100C	1.8	2.31	0.62	16.9
100C	1.9	2.36	0.62	16.9
100C	1.10	2.30	0.63	16.9
100C	1.11	2.38	0.55	17.3
100C	1.12	2.27	0.45	17.7
100C	1.13	2.29	0.41	17.9
100C	1.14	2.16	0.38	18.1
100C	1.15	2.27	0.42	17.9
100C	2.0	2.23	0.55	17.3
100C	2.1	2.28	0.69	16.6
100C	2.2	2.13	0.72	16.5
100C	2.3	2.15	0.69	16.6
100C	2.4	2.29	0.94	15.4
100C	2.5	2.16	0.69	16.6
100C	2.6	2.24	0.74	16.4
100C	2.7	2.20	0.73	16.4
100C	2.8	2.37	0.63	16.9
100C	2.9	2.38	0.70	16.6
100C	2.10	2.24	0.68	16.6
100C	2.11	2.25	0.68	16.6
100C	2.12	2.25	0.68	16.6
100C	2.13	2.25	0.65	16.8
100C	2.14	2.21	0.57	17.1
100C	2.15	2.35	0.61	17.0
100C	2.16	2.29	0.60	17.0
100C	2.17	2.53	0.76	16.2
100C	2.18	2.47	0.44	17.8
100C	2.19	2.44	0.55	17.3
100C	3.0	2.39	0.65	16.8
100C	3.1	2.32	0.66	16.7
100C	3.2	2.13	0.62	16.9
100C	3.3	2.07	0.65	16.8
100C	3.4	2.04	0.64	16.8
100C	3.5	2.12	0.64	16.8
100C	3.6	2.09	0.56	17.2

100C	3.7	2.29	0.57	17.1
100C	3.8	2.40	0.68	16.6
100C	3.9	2.39	0.56	17.2
100C	3.10	2.27	0.59	17.1
100C	3.11	2.34	0.59	17.1
100C	3.12	2.24	0.50	17.5
100C	3.13	2.44	0.56	17.2
100C	3.14	2.37	0.45	17.7
100C	3.15	2.34	0.42	17.9
100C	4.0	2.43	0.56	17.2
100C	4.1	2.22	0.65	16.8
100C	4.2	2.04	0.69	16.6
100C	4.3	2.05	0.74	16.4
100C	4.4	2.08	0.66	16.8
100C	4.5	2.11	0.66	16.7
100C	4.6	2.13	0.63	16.9
100C	4.7	2.13	0.58	17.1
100C	4.8	2.17	0.48	17.6
100C	4.9	2.19	0.52	17.4
100C	4.10	2.16	0.51	17.4
100C	5.0	2.22	0.67	16.7
100C	5.1	2.32	0.76	16.3
100C	5.2	2.45	0.70	16.6
100C	5.3	2.38	0.71	16.5
100C	5.4	2.35	0.76	16.3
100C	5.5	2.42	0.70	16.5
100C	5.6	2.47	0.63	16.9
100C	5.7	2.31	0.59	17.1
100C	5.8	2.32	0.59	17.1
100C	5.9	2.30	0.58	17.1
100C	6.0	2.41	0.67	16.7
100C	6.1	2.34	0.78	16.1
100C	6.2	2.36	0.76	16.3
100C	6.3	2.31	0.70	16.5
100C	6.4	2.33	0.64	16.9
100C	6.5	2.32	0.62	16.9
100C	6.6	2.31	0.61	17.0
100C	6.7	2.34	0.66	16.7
100C	7.0	2.30	0.71	16.5